

Light to Electrons to Bonds: Imaging Water Splitting and Collecting Photoexcited Electrons

Thesis by

Andrew Jay Leenheer

In Partial Fulfillment of the Requirements

for the Degree of

Doctor of Philosophy



California Institute of Technology

Pasadena, California

2013

(Defended December 10, 2012)

© 2013

Andrew Jay Leenheer

All Rights Reserved

To my father, who blazed a trail.

Acknowledgments

“We have not succeeded in answering all our problems. The answers we have found only serve to raise a whole set of new questions. In some ways we feel we are as confused as ever, but we believe we are confused on a higher level and about more important things.” — E.C. Kelley

I would like to thank all those who crossed my path at Caltech who helped me find answers or at least helped confuse me on a higher level than when I arrived. Many thanks go to my advisor, Harry Atwater, for his optimism and enthusiasm for science coupled with a depth and breadth of knowledge shared humbly with his students and peers. I also thank Nate Lewis who keeps focus on questions that need answers. The other members of my committee, Brent Fultz and Bill Johnson, greatly expanded my understanding of and appreciation for the basic physical laws that underlie the science of materials, and I appreciated their intuitive approach.

Many postdocs and fellow graduate students were instrumental in the success of my work. I would like to thank Mike Filler who was very welcoming and great at getting me up to speed in the labs, as well as Domenico Pacifici and Brendan Kayes. Imogen Pryce was great to work with when thinking about nitrides and starting e-beam lithography. Shannon Boettcher got me going doing photoelectrochemistry, and Deirdre O’Carroll taught me how to get around a microscope. In my first couple of years I conquered classes together with the help of Mike Deceglie and Davis Darvish and the cheering of Carrie Hofmann. Greg Kimball was a great fellow electrochemist in a physics group, and Mike Kelzenberg helped greatly in setting up measurements. Thanks to Vivian Ferry who showed me that a chemist could do plasmonics. For simulation software help, much appreciation goes again to Deirdre, as well as Chengxiang

Xiang and Koray Aydin. Emily Warmann helped teach me about polishing and refined the flow cell. Thanks to Ryan Briggs for his constant enthusiasm and expertise with all things lasers and microfabrication, and Stan Burgos also was helpful in the fab. While great on guitar, Jim Fakonas also impressed and helped me with NIR optics, plasma processing, and talk about plasmonics. For anything silicon, Dan Turner-Evans was the first person to ask. I much appreciated Carissa Eisler and Jonathan Grandidier for taking over the thankless job of sputterer guru, and Morgan Putnam and Jeff Bosco attempted their best to keep me safe in the lab. For learning semiconductor photoelectrochemistry, Liz Santori, Emily Warmann, Seokmin Jeon, Leslie O’Leary, and James McKone were patient with this physicist-by-training. I also thank Matt Sheldon, who inspires out-of-the-box thinking about plasmonics. Towards the finish, I appreciated Kelsey Whitesell’s expertise with nanoimprint lithography and Victor Brar’s help with FTIR microscopy.

After joining the Joint Center for Artificial Photosynthesis, I had the opportunity to work with some fine electrochemists, including Josh Spurgeon, Matt Shaner, Charles McCrory, and Ty Matthews. Thanks to Bruce Brunschwig for his dedication to working labs and equipment, and I loved the conversations with Joachim Lewerentz, whose early research I ended up following. I had a great time working closely with Ragip Pala on diffusion length measurements, and his always-willing help and contribution to the close of this thesis cannot be overstated. Prineha Narang deserves respect for her dedication to JCAP, and I was privileged to be able to work with her and toss around ideas about plasmons.

I was fortunate to have friendly and easygoing office mates in my various offices who made coming to work enjoyable—Davis Darvish, Katsu Tanabe, Ben Yin, Shu Hu, Adam Pieterick, Marika Letilly, and Erik Verlage. Though all the contributions are too many to mention, every following person with the Atwater group made a difference in my Caltech career (in loose order of appearance): Melissa Archer, Rob Walters, Jen Dionne, Keisuke Nakayama, Ken Diest, Matt Dicken, Krista Langeland, Gerald Miller, Luke Sweatlock, Rene de Waele, Eyal Feigenbaum, Jeremy Munday, Peter Saeta, Marina Leite, Adele Tamboli, Min Jang, Emily Kosten, Hal Emmer,

Chris Chen, Naomi Coronel, Samantha Wilson, Yulia Tolstova, Ruzan Sokhoyan, Martina Schmid, Raymond Weitekamp, Ana Brown, Sunita Darbe, Christofer Flowers, Sondra Hellstrom, John Lloyd, Amanda Shing, Anna Beck, Siying Peng, and Nick Batara. From the Lewis group, I appreciated help from Jim Maiolo, Matt Bierman, Nick Strandwitz, Rob Coridan, Ron Grimm, Shane Ardo, Joe Beardslee, and Fadl Saadi. From JCAP I appreciated conversations with Jenny Yang, Esther Alarcon Llado, Joel Ager, Slobodan Mitrovic, John Gregoire, Kyle Cummins, Jesus Velazquez, and Sujo Jung.

Much of the sample fabrication was done in the micro/nano labs or KNI cleanroom, and I very much appreciate Alireza Ghaffari, Guy DeRose, Melissa Melendes, Kevin Kan, Bophan Chim, Nils Asplund, and Chris Morales for their assistance and for keeping the equipment running. And of course everything would have quickly ground to a halt without the very competent, smiling, and helpful administrators—April Neidholdt, Lyra Haas, Tiffany Kimoto, Jennifer Blankenship, Paige Johnson, Vikki Appel, and Christy Jenstad—who also provided a good dose of normal life alongside the science at Caltech.

I am thankful for the funding support from Caltech, the Applied Materials Fellowship, the National Science Foundation, the Global Climate and Energy Project, and the Department of Energy Office of Science through JCAP which has afforded me the chance to work on a variety of interesting projects wherever they led.

I would not have made it through (or even to!) Caltech without the love and support of my wife Becky who was always a bright spot and brought our wonderful son into the world during my studies. Many thanks also to my dad Jerry and sister Rachel, who helped me realize chemistry is not so bad, and to my mother Cora Jean who ceaselessly encourages and teaches.

Andrew J. Leenheer

December 2012

Pasadena, California

“Without counsel, plans go awry,

but in the multitude of counselors they are established.” Proverbs 15:22

Abstract

Photoelectrochemical devices can store solar energy as chemical bonds in fuels, but more control over the materials involved is needed for economic feasibility. Both efficient capture of photon energy into electron energy and subsequent electron transfer and bond formation are necessary, and this thesis explores various steps of the process. To look at the electrochemical fuel formation step, the spatially-resolved reaction rate on a water-splitting electrode was imaged during operation at a few-micron scale using optical microscopy. One method involved localized excitation of a semiconductor photoanode and recording the growth rate of bubbles to determine the local reaction rate. A second method imaged the reactant profile with a pH-sensitive fluorophore in the electrolyte to determine the local three-dimensional pH profile at patterned electrocatalysts in a confocal microscope. These methods provide insight on surface features optimal for efficient electron transfer into fuel products.

A second set of studies examined the initial process of photoexcited electron transport and collection. An independent method to measure the minority carrier diffusion length in semiconductor photoelectrodes was developed, in which a wedge geometry is back illuminated with a small scanned spot. The diffusion length can be determined from the exponential decrease of photocurrent with thickness, and the method was demonstrated on solid-state silicon wedge diodes, as well as tungsten oxide thin-film wedge photoanodes. Finally, the possibility of absorbing and collecting sub-bandgap illumination via plasmon-enhanced hot carrier internal photoemission was modeled to predict the energy conversion efficiency. The effect of photon polarization on emission yield was experimentally tested using gold nanoantennas buried in silicon, and the correlation was found to be small.

Contents

Acknowledgments	iv
Abstract	vii
List of Publications	xi
List of Figures	xiii
List of Tables	xiv
1 Introduction	1
1.1 World energy needs and solar energy conversion	1
1.1.1 Renewable energy economics	3
1.1.2 Solar cell efficiency	4
1.2 Solar fuels	6
1.2.1 Semiconductor photoelectrochemistry	7
1.2.2 Surface structure and catalysis	9
1.2.3 Light absorption and diffusion length	10
1.3 Contents of this thesis	11
2 Water splitting reaction rate measured via bubble growth at laser-illuminated SrTiO₃	13
2.1 Introduction	13
2.2 Strontium titanate photoanode preparation	15
2.3 Bubble growth measurement and analysis	15

2.3.1	Calculation of gas supersaturation before nucleation	20
2.4	Bubble effects on photocurrent	25
2.5	Conclusion	26
3	Water splitting reaction rate measured via laser-scanning confocal fluorescence pH imaging	28
3.1	Introduction	28
3.2	Sample fabrication	30
3.3	Flow cell design for microscope	31
3.4	Imaging pH changes	33
3.5	Numerical simulation of pH increase	39
3.6	Conclusions	42
4	Photoelectrode minority carrier diffusion length measured via wedge geometry	44
4.1	Introduction	44
4.1.1	Theory and choice of wedge geometry	46
4.1.2	Assumptions and requirements	51
4.2	Fabrication of materials in the wedge geometry	55
4.2.1	Polishing silicon into a wedge	55
4.2.2	Sputtering WO_3 under a shutter	56
4.2.3	Polishing films at an angle	63
4.3	Diffusion length measurement: Photocurrent with scanned illumination	65
4.3.1	Silicon wedge	67
4.3.2	Tungsten oxide wedges	68
4.4	Conclusion	73
5	Plasmonic hot carrier internal photoemission for energy conversion	75
5.1	Introduction	75
5.2	Theory of plasmon-enhanced internal photoemission	79
5.2.1	Hot electron excitation	80

5.2.2	Hot electron transport	83
5.2.3	Hot electron emission	84
5.2.4	Fowler yield and extensions	86
5.2.5	Voltage dependence and power conversion efficiency	87
5.2.6	Geometrical considerations	94
5.2.7	Unique properties of plasmons	94
5.2.8	Alternate sources of subgap photocurrent	96
5.2.8.1	Pseudo-internal photoemission	96
5.2.8.2	Thermionic emission from temperature gradient . . .	99
5.3	Numerical simulations	99
5.4	Experiment: Is yield correlated with polarization?	102
5.4.1	Reproducing dipole antenna response	103
5.4.2	Angled illumination to add p-polarization	106
5.4.3	Buried antenna geometry	106
5.4.4	Buried antenna fabrication and responsivity	108
5.4.5	The role of the titanium	114
5.5	Summary	115
6	Summary and outlook	117
A	Steady-state solution to Poisson's equation for Gaussian source	122
B	Mathematica code for diffusion length calculations	124
	Bibliography	125

List of Publications

Portions of this thesis have been drawn from the following publications:

- A.J. Leenheer and H.A. Atwater, “Water-Splitting Photoelectrolysis Reaction Rate via Microscopic Imaging of Evolved Oxygen Bubbles.” *J. Electrochem. Soc.* **157** B1290 (2010). doi:10.1149/1.3462997 (Chapter 2)
- A.J. Leenheer and H.A. Atwater, “Imaging Water-Splitting Electrocatalysts with pH-Sensing Confocal Fluorescence Microscopy.” *J. Electrochem. Soc.* **159** H752 (2012). doi:10.1149/2.022209jes (Chapter 3)

List of Figures

1.1	Levelized cost of electricity for various energy sources	4
1.2	Solar cell efficiency losses	5
1.3	Photoelectrochemical band diagram for water splitting	8
2.1	Schematic of the experimental setup to measure bubble evolution . . .	16
2.2	Bubble video processing workflow	18
2.3	Bubble growth time series	18
2.4	Photocurrent detail of bubble series	19
2.5	Comparison of gas evolution measurements	20
2.6	Dissolved oxygen profile calculation	22
2.7	Ray-tracing optical simulations of a bubble	27
3.1	Flow cell schematic for confocal microscopy	32
3.2	Fluorescence emission ratio of BCECF dye	34
3.3	pH profile around cloverleaf patterned Au electrocatalysts	35
3.4	pH increase around arrays of Au circles	37
3.5	pH increase near various electrocatalysts in parallel	39
4.1	Geometry for diffusion length calculations	48
4.2	Simulated spectral response measurement of diffusion length	49
4.3	Calculated photocurrent for wedge geometry diffusion length measurement	51
4.4	Photocurrent and diffusion length for various cases of wedge material properties	52
4.5	Pore geometry for photocurrent correction	54
4.6	Expected photocurrent behavior with pores	54

4.7	Sputter deposition setup for thin film wedge fabrication	57
4.8	Optical determination of sputtered film thickness profile	58
4.9	SEM images of tungsten oxide deposited at varied temperature	59
4.10	X-ray diffraction of WO_3 films	60
4.11	Top surface morphology of polished WO_3	62
4.12	Optical properties of WO_3 films	64
4.13	Illumination and cell setup to scan illumination across an electrode. . .	66
4.14	Silicon wedge photocurrent	68
4.15	Tungsten oxide cyclic voltammetry	69
4.16	Photocurrent for dense tungsten oxide wedge	70
4.17	WO_3 wedge photocurrent dependence on voltage and effect of annealing	71
4.18	WO_3 photocurrent for wedge samples deposited at high temperature; effect of alumina insulation and polish	73
5.1	Internal photoemission band structure and escape cone	80
5.2	Hot electron energy distribution and mean free path	83
5.3	Band structure for IPE with applied voltage	88
5.4	Sample IPE calculations and considerations for a thin-film emitter . .	91
5.5	Pseudo-internal photoemission band diagram.	97
5.6	SEM of Au dipole antennas	104
5.7	Measurement apparatus schematic for testing responsivity	104
5.8	Responsivity of Au dipole antennas	105
5.9	Buried antenna schematic geometry.	107
5.10	Simulations of absorption and yield for buried antenna	109
5.11	SEM images of buried antenna arrays	111
5.12	Responsivity for buried antennas with both polarizations	113
5.13	Current-voltage behavior of Au/Ti/Si and Au/Si diodes	115

List of Tables

5.1	Efficiency for internal photoemission solar energy conversion devices . . .	92
5.2	External quantum yield for various internal photoemission geometries . .	101

Chapter 1

Introduction

1.1 World energy needs and solar energy conversion

Throughout human history, advances in energy utilization have led to increased comfort, lifespan, and freedom for those consuming the energy. In the development of agriculture, energy in biomass was more efficiently harvested, and via domestication the mechanical advantage of large animals was harnessed. However, in the preindustrial world one of the most useful forms of energy was obtained from harnessing other humans in slavery [1], as the 2000 (kilo)calorie daily dietary energy requirement works out to about 100 W power consumption per person. Even if only a small amount of that power can be harnessed, in ancient times slavery was a primary means of constructing civilization and achieving comfort for the masters. However, even in ancient Greece it was recognized that machines would be able to end slavery, as Aristotle wrote in *Politics* [2], “We can imagine a situation in which each instrument could do its own work, at the word of command or by intelligent anticipation...a shuttle would then weave of itself, and a plectrum would do its own harp-playing. In this situation managers would not need subordinates and masters would not need slaves.” Though some wind power and hydropower were increasingly used over time, it was not until the industrial revolution in the mid-eighteenth century that the great amount of energy buried in carbon-rich fossil fuels was exploited to provide abundant and inexpensive energy for humanity [3] and the prevalence of slavery quickly declined. Though worldwide energy equality is still a work in progress, the technology devel-

opment that allowed fossil fuels usage has enabled an explosion of population and comfort allowing the pursuit of happiness rather than simple survival, and Aristotle's vision is practically realized in many developed countries.

Fossil fuels provide a marvelously dense form of stored energy. Most of the freely available energy on the earth's surface comes from the sun, either directly as radiation or as a precursor to mechanical energy available in wind and hydropower [4]; an abundance of nuclear energy also exists but is difficult to safely use. The world power usage as of 2011 was 17.7 TW on average and is projected to rise to over 24 TW by as soon as 2030, and over 83% of the current energy usage is from fossil fuels consisting of roughly equal parts liquid petroleum, coal, and natural gas [5]. Solar radiation could easily fulfill these energy requirements, as the irradiance over the earth's surface is about 10^5 TW [6]. However, solar energy is diffuse and cyclic, with a daily average irradiance of only about $250 \text{ W m}^{-2}\text{day}^{-1}$, equivalent to 21.6 MJ/m^2 , and with a device to capture 20% of that energy about 4 MJ/m^2 is available. In comparison, the energy in an inexpensive and portable gallon of gasoline is 130 MJ/gal . At this point in history we are fortunate to be able to mine the result of millions of years of biological energy capture, for even though the solar energy conversion efficiency of plants is typically below 1% [7], over time huge reserves of biomass energy have been buried and not utilized until the last couple of centuries.

The fossil fuel solution to the world's energy use is not a permanent situation, however. Concerns about "peak oil" have been mentioned for the last few decades anticipating the point when demand for oil exceeds the maximum rate of production; however, discovery of new reserves of oil and gas as well as improved extraction techniques for shale oil and hydraulic fracking to collect natural gas have lessened the concerns about the amount of recoverable fossil fuels available [3], and the United States is even on track to become a net oil exporter by 2030 [8]. However, it has been recently found that massive consumption of fossil fuels is not without consequence, for carbon that was buried for millions of years is being emitted into the atmosphere as carbon dioxide, a greenhouse gas. The full implications are unknown, but climate modeling has predicted global temperature increases of 2-4 °C over the next century,

rising sea levels, and ocean acidification [9], and the residence time of CO₂ in the atmosphere is on the scale of millennia [6] so any action or inaction at present will be affecting the planet for a long time. Now is the time to transition to alternative sources of energy with less potential for harm even though plenty of fossil energy is still available—“the Stone Age did not end because we ran out of stones” [3]. Though humanity should be able to adapt to a changing climate, the costs are likely to be high. The global nature of the problem means that those who suffer the most are not necessarily those who use the most energy, as it is the poorer countries that will have more difficulty adapting; although not as direct as slavery, continued use of fossil fuels involves the rich exploiting the poor.

1.1.1 Renewable energy economics

The present limited use of renewable sources of energy is due to simple economics, for it is more expensive to harness the diffuse alternative energy sources compared to fossil fuels. One area in which renewable energy can make inroads is in electricity, which is a high-value form of energy, and many renewable technologies directly generate electricity. The 2012 levelized cost of electricity is presented in Figure 1.1 which represents the price at which it must be sold to recoup the costs of generation. Though natural gas combined-cycle plants together with coal-fired plants are the least expensive, various alternative energy technologies are becoming economically competitive. In particular, onshore wind is presently less expensive than fossil fuel sources in some markets; however, the total global wind potential only amounts to 2 TW [10]. Similarly, though biomass and geothermal are sometimes economically competitive, the resource reserve for each is only 7 and 11.6 TW, respectively. In contrast, solar energy technologies are quickly coming down in price, and the reserve of economically viable solar electricity is 60 TW, so it is set to become a dominant player in the electrical energy market. If the indirect costs of fossil fuels from pollution and carbon emission were recognized and taxed as such, solar would become even more attractive.

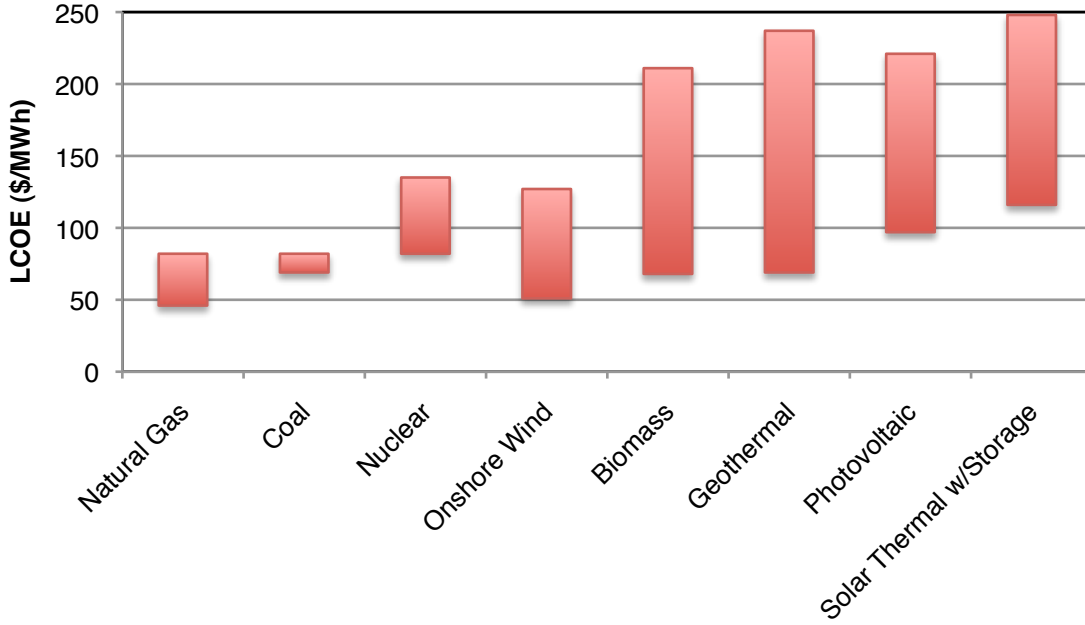


Figure 1.1 – Levelized cost of electricity (LCOE) ranges for various electrical energy sources in 2012. Data adapted from [11].

1.1.2 Solar cell efficiency

For photovoltaic cells, almost half of the electricity cost comes from installation and balance of systems cost [12], and the material cost of the module is becoming less of the overall cost. Therefore, the energy conversion efficiency of photovoltaics is a critical parameter to improve, for even if an inefficient cell is inexpensive to manufacture, it may not be economical once installed. Gains in efficiency are achieved through basic research in the device physics and materials science of the semiconductors involved. Traditional single-junction photovoltaic cells are nearing the thermodynamic limits for device efficiency, with single-crystal Si and GaAs cells reaching 25% and 28.8% efficiency, respectively, under one-sun illumination [13] compared to the theoretical limit of about 33% for those materials' bandgaps. Further efficiency improvements for these types of solar cells require approaches that overcome the limiting assumptions in the Shockley-Queisser analysis [14].

Two limits that severely restrict device efficiency are shown in Figure 1.2(a), where photons of different energy enter a light-absorbing semiconductor device. Photons of

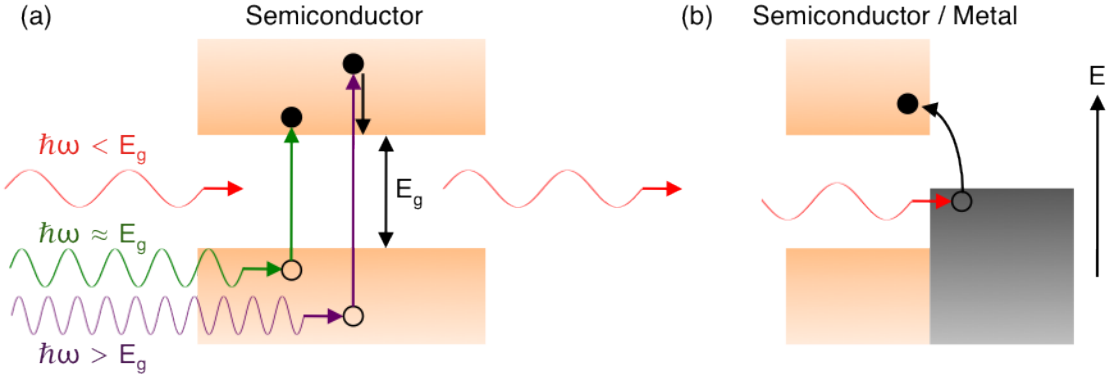


Figure 1.2 – (a) Solar cell efficiency losses from low-energy photon transmission and high-energy electron-hole thermalization. (b) Collection of sub-bandgap illumination via metallic hot carrier internal photoemission.

energy $\hbar\omega$ below the bandgap energy E_g are simply not absorbed, while photons of energy much larger than the bandgap energy excite electron-hole pairs that end up thermalizing to only retain the bandgap energy, so the excess is lost. In the device, the right balance of solar spectrum absorption and electron-hole pair energy is needed for high efficiency, and the optimal bandgap is around 1.1-1.4 eV as is the case for Si and GaAs with efficiencies in the range of 30-40% depending on the conditions. Achieving higher efficiencies (per semiconductor absorber material) requires either utilization of the energy lost during thermalization or a way to absorb and collect the sub-bandgap illumination. One technique to achieve the former is via so-called “hot carrier solar cells” [15] in which an excited electron or hole is collected before thermalization, which requires energy-selective contacts and reduction of hot-electron-phonon coupling, both of which are difficult to achieve. In Chapter 5 of this thesis, we explore a different hot carrier phenomenon in which photons are absorbed in a metal adjacent to a semiconductor, and hot electrons from the metal are emitted into the semiconductor before thermalization as shown in Figure 1.2(b); in this case the goal is to collect the photons with energy less than E_g via internal photoemission.

1.2 Solar fuels

Electricity presently comprises only about 40% of the world's total energy use, and fuel for transportation comprises about another 20% [5]. Thus, even if renewable energy technologies largely replace fossil fuel electricity generation, the need for transportation fuels will still require a large amount of fossil fuel energy unless an alternative source of fuel can be found. Battery technology can help store and transport electricity, but the energy density and speed of refilling for current batteries do not come close to that possible with hydrocarbon fuels. In addition, wind and solar sources for renewable electricity are intermittent by nature, and large-scale methods for electricity storage are needed if renewable electricity is to replace natural gas and coal. Pumped hydraulic power and compressed air are inexpensive ways to store energy, but if storage is to be scaled up to the terawatt scale, capturing the energy in the chemical bonds of a fuel is much more attractive [6].

Renewable fuel generation is possible by various routes. Perhaps the simplest is via biofuels, converting the sugars in plants to alcohols or other hydrocarbons, but the aforementioned low efficiencies of plants means that the total power available in biofuels is perhaps only 5 TW [6]. Thermochemical cycles can directly reduce CO₂ or H₂O using heat from either solar or nuclear power [16], but the high temperatures and sometimes corrosive chemicals involved pose difficult challenges for the materials making up the reactors. A very attractive option is electrochemical water splitting because of the abundant feedstock (water) and flexible product, hydrogen fuel which stores a free energy of 1.23 eV per molecule. Electrolyzers can operate between 65-90% efficiency [17], and the hydrogen produced can either be used to again make electricity in a fuel cell or as a feedstock along with a source of carbon to make a carbon-neutral hydrocarbon fuel. Again, however, the cost becomes a limit, and the total capital cost of a renewable electricity source as well as the electrolyzer means that renewable hydrogen production cannot currently compete with hydrogen from methane steam-reforming [18]. A more direct route is to copy (and improve upon) the natural process of photosynthesis in which photons excite electron-hole pairs in a

protein photosystem complex that are separated via a series of electron transfer steps with the electron eventually reducing CO_2 to sugars and the hole oxidizing water to O_2 . In an ideal solar fuels device, the input is light and water, and the direct output is the fuel with solar energy stored in the chemical bonds. By combining all the processes into one hopefully simple device, the cost of hydrogen may eventually be less than the fossil fuel route [19].

1.2.1 Semiconductor photoelectrochemistry

A way to mimic photosynthesis is through semiconductor photoelectrochemistry (PEC), which shares many similarities to a photovoltaic cell coupled to an electrolyzer but in only one device. Essentially, instead of contacting a solar cell with wires to collect the voltage generated by light, the semiconductor is contacted with a liquid and the voltage is used to induce a chemical reaction. A key difference occurs if the liquid is used to form a junction. In a solid-state photovoltaic cell, a junction between materials with different chemical potentials is used to separate photogenerated electron-hole pairs, and this semiconductor junction formation can be difficult to form or require high-temperature processing steps. A liquid can instead be used to form the junction if a redox couple is present in solution that can exchange electrons with the semiconductor, and again the electric fields built up at this interface from the chemical potential difference can separate and collect photogenerated electrons. The ease of junction formation is an advantage in semiconductor photoelectrochemistry [20]. However, in this case an electron-transfer chemical reaction must occur at the semiconductor surface as well, and the energetic positions of the semiconductor bands at the surface relative to the redox potential affect the charge separation efficiency.

A diagram of the device band structure for a photoelectrochemical water-splitting cell is shown in Figure 1.3 which is based on the standard model for semiconductor photoelectrochemistry [21, 22]. This cell is similar to the first demonstration of water splitting with a semiconductor by Fujishima and Honda [23] with a n-type TiO_2 photoanode. In the dark, the semiconductor bands bend upward due to equilibra-

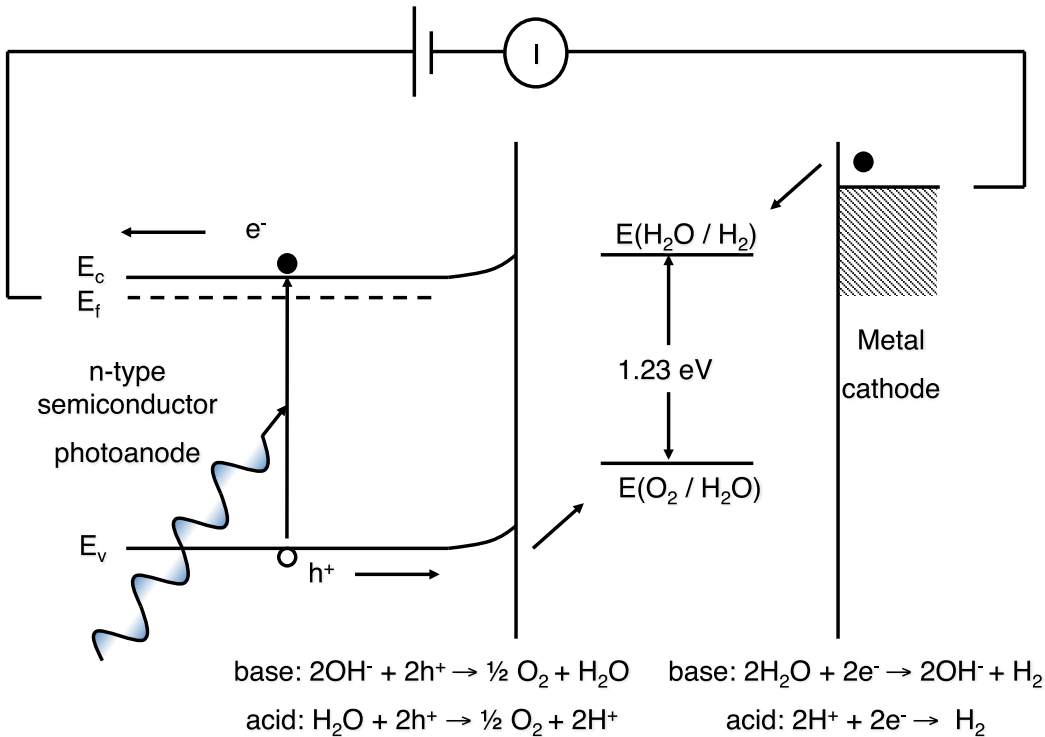


Figure 1.3 – Photoelectrochemical band diagram for water splitting with an illuminated n-type photoanode semiconductor and metal counter-electrode, with positive bias applied to the semiconductor. The dominant chemical reactions are shown for both basic and acidic conditions.

tion with the solution potential, and under illumination the band bending in the semiconductor depletion region sweeps minority-charge-carrier holes to the sample surface where they either oxidize water molecules or hydroxyl ions to evolve oxygen. At the counter-electrode, the photogenerated electrons reduce either protons or water molecules to evolve hydrogen.

No known semiconductor satisfies all the requirements for efficient, stable, and inexpensive operation. For a single-semiconductor device, the bandgap of the absorber should be above 2 eV to allow the thermodynamic requirement of 1.23 eV to split water as well as reaction and charge separation overpotentials and entropic losses which limits the energy conversion efficiency to about 17% [24] because of the poor utilization of the solar spectrum. A tandem system with a second semiconductor absorber offers more flexibility where an efficiency of 27% can be reached with a semiconductor bandgap combination of 1.7 eV and 1.1 eV. A few photocathode semiconductors with

bandgaps near 1 eV are available such as Si, InP, and WSe₂ that show reasonable stability, but the discovery of a stable photoanode with a bandgap near 1.7 eV has been elusive [25] and is a main thrust of the Joint Center for Artificial Photosynthesis. Most covalent or compound semiconductors are unstable against oxidation because the photoexcited holes have enough energy to oxidize and corrode the semiconductor itself in the presence of water [26]; some oxide semiconductors are stable but typically have bandgaps above 2.5 eV.

1.2.2 Surface structure and catalysis

Beyond just absorbing light and delivering minority carriers to the semiconductor surface, a PEC device must also be able to perform the chemical reaction involved. Otherwise, the photoexcited electron-hole pairs will recombine before being captured in chemical bonds. For water splitting, both hydrogen evolution and oxygen evolution are multi-electron transfer reactions with a variety of mechanisms active depending on the pH and surface chemistry. Oxygen evolution in particular is a difficult reaction, with overpotentials of 300-400 mV necessary to match the current from solar illumination. Usually the semiconductor light absorber is not a great electrocatalyst, so a heterogeneous co-catalyst can be attached to the semiconductor surface to lower the overpotential for gas evolution [27]. Even if the semiconductor material is a good catalyst itself such as some perovskites and layered chalcogenides, the presence of step edges and edge sites can be most active [28]. The co-catalyst should aid the chemical reaction, but since it is located at the semiconductor/liquid interface, care must be taken not to detrimentally affect the liquid junction. Additionally, the catalyst should not parasitically absorb light that would be absorbed in the semiconductor.

To most effectively perform the chemical reaction at the semiconductor surface, the interface and co-catalyst is often nanostructured to obtain a large interfacial area and variety of chemical environments to allow bonding and desorption of the various reactants, intermediates, and products. Rather than just measuring the ensemble average of the behavior of an entire electrode surface, more useful information can be

obtained by imaging the spatial variation in the chemical reaction rate over the sample surface. The first part of this thesis is devoted to developing microscopic methods to optically image the differences in local reaction rates on both photoelectrodes and dark electrodes patterned with metallic electrocatalysts. The ability to view differences in reaction rates from various patterned features on a given electrode *in situ* will allow development of the optimal surface structure for a solar fuels device.

The activity of an electrode can be mapped with scanning electrochemical microscopy in which a nanoscale metal electrode is brought close to the electrode and scanned while measuring current or potential [29]. However, the presence of the probe can perturb the experiment, and samples must have little variation in topography because the probe is usually scanned at constant height. The goal here was to develop noninvasive methods that would allow microscopic imaging of water splitting on electrodes with arbitrary morphologies.

1.2.3 Light absorption and diffusion length

As light is absorbed by a semiconductor, the intensity exponentially decreases and the decay is described by the absorption coefficient α . If the absorption length $1/\alpha$ is longer than the depletion width, electron-hole pairs are generated in a quasineutral region where there is no driving force for charge separation and collection. The excited carriers diffuse around the quasineutral region either until they recombine within a characteristic dimension called the diffusion length or until they are collected by the junction. If the absorption length is much longer than the diffusion length, excited charge carriers will be lost and the photon energy not collected. The right balance of absorption depth and diffusion length is necessary for efficient device operation and low cost. The absorption coefficient is a fundamental parameter of the semiconductor, and modification of the spatial location of photon absorption can only be done with various optical scattering strategies [14]. On the other hand, the diffusion length is both a fundamental property of the material and a function of its purity, and long diffusion lengths can be obtained with more perfect materials.

In the search for an ideal water-splitting photoanode, the diffusion length is an important parameter to know for promising material candidates as it can be a limiting factor. For example, hematite appears to be an ideal photoanode with a bandgap around 2 eV, good stability, and band edge positions straddling the water oxidation and reduction potentials, but its very short diffusion length of 2-4 nm compared to the absorption length of about 100 nm causes poor performance [30]. As new semiconductors are synthesized, a straightforward, independent measurement of diffusion length is needed, and the development of such a technique is described in Chapter 4. Once the diffusion length and absorption coefficient are both known, the material can be micro- or nano-structured as necessary to place the junction within a diffusion length of the carrier generation location.

1.3 Contents of this thesis

Though a variety of projects were tackled in this thesis, each study was aimed at more efficiently capturing solar radiation in chemical bonds whether by developing characterization techniques for PEC cells or by exploring new ways to more efficiently utilize absorbed photons.

- In Chapter 2, the localized oxygen evolution rate on strontium titanate photoanodes is measured in a microscope by imaging the bubbles resulting from gas evolution near a focused laser spot. The bubble growth rate was found to have a good agreement with the product formation expected from the measurement of photocurrent, so imaging the bubbles provided a good measurement of the actual amount of product formed. However, for studying structured electrodes, the bubble could be an interference, and the effects of the bubble on the photocurrent and illumination were considered.
- In Chapter 3, a method to image the localized reactant concentration near a hydrogen-evolving electrode was developed in an effort to avoid the complications of bubbles. A fluorescent pH indicator added to the electrolyte allowed

quantitative, three-dimensional imaging of proton concentration near a patterned hydrogen-evolving electrode in a confocal microscope. A flow cell to fit in the microscope was used to overcome diffusion limitations and increase the resolution to near micron scale. Modeling of the cell was also performed to solve the convection/diffusion equations via finite element software, the localized current density could be well compared to the experimental image.

- In Chapter 4, techniques to measure photogenerated carrier diffusion length are considered, and a new method for characterizing photoelectrodes is presented in which back-side illumination is scanned along a sample of graded thickness. The photocurrent decreases exponentially with increasing sample thickness, and for strongly absorbed light the exponential decay directly gives a measurement of the diffusion length. The method was demonstrated on both a silicon wedge and a tungsten oxide photoanode wedge, and a way to avoid the complications of sample porosity is presented.
- In Chapter 5, a more exotic mechanism for light absorption and collection is examined: plasmonic hot carrier emission from a metal into a semiconductor. Metallic hot carriers could enhance both photoelectrodes and catalysis, so here some of the basic physics were examined to determine plausible efficiencies. The theory of internal photoemission is outlined and applied here to plasmonic nanostructures, and estimates of the solar energy conversion efficiency were calculated to determine the possible collection of sub-bandgap photon energy. The efficiencies are found to be low unless hot carriers could be directed normal to the interface, so an experiment was designed to test for correlation between the photon polarization and hot carrier momentum.

Finally, Chapter 6 will summarize the work done and discuss possible future directions for research.

Chapter 2

Water splitting reaction rate measured via bubble growth at laser-illuminated SrTiO₃

To look at the spatial variation of gas evolution reaction rate on a semiconductor photoelectrode, the most straightforward test was to look at where the bubbles form on the surface. However, after a few initial tests of water photoelectrolysis with broad illumination, it became clear that on the gas production location and bubble nucleation location could be separated by hundreds of microns due to dissolved gas diffusion through the electrolyte. Instead, to study the local reaction rate, the above-bandgap illumination was focused to the micron scale, and the subsequent well-controlled bubble evolution rate near the spot of illumination was able to provide a localized reaction rate. This chapter details the measurement of bubbles in a microscope and the likely effects that bubbles have on a planar electrode.

2.1 Introduction

The production of hydrogen using solar energy to directly split water in a semiconductor photoelectrochemical cell is a promising source of carbon-free fuel [31], but many issues with the semiconductor-liquid interface remain. Semiconductors with bandgaps around 2 eV useful for absorbing the solar flux and possessing the necessary potential to split water [24] often suffer stability issues due to photo-excited

charge carriers corroding the semiconductor rather than transferring into the electrolyte [32]. Adding heterogeneous catalysts or structuring the electrode surface can provide more active sites for charge transfer, lowering the overpotentials required and possibly increasing stability, but the often the nature of the active sites is unknown [33, 34, 35, 36, 28, 37]. Traditional experimental techniques involve modifying or structuring the entire surface of a semiconductor photoelectrode and measuring the photocurrent under illumination; this method provides only the average reaction rate of all the various redox reactions occurring over the entire exposed surface. Localized methods that differentiate the activity on separate patterned areas on the same electrode could offer a wealth of information about the surface sites important for efficient charge transfer. Previous research has focused on utilizing a scanned electrochemical probe near the surface [29] that can even include local illumination through an optical fiber [38], a very useful but rather perturbative and difficult to implement method.

Examining the evolved gas bubbles could provide this type of local measurement by recording their growth rate at different surface features. Additionally, measuring the bubble and hence the actual gas produced differentiates between the gas-evolving reaction of interest and any parasitic corrosion reactions that can still contribute to the measured current. Optical microscopy of the photogenerated gas bubbles during their growth is a straightforward technique and provides a localized measurement of the reaction rate at various areas on a semiconductor surface.

As a model system to explore the use of this technique, we used n-type SrTiO₃ as a semiconductor photoanode to split water while observing the resulting oxygen bubbles with an inverted optical microscope. SrTiO₃ (strontium titanate), while not suitable for solar applications due to its wide 3.2 eV bandgap [39], is stable in aqueous environment with the conduction band energy high enough to reduce water to hydrogen gas [40, 41]. The lack of corrosion means that a simultaneous measurement of the current and bubble growth allows a comparison of the two methods. Since visible light does not generate charge carriers, the microscope illumination used for imaging is decoupled from the above-bandgap ultraviolet laser illumination, allowing the bubble nucleation and growth dynamics to be easily observed. We found that

indeed the water-splitting reaction rate can locally and quantitatively be determined from the recorded bubble size as a function of time.

2.2 Strontium titanate photoanode preparation

Single crystals of (100) SrTiO₃ were obtained from MTI Corp. and were colorless and transparent upon arrival. Samples were annealed at 1000 °C under 5% H₂/95% N₂ until they were bluish-black but still somewhat transparent, resulting in n-type conductivity [42]. A schematic of the experimental setup as well as a picture of the actual cell is shown in Figure 2.1. Electrochemical cells were fabricated by contacting the edges of a sample with indium gallium eutectic, silver adhesive paste, and a copper wire, then sealing the sample to the bottom of a plastic Petri dish with insulating epoxy (Torrseal, Varian Inc.) leaving only about 10 mm² of the SrTiO₃ surface exposed to electrolyte. After the epoxy cured, the sample was rinsed clean with isopropanol and deionized H₂O and blown dry with a N₂ stream. About 10 mL unstirred, oxygen-saturated reagent grade 1.6 M KOH in deionized water was used as electrolyte, and the cell was set up in the three-electrode configuration with a Pt gauze counter electrode and an Ag/AgCl in 3M NaCl reference electrode. A positive bias of 200 mV vs. V_{Ag/AgCl} was applied to the sample with a Gamry Reference 600 potentiostat to ensure solely O₂ evolution and maximize quantum yield at the SrTiO₃ surface, and the current flow was recorded using the potentiostat. An oxygen atmosphere was maintained by flowing pure oxygen into a transparent plastic enclosure that housed the entire cell. Photocurrent was measured by chopping the illumination at 5 Hz and measuring the current using a SRS SR830 lock-in amplifier.

2.3 Bubble growth measurement and analysis

The bubble evolution was observed in a Zeiss Axio Observer inverted microscope equipped with a 10x objective. Samples were illuminated from above both with transmitted visible light via a halogen lamp filtered through a 430 nm long-pass filter

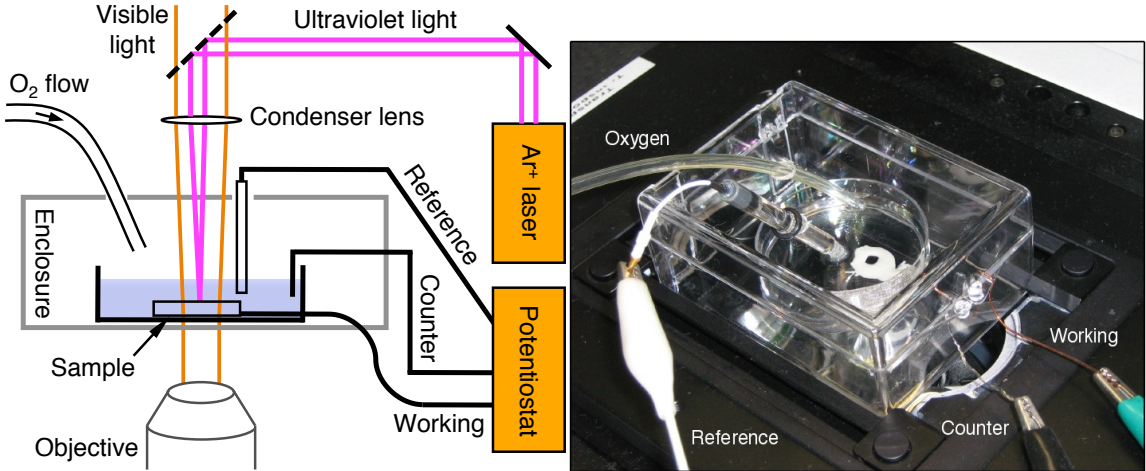


Figure 2.1 – Schematic of the experimental setup. Left: The sample was sealed to the bottom of a Petri dish filled with electrolyte, and the entire cell was enclosed in a transparent plastic box to maintain an oxygen atmosphere. A cube beamsplitter combined the visible illumination and ultraviolet laser. Right: Picture of the experimental cell setup: the oxygen flow tube and Ag/AgCl reference electrodes were introduced through the top of the plastic enclosure. Wires for the working and counter electrodes passed through the box seam. The white epoxy around the sample can be seen, but the platinum mesh counter-electrode is partly hidden.

and with above-bandgap radiation via the 351/364 nm lines of an argon ion laser focused to a small spot on the sample surface. The laser power was attenuated using neutral density filters and measured at the sample position with a Newport 1835-C power meter equipped with a UV-calibrated Si photodiode, and the power was monitored throughout the experiment. Videos were recorded at 30 frames per second using a black-and-white digital camera attached to the microscope. The laser spot size at the sample surface was measured using the camera, fitting the intensity to a Gaussian profile and using the $1/e$ value as the spot radius, $r_{laser} = 20 \mu\text{m}$. The laser beam was manually shuttered to control bubble evolution, and the microscope focus was slightly adjusted during growth to keep the outer bubble edges in focus. Calculations were performed using either Igor Pro or Mathematica software on a personal computer.

Illuminating the biased SrTiO₃ surface with ultraviolet laser light resulted in a few microamps of photocurrent, while the contribution from the visible halogen lamp illumination to the photocurrent was negligible. Focusing the laser to a 20 μm radius

spot with at least 37 μW beam power resulted in a single bubble nucleating and growing at the laser spot; however, lower intensities produced photocurrent but no bubble while extremely high intensities resulted in copious uncontrolled bubbling and noticeable local sample degradation. For conditions of single bubble growth, an example frame processing workflow is shown in Figure 2.2 where the video of bubble growth was digitally recorded and analyzed using image thresholding within IGOR Pro software to extract the bubble radius r_{bub} from each frame. A representative time series of the photocurrent, bubble radius, and calculated gas present in the bubble is shown in Figure 2.3, and the corresponding processed video can be found in online supplemental material [43]. An example of the bubble image and software edge recognition is shown in the inset of Figure 2; the bright spot seen in the bubble center is a result of the optical scattering of the bubble. Assuming for each bubble: (i) an approximately spherical shape, (ii) a composition of only gaseous oxygen and water molecules, (iii) a temperature of 298 K, and (iv) an internal pressure of 1 atm plus the Laplace pressure, the number of oxygen molecules inside the bubble was calculated using the ideal gas law,

$$N_{O_2} = \frac{(P_0 - P_{H_2O} + 2\gamma/r_{bub})}{kT} \frac{4}{3}\pi r_{bub}^3, \quad (2.1)$$

where $P_0 = 1$ atm is the ambient pressure, $P_{H_2O} = 0.033$ atm is the vapor pressure of water inside the bubble [44], $\gamma = 0.71$ atm- μm is the gas/liquid surface tension [44], k is Boltzmann's constant, and $T = 298$ K is the ambient temperature. At the counter electrode, bubbles were also evident that were presumably H_2 , but no attempt was made to identify the actual gas composition of any bubbles.

The rate of oxygen production at the photoanode and thus the water splitting rate could then be calculated in two ways, from either the photocurrent or the rate of bubble growth. For the traditional photocurrent measurement, Faraday's Law gives the oxygen evolution rate,

$$R_{O_2,cur} = \frac{I_{photo}}{qZ}, \quad (2.2)$$

where I_{photo} is the photocurrent, q is the charge of an electron, and $Z = 4$ is the

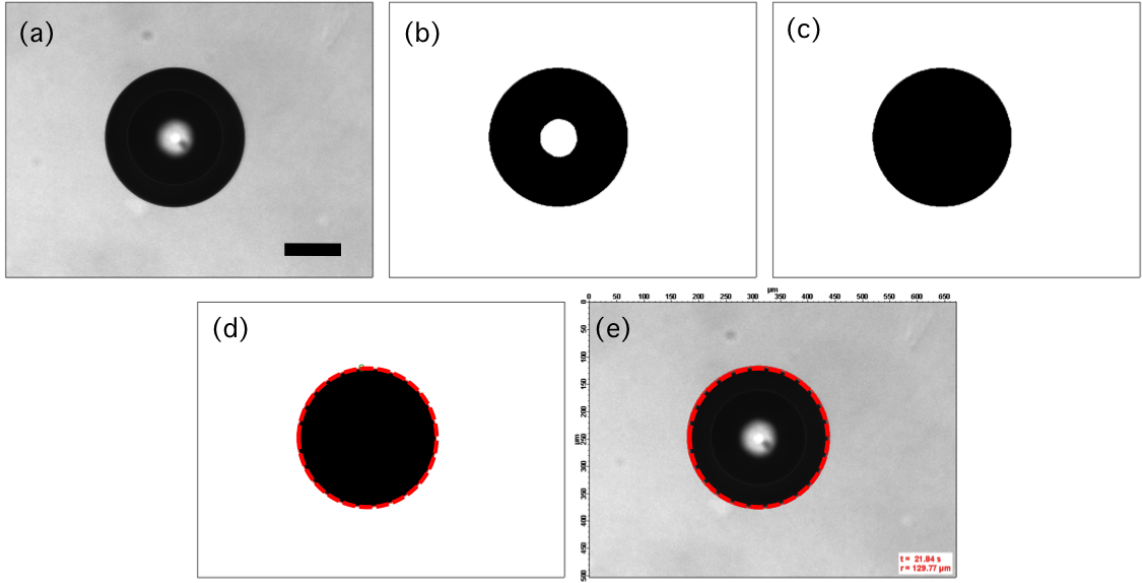


Figure 2.2 – Video processing workflow. (a) Extract movie frame, (b) threshold at a given darkness to create a binary image, (c) close the center hole via iterated opening and closing operations, (d) perform particle analysis to calculate bubble area and corresponding radius, (e) overlay the bubble perimeter on the original frame, increment the frame and repeat. Scale bar is 100 microns.

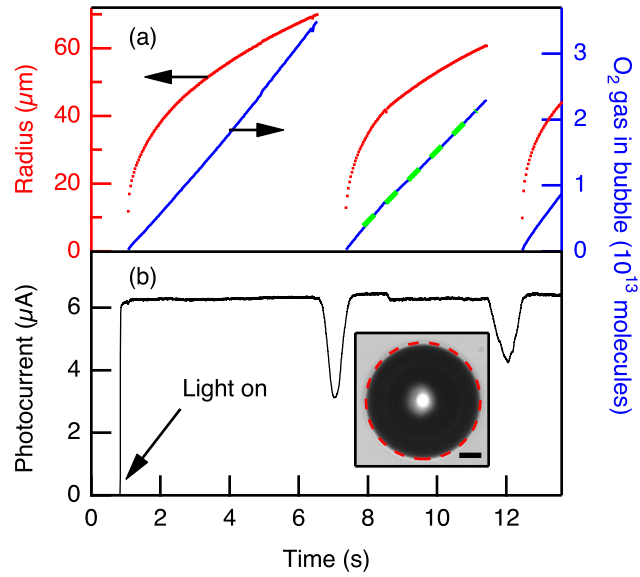


Figure 2.3 – Bubble growth time series. (a) Measured bubble radius and calculated gas present, and (b) photocurrent as a function of time at an irradiance of $1.8 \times 10^5 \text{ W/m}^2$. The dotted line in (a) is the fit whose slope gives the reaction rate. Inset: Example of an analyzed video frame with the bubble perimeter shown as a dotted line (10 μm scale bar).

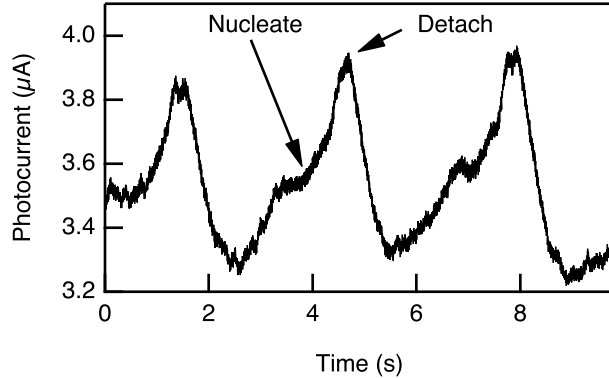


Figure 2.4 – Photocurrent detail for a series of bubble nucleation, growth, and departure sequences at $1.1 \times 10^5 \text{ W/m}^2$.

number of electrons transferred to evolve one oxygen molecule. Alternatively, the rate $R_{O_2,bub}$ can be calculated from the bubble growth by fitting a line to the N_{O_2} vs. time plot, as shown by the dotted line in Figure 2.3. It should also be noted that the photocurrent varied upon bubble nucleation and detachment, as shown in Figure 2.4. However, these variations were often small when compared with the overall photocurrent.

Within the intensity range that allowed single bubble nucleation and growth, the laser power was varied and the oxygen evolution rate averaged at various locations and for multiple bubbles on a single electrode; the results are shown in Figure 2.5(a). Here the laser power was converted to an approximate irradiance by dividing by the spot area πr_{laser}^2 . The minimum irradiance to nucleate a bubble was about $3 \times 10^4 \text{ W/m}^2$, where a few seconds of waiting time between bubbles existed. At irradiances below this, a bubble was first nucleated with more intense illumination, the laser was shuttered, the intensity was reduced, and the sample was again illuminated to measure the actual bubble growth. The remarkable agreement between the traditional current measurement method and the present bubble growth method shows the utility of recording bubble growth as a metric of the actual gas evolved, which can be especially useful for semiconductors that are susceptible to photocorrosion. As a more direct comparison, the external quantum yield Φ shown in Figure 2.5(b) was calculated

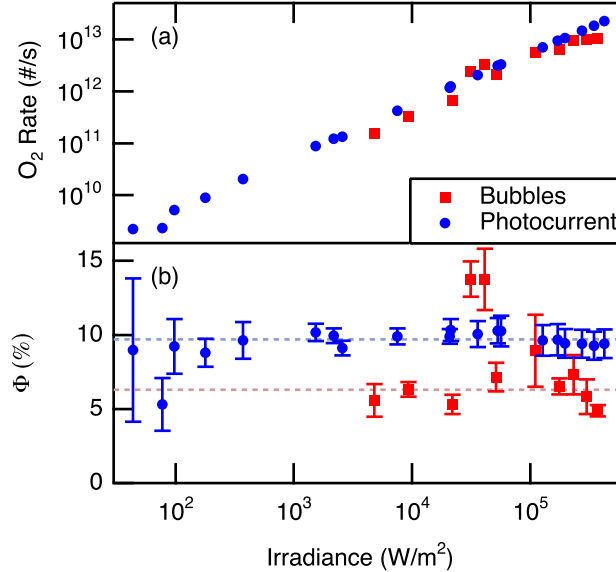


Figure 2.5 – Comparison of gas evolution measurements. (a) Oxygen production rate and (b) quantum yield Φ as a function of laser irradiance measured by the current (squares) and by the bubble growth rate (circles). The laser spot radius was $20 \mu\text{m}$. The dotted lines indicate the approximate quantum yields measured by the two methods.

using

$$\Phi = \frac{\# \text{ electrons utilized}}{\# \text{ incident photons}} = \frac{ZR_{O_2}}{P_{laser}/(hc/\lambda)} \quad (2.3)$$

where $\lambda \approx 360 \text{ nm}$ is the laser wavelength, P_{laser} is the laser power, h is Planck's constant and c is the speed of light. The error bars shown are the standard deviation of measurements done at multiple locations on the sample and with multiple bubbles. The error was higher for lower irradiances because of difficulty distinguishing the small photocurrent and low bubble growth rate from noise in the measurement.

2.3.1 Calculation of gas supersaturation before nucleation

To be able to quantify and analyze the gas evolution rate by examining bubble growth, conditions of single bubbles growing at the area of interest were desired. Bubble nucleation is highly dependent on the local properties of the surface, with pits and hydrophobic surfaces encouraging nucleation [45, 46]. However, we desired to decouple the sites of preferred bubble formation from the sites of enhanced gas evolution. Without introducing artificial nucleation sites nearby, it was necessary to use strong

local irradiation to overcome the diffusion of dissolved gases into the bulk electrolyte and achieve the local supersaturation necessary to form a bubble. Thus the irradiances seen in Figure 2.5 are much higher than in typical semiconductor photoelectrolysis studies [41, 47] and certainly higher than the ultraviolet above-bandgap solar irradiance. Even so, the remarkable agreement between the measurement of photocurrent and bubble growth for quantifying the reaction rate shows the usefulness of this alternative method. The overall rate and quantum efficiency appears slightly lower for the bubble measurement due to the tendency for the gas to enter solution either directly or via bubble shrinkage due to the Laplace pressure. Additionally, the photocurrent may be over-estimating the gas evolution rate due to possible parasitic side reactions.

The small illuminated area and non-optimized sample quality likely caused the overall low observed quantum efficiency Φ . Some photogenerated carriers are always lost due to recombination across the depletion region facilitated by traps. When the dark junction area is much larger than the illuminated area, excess carriers can diffuse away from the laser spot and be lost across the dark junction resulting in a considerable loss of photocurrent. At higher irradiances, other reasons for the low observed Φ likely include diffusion-limited current in the unstirred electrolyte, the relatively weak OH⁻ concentration [47] and low rates of charge transfer to oxidize H₂O, and possible Auger recombination under the high-level injection conditions with strong illumination (see below). The observed Φ agreed fairly well at high irradiances with previously reported data in a similar experiment that used a much larger laser spot of 1 mm [41].

To help analyze the conditions for bubble nucleation, simulations of the steady-state carrier generation rate in the semiconductor and dissolved oxygen profile in the electrolyte are shown in Figure 2.6 for experimental conditions under which the laser irradiance was just at the threshold for bubble formation. In the semiconductor, the charge carrier generation rate was calculated from

$$G_{carrier} = \frac{P_{laser}\lambda}{hc\pi r_{laser}^2} \alpha e^{-\alpha z} e^{-r^2/r_{laser}^2}, \quad (2.4)$$

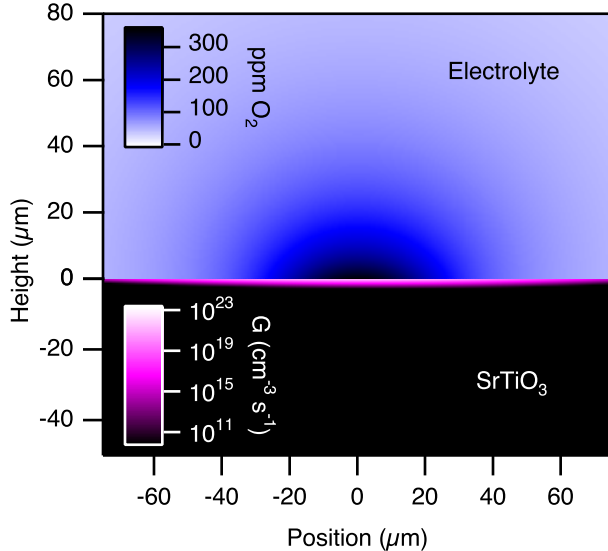


Figure 2.6 – Simulated steady state radial profiles of the dissolved oxygen in electrolyte (top) and the carrier generation rate in SrTiO_3 (bottom) for a Gaussian illumination profile. The laser irradiance was $3 \times 10^4 \text{ W/m}^2$ at a radius of $20 \mu\text{m}$, with an assumed $\Phi = 10\%$.

where $\alpha = 2.5 \times 10^4 \text{ cm}^{-1}$ is the absorption coefficient of SrTiO_3 at 360 nm [39]. The calculations of dissolved oxygen in the electrolyte follow the treatment of Lax for a Gaussian laser profile [48]; details are given in the appendix. It can be seen that the generation rate was over $10^{23} \text{ cm}^{-3} \text{ s}^{-1}$, possibly into high-level injection conditions depending on the carrier lifetime. Based on the measured Φ , we assumed that 10% of the photogenerated carriers are successful in oxidizing water and evolving dissolved oxygen that then diffuses away from the laser spot, resulting in the shown dissolved oxygen profile in the electrolyte. As the saturation condition for oxygen in water at 1 atm oxygen is about 40 ppm, these calculations indicate that a supersaturation of about 8x the saturation limit is approached before bubble nucleation. This observation is consistent with previous studies in which the supersaturation near gas-evolving electrode surfaces is often about 5 \times and as high as 100 \times the saturation limit due to the energetic barriers involved in bubble nucleation at smooth surfaces [49, 50, 51]. Indeed, the high concentrations of dissolved oxygen near the electrode surface can impede the water oxidation reaction, lowering Φ .

Once a bubble forms, it provides a sink for the gaseous products, quickly consum-

ing much of the nearby dissolved oxygen, especially under our experimental conditions where the laser is of comparable size or smaller than the bubble size. For the majority of a bubble's dwell time on the electrode, its radius seen in Figure 2.3 followed the relationship $r_{bub} \propto t^{1/3}$, indicating a “direct injection” of the evolved gas into the bubble from the electrode rather than bubble growth due to diffusion from the bulk electrolyte or liquid inertia [52]. However, near the limit of bubble nucleation, the relatively long waiting time between bubbles caused a build-up of dissolved gas and high bubble growth rate once nucleated, resulting in the higher apparent quantum efficiencies for laser irradiances near $4 \times 10^5 \text{ W/m}^2$ as seen in Figure 4(b). For these “nucleation-limited” conditions, the bubbles grew faster than the oxygen was being produced at the electrode surface.

It is useful to examine the assumptions made and possible associated errors in the simple calculation we used to quantify the amount of oxygen evolved. First, the ideal gas law was invoked for the bubble, while a more accurate calculation could use the van der Waals equation,

$$(P + \frac{N^2 a}{V^2})(V - Nb) = NkT, \quad (2.5)$$

where a and b are the van der Waals parameters for oxygen. Given the approximate pressure and volume of a typical bubble, the difference in the number of gas molecules for the ideal and van der Waals case was on the order of 1%, not large enough to be significant. Second, the partial pressure of oxygen in the bubble was corrected for the vapor pressure of water and the Laplace pressure (a small correction at a bubble radius greater than a micron or two), and the extra gravitational pressure of the liquid above the bubble was considered to be negligible. Though the gas composition was not measured, it is reasonable to assume that it is mostly oxygen because the standard model for photoelectrochemical cells [21] predicts that only holes will be available at the photoanode surface (especially with the extra +200 mV vs. V_{Ag/AgCl} applied bias) therefore only oxidizing water, not reducing it at the SrTiO₃. Third, the bubble volume was calculated assuming a sphere, though an actual bubble will have

a non-zero contact angle measured through the liquid and more of an oblate spheroid shape. However, we have estimated that the contact angle was small, perhaps about 5° at most (see below), so the amount of volume cut off by the solid interface was about 106 times smaller than the bubble volume, a very small correction. Also, previous studies that observe bubbles at water-splitting electrodes from the side show very close to a spherical shape [53]. Fourth, the temperature in the bubble was assumed to be ambient temperature, but the laser could possibly cause local heating and vaporization. Since the water and gas do not absorb the ultraviolet laser, the primary rise in temperature would be in the semiconductor. The temperature profile in a semiconductor irradiated with a Gaussian laser profile has been solved by Lax [48], with the maximum temperature rise ΔT_{max} in the center of the laser spot given in the appendix. Using $K = 11 \text{ W m}^{-1} \text{ K}^{-1}$ as the thermal conductivity of SrTiO₃ [54], the max temperature rise was only 0.64 °C even at the highest laser irradiances used (500 μW at 20 μm beam radius), not large enough to introduce a significant error in the gas calculation. Also, this calculation assumed no heat transfer to the liquid, so in reality the temperature rise will be even lower. The experimental uncertainties arising from averaging multiple measurements, calibrating distances in the microscope, and keeping the edge of the bubble in focus were the primary sources of error.

The primary drawback to this technique was the interference of the bubble with the area of study. Once a bubble was formed, the existence of a finite contact angle means that an area of the electrolyte/solid interface was excluded – unfortunately the same area illuminated by the focused laser beam. The contact angle, though difficult to measure in-situ with our experimental setup, can be estimated by balancing the buoyancy force of the bubble at its break-off radius in quiescent liquid with the adhering force resulting from surface tension. The equation obtained is the so-called Fritz equation for the contact angle θ in degrees [55],

$$\theta \approx 46.8r_{depart}\sqrt{\frac{g(\rho_L - \rho_G)}{\gamma}}, \quad (2.6)$$

where r_{depart} is the bubble radius at departure, g is the acceleration due to gravity, ρ_L

and ρ_G are the densities of the liquid and gas, respectively, and $\gamma = 0.072 \text{ N/m}$ is the surface tension between the liquid and gas [44]. For the typical observed break-off radii of 30-60 μm , the calculated contact angle was $0.5\text{-}1^\circ$, and the radius of the excluded photo electrode area was thus 0.25-1 μm . Occasional larger bubbles of 200 μm radius shielded up to a 20 μm radius area. This measurement of excluded area is comparable to the gas/solid interfacial area evident in the microscope for a large bubble. Note that the excluded area was comparable to the laser spot size used to nucleate a bubble. Only the illuminated areas within a minority carrier diffusion length of the liquid/solid interface could contribute to the gas evolution, so the presence of the bubble may lower the reaction rate. Since the bubble base blocks local sites of study from the electrolyte, this technique may not be well suited for comparing the reaction rate at various surface features, depending on the contact angle of the given semiconductor-electrolyte-gas system. Modifications to this technique could involve introducing separate nearby nucleation features such as rough Teflon fibers [46] or simply scanning the sample or laser beam and measuring photocurrent at different surface features.

2.4 Bubble effects on photocurrent

The variation of current seen in Figure 2.4 resulting from the bubble dynamics can be understood based on two mechanisms. First, with no bubble present, the high oxygen concentration near the electrode restricted the current to be diffusion-limited, then when a bubble nucleated, it provided a large sink for the oxygen, and the reaction could proceed at a higher rate (with the caveat of the excluded electrode area). Second, the optical effects of the bubble must be considered. Since the index of refraction inside the bubble was lower than the electrolyte, the bubble acted as a diverging lens to scatter the incident laser beam. Thus when the bubble detached and rose within the illuminating laser beam, it diverted light away from the sample, temporarily reducing the current. To illustrate the light scattering, radial intensity profiles of both a uniform and a Gaussian laser before and after scattering are shown

in Figure 2.7. This calculation was performed by sending many rays carrying intensities based on the value of r toward a spherical bubble tangent to the electrode surface, solving Snell's law at each interface using the indices of refraction for gas and electrolyte of 1 and 1.34, respectively, and histogramming the resultant intensities at the electrode surface. Effects of light polarization and reflection losses were not considered. In Figure 2.7(a), the incident laser intensity is constant as in the case of uniform illumination; it is easily seen that the bubble diverts light away from itself both due to refraction inside the bubble and total internal reflection in the liquid (and showing an apparent bright spot in the middle of the bubble). More relevant to the present experimental conditions is Figure 2.7(b), where an incident Gaussian laser profile with a radius smaller than the bubble radius is simply broadened by the scattering. Interestingly, the profile seen for the particular bubble radius chosen did not change as the bubble grows even larger because the increased distance from the surface offsets the lower bubble surface curvature. During its nucleation and growth, the bubble's lensing effects were quite evident in this experiment. In general, bubbles at photoelectrodes can hinder the flow of products and reactants, but the refraction of incident light away from the blocked area mitigates this effect.

2.5 Conclusion

By shining above-bandgap light on a semiconductor photoelectrode to form isolated, individual bubbles, we have shown that analyzing the bubble growth can provide a quantitative measure of the surface electrochemical reaction rate. Observing the evolved gas bubbles in an optical microscope can thus provide an alternative method for characterizing photoelectrode surfaces. Since SrTiO_3 is quite stable against photocorrosion, the reaction rate calculated from the photocurrent using Faraday's Law can be compared to the bubble growth rate, and the two methods showed quite good agreement. This method could be used for other semiconductors to characterize the relative rates of gas production and surface corrosion. However, the tendency for gas to diffuse away in solution rather than enter the bubble somewhat lowered the

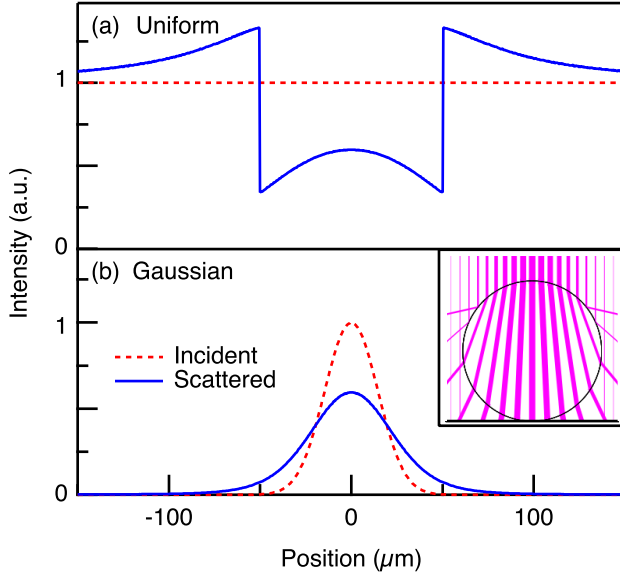


Figure 2.7 – Ray-tracing optical simulations of a bubble. The radial laser profile is shown after scattering by a 50 μm radius bubble for (a) a uniform incident profile and (b) a Gaussian incident profile with a 20 μm radius. Inset: Schematic of rays passing through bubble.

apparent reaction rate observed from the bubble.

The surface sites favorable for bubble nucleation are not necessarily the same surface sites with the best electron transfer rate, so we forced localized bubble nucleation by using a small laser spot with rather high irradiances. Simulating the dissolved gas profile, it was found that a supersaturation of about 8 \times was necessary to nucleate a bubble on the smooth surface. However, once a bubble was nucleated, the existence of a finite contact angle meant that a significant area of the illuminated interface was excluded from the electrolyte. Thus, this method may not be well suited for comparing the reaction rates at different surface features without introducing a separate nucleation site nearby. Future work could add a nearby pit or rough hydrophobic fiber to encourage bubble nucleation near a surface feature of interest. Patterning sub-millimeter areas of a semiconductor photoelectrode with different surface modifications (and nearby bubble nucleation sites) would allow the use of this method to compare, on one sample, the effects of heterogeneous catalysts or morphology changes.

Chapter 3

Water splitting reaction rate measured via laser-scanning confocal fluorescence pH imaging

While bubble evolution could measure the water-splitting reaction rate on a photo-electrode, it was determined that the presence of the bubble on the surface likely blocked many of the surface features under study. Instead, this chapter develops a method to image the reactant concentration rather than the product gas with a pH indicator fluorophore at current densities below that required for bubble formation. For demonstration, the pH imaging was done on patterned dark electrocatalyst surfaces, but the technique could be readily applied to photoelectrodes as well.

3.1 Introduction

There is a critical worldwide need for renewable energy sources, but many promising options such as solar or wind energy are intermittent by nature, with limited ability to produce dispatchable power on demand, thus limiting integration of renewables into the power grid. Storing energy in chemical bonds by using renewably generated electricity to split water could provide a clean and scalable fuel in hydrogen gas or in liquid hydrocarbons after further processing [31]. While current water electrolyzers can provide high efficiencies, they often use expensive catalysts and corrosive electrolytes [56], motivating research on electrocatalysts that can operate with

less overpotential and in neutral aqueous electrolyte. However, traditional catalyst characterization techniques rely on simple current-voltage curves which average the reaction rate over all exposed surface features of the electrode. In contrast, imaging the spatially resolved reactant or product concentration near the electrode reveals specific areas of high activity and reaction rate resulting from e.g. use of heterogeneous catalysts or high surface area electrode topology. While the evolved gas bubble growth rate can provide a good measure of the local reaction rate [43], bubbles do not necessarily nucleate near the surface features of interest and can block the flow of reactants. Scanning electrochemical microscopy (SECM) provides submicron resolution and many analytical capabilities, but the presence of the probe significantly perturbs the local environment [29]. Detecting the local pH at a water-splitting cathode indicates the consumed H⁺ and evolved OH⁻ concentrations, indirectly measuring the evolved H₂. pH changes near large platinum electrodes have been quantified by amperometric SECM, identifying both steady-state H₂ evolution as well as transient adsorption and surface oxidation features [57]. By using the potentiometric mode, three-dimensional pH profiles near micron-scale platinum electrodes have also been mapped with SECM with less perturbation [58, 59] but require the fabrication of a micron-scale ion selective tip and difficult tip-substrate distance feedback mechanisms.

Changes in pH can be detected not only electrochemically but also through the use of an pH indicator molecule. Conventional colorimetric pH indicators can be used [60, 61] but require an immobilization strategy if one desires limit the region of analysis to the electrolyte near the active electrode as has been done using thin films and waveguides [62]. Fluorescence-based pH indicators are experimentally more versatile and have been used to spatially image water oxidation [63] and compare electrocatalyst compositions in combinatorial libraries [64, 65]. If the indicator dye is present in the bulk electrolyte, dye above area of interest will also be visible resulting in a large background signal, but this contribution can be eliminated with confocal microscopy in the case of a fluorescent indicator.

We utilized a fluorescent pH indicator in an aqueous electrolyte and imaged the pH profile at a hydrogen-evolving electrode using a laser-scanning confocal microscope.

Previous studies have developed this technique [66, 67] showing three-dimensional diffusion profiles of increased pH in the diffusion layer near cathodic electrodes with resolution on the order of hundreds of microns in quiescent electrochemical cells and provided a semi-quantitative measurement of increased pH based on relative fluorescence intensity. Here we developed a flow cell to reduce the diffusion limitations and reveal three-dimensional product/reactant profiles at micron-scale resolution for varied surface features. The measurement of pH using confocal fluorescence has successfully been applied to refine other electrochemical models such as weak acid transport across a membrane [68] and the actual three-dimensional fluid flow near an impinging microjet [69]. The fluorescent pH indicator molecule is an organic molecule that protonates or deprotonates at a given pK_a value which changes its fluorescence properties. In previous work, fluorescein has commonly been used [66, 67, 68, 69, 70] because its absorption and fluorescence emission increases dramatically as pH increases from 4 to 8 [71]. However a purely intensity-based measurement is difficult to quantitatively calibrate and is subject to artifacts such as reflective surfaces, dye concentration, laser intensity variations, and shadowing. Therefore in this study we instead used a two-color dye, the fluorescein-derived ratiometric indicator 2',7'-bis-(2-carboxyethyl)-5-(and-6)-carboxyfluorescein (BCECF) which is often used in biological intracellular pH sensing [72] to enable quantitative pH measurement with few artifacts. The pH profiles are demonstrated on conductive glass patterned with micron-scale metal catalysts, metal catalysts patterned with varied surface area, and a comparison of multiple metals in parallel on one sample that revealed interesting electrochemical activity in conjunction with cyclic voltammetry.

3.2 Sample fabrication

Commercial F:SnO₂-coated glass (FTO) was obtained from Pilkington (TEC 15) and polished using Logitech SF-1 colloidal silica on a felt pad to serve as a smooth, transparent, conducting, and non-catalytic substrate cut into pieces about 1-2 cm². Electrode patterns were fabricated using standard electron-beam lithography or pho-

tolithography techniques followed by metal evaporation and lift-off. For photolithography, a 50 nm anti-reflective polymer layer (Brewer Science WiDe-15B) was spun on the FTO under the photoresist to eliminate back-reflections and overexposure; this layer was removed during the develop in base but remained during the lift-off in acetone. Hence, the bulk of the FTO surface was covered in polymer, with only a small 1 μm region of FTO exposed near the patterned metal catalyst. After patterning, one corner of the FTO was contacted with a copper wire and silver adhesive paste to complete the working electrode.

3.3 Flow cell design for microscope

A miniature electrochemical flow cell shown in Figure 3.1 was made to fit under the microscope objective, and consisted of the planar glass/FTO working electrode, a silicone gasket spacer, and a glass cover slip. The silicone gasket was cut from 0.7-mm-thick Press-to-Seal silicone (Grace Biolabs) and provided a watertight seal to the FTO/glass while allowing fast disassembly, cleaning, and reuse of the overall cell. The flow channel was cut from the silicone spacer to about 1 cm long by 1.5 mm wide. Two 1 mm holes were etched in a No. 1.5 cover slip at the flow channel ends, and bent stainless steel tubing was attached using epoxy for fluid input and output ports. The entire top coverslip was epoxied to a copper ring for support, and all epoxy joints were subsequently sealed with RTV-108 silicone. Additionally, a 100 μm -diameter Pt wire was placed between the input and output ports to act as a counter electrode. Galvanostatic current was applied with a Gamry Reference 600 potentiostat in the two-electrode configuration.

Buffered pH calibration solutions over the pH range 4.5-10 consisted of boric acid, citric acid, dipotassium phosphate, sodium sulfate, and sodium hydroxide adjusted to 200 mM total ionic strength in deionized water as well as 10 μM BCECF dye. The electrolyte during analysis consisted of 66 mM sodium sulfate (200 mM ionic strength) and 20 μM BCECF dye in deionized water. The initial bulk pH was adjusted using dilute sulfuric acid or sodium hydroxide. Flow was induced by using a syringe pump

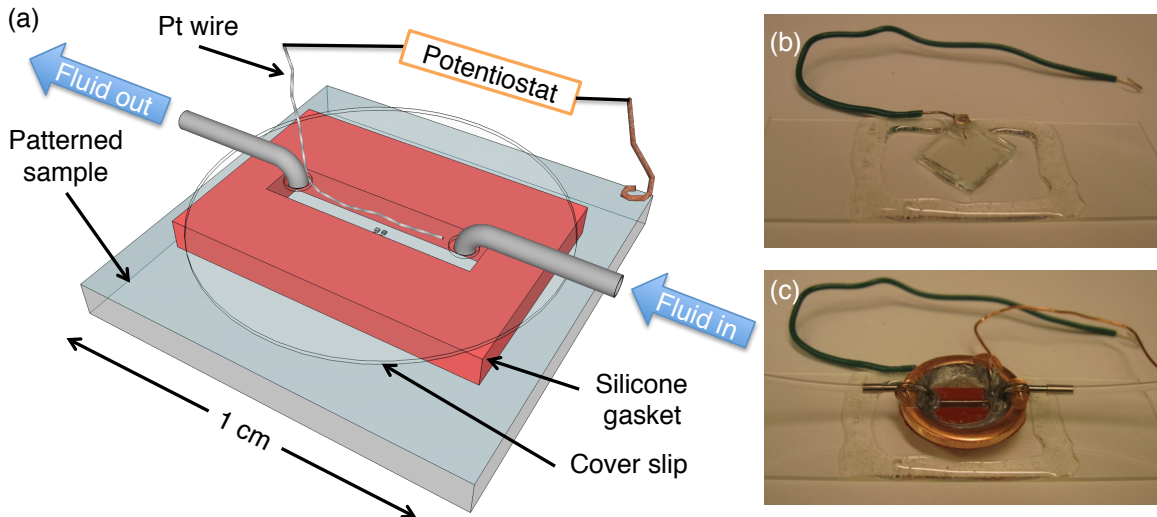


Figure 3.1 – Flow cell schematic for electrochemistry under the confocal microscope. (a) Sketch of the cell construction. (b) Image of a sample of patterned electrocatalysts (not visible) on a FTO square attached to a microscope slide. (c) Sample with the gasket and flow cell top assembly attached, ready for imaging.

to draw electrolyte through the flow cell connected with Tygon or polyethylene tubing and a glass rotameter to measure the flow rate.

A Zeiss LSM710 confocal laser-scanning head was attached to a Zeiss Axio Imager upright microscope equipped with a 20x, 1 NA water-immersion dipping objective lens. This objective provided a maximum field of view of about $500 \times 500 \mu\text{m}$. The excitation wavelengths alternated line-by-line between the 458 and 514 nm lines from an argon ion laser adjusted to an intensity that avoided dye saturation or bleaching [73], though the flow mitigated those effects. The emitted fluorescent light was collected by a photomultiplier tube for wavelengths from 525-720 nm through a confocal pinhole set to 1 Airy unit resulting in an optical slice thickness of about 2.2 micron. Additionally, laser light transmitted through the sample was collected via a transmitted-light photomultiplier tube to show the patterned catalyst location and geometry.

3.4 Imaging pH changes

The fluorophore BCECF exhibits a pH-sensitive fluorescence excitation spectra and has an isoemissive point at $\lambda = 435$ nm where the fluorescence intensity varies little with pH, whereas the largest change in fluorescence intensity with pH results from excitation at $\lambda = 500$ nm [72]. Thus exciting sequentially with the two different wavelengths and taking the ratio of emitted fluorescence gives a measure of pH which eliminates artifacts resulting from intensity variations present in both signals. The change in fluorescence is due to protonation/deprotonation of the molecule; for BCECF, the exchange is between the tetra-anion and penta-anion forms and occurs at $pK_a = 7$. Considering a linear combination of fluorescence of both the tetra-anion (basic) and penta-anion (acidic) forms present at a given pH with a first-order dissociation constant for the acid/base equilibria, the pH can be related to the fluorescence emission of two excitation wavelengths F_{λ_1} and F_{λ_2} as [74]

$$pH = pK_a - \log\left(\frac{R_b - R}{R - R_a} \times \frac{F_{b,\lambda_2}}{F_{a,\lambda_2}}\right), \quad (3.1)$$

where $R = F_{\lambda_1}/F_{\lambda_2}$ is the measured fluorescence ratio and subscripts a and b indicate values at acidic and basic endpoints, respectively. Only the pK_a of the indicator as well as fluorescence intensities in acid and base are required for calibration of this sigmoidal curve. In the confocal microscope used here, the best available laser excitation wavelengths were at $\lambda_1 = 514$ nm and $\lambda_2 = 458$ nm for the highest signal-to-noise ratio. Fig. 3.2 shows the relationship between the fluorescence ratio and pH for 20 μM BCECF in calibrated buffer solutions at constant ionic strength as well as endpoints in dilute sulfuric acid and sodium hydroxide. For the model fit, the dissociation constant of BCECF was empirically determined to be $pK_a = 7.05$ from the buffered solution at pH 6.5. Clearly, the fluorescence ratio quantitatively determines pH over the range 5.3 to 7.5, but beyond that range the noise and sigmoidal shape allow only upper or lower limits on pH. Other fluorophores with different pK_a values would enable detection over different pH ranges.

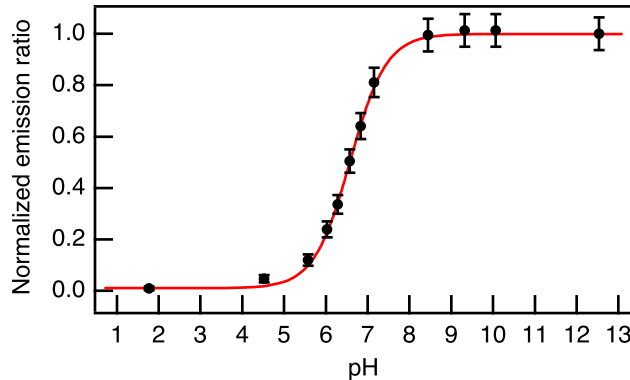
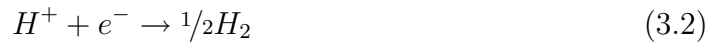


Figure 3.2 – Fluorescence emission ratio 514 nm/458 nm of 20 μM BCECF dye. Circles represent buffered solutions or dilute acid and base endpoints, and solid line shows model using $pK_a = 7.05$ and $F_{b,\lambda_2}/F_{a,\lambda_2} = 2.95$. Error bars indicate standard deviation of ratio largely due to shot noise.

The electrolyte during pH imaging was initially adjusted to pH 5.3 for the most sensitive measure of pH increase during water electrolysis, and 20 μM BCECF dye gave a strong fluorescent signal. Cyclic voltammetry curves (not shown) of this electrolyte showed only peaks related to water, indicating that the BCECF was stable and not prone to strong adsorption over the potential window of water electrolysis.

Initial tests of patterned electrodes in quiescent solution revealed diffusion profiles that approached hundreds of microns within seconds, so we adopted a flow cell geometry to aid convective transport. To test the resolution and demonstrate the technique, a glass/FTO electrode was patterned with a micron-scale cloverleaf of 100-nm-thick Au with a 3 nm Cr adhesion layer as shown in Fig. 3.3(a). Encircling each pattern is a small region of exposed FTO, and the rest of the electrode is protected from the electrolyte by WiDe polymer. Fig. 3.3(b) shows the pH profile resulting from -4 μA applied to the cloverleaf sample in the flow cell with 0.045 mL/min applied flow while tracking the BCECF fluorescence ratio.

Clear increases in pH are seen near the Au electrocatalyst where hydrogen is being evolved according to the proton reduction reaction



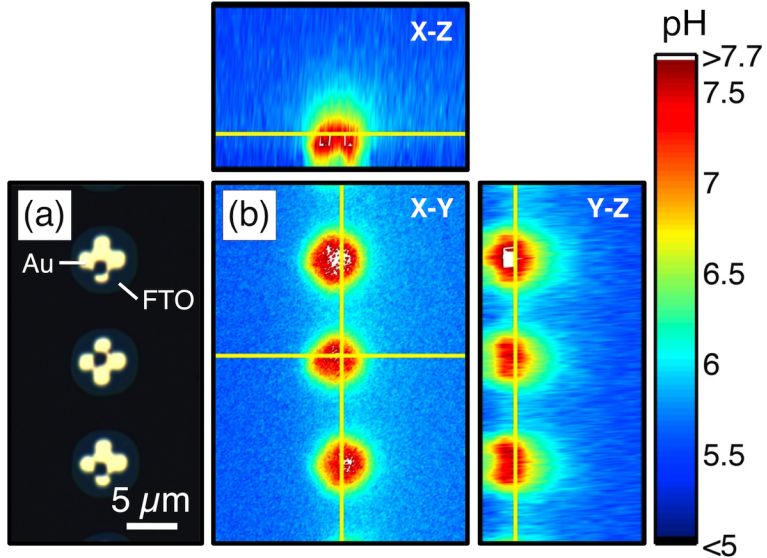


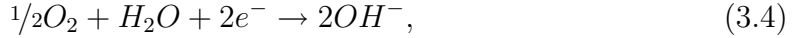
Figure 3.3 – Cloverleaf patterned Au electrocatalysts. (a) Optical microscope image of patterned Au on FTO and (b) 3D orthonormal projection image of pH with -4 μ A applied to sample and fluid flow from left to right. The scale is the same in all images, and the slice locations in the 3D image are shown as yellow lines. pH values above the detection limit are shown as white.

or the less facile water reduction reaction



depending on the local pH and ion concentrations. For near-neutral conditions as used here, the water reduction reaction is dominant. The applied flow is in the laminar flow regime, so products and reactants are swept in the positive x direction as well as diffusing in the y and z directions. In the planar geometry employed here, the pH profile in the z direction is that expected from the diffusion and fluid flow, but the easy three-dimensional imaging capability would be useful for non-planar electrodes or less uniform fluid flows. For this applied current, the flow was sufficient to overcome back-diffusion and reveal the approximate resolution of this technique to be about 5 microns determined from the size of the increased pH features in Fig. 3.3(b). The submicron features in the cloverleaf patterns are not evident primarily due to lateral diffusion. Higher applied current requires a higher flow to maintain

resolution. It should be noted that other electrochemical reactions could contribute to the measured pH increase, such as oxygen reduction,



or metal oxide reduction to metal M,



Control experiments showed that de-aerating the electrolyte by purging with Ar gas for 30 minutes showed no effect on the pH profile at a given current, indicating that oxygen reduction was not dominant. Au was chosen as a noble metal catalyst to test this technique because shows little oxidation and little oxide reduction under negative current. Additionally, a control experiment using sodium nitrate supporting electrolyte showed similar pH profiles, so the sulfate ion was unlikely involved in the pH increase.

To demonstrate the sensitivity of this technique to the local current density, a sample was prepared with Au catalyst patterned in 60- μm -square patches of hexagonally-packed circles of the same top projected area but varied radius (pitch/radius = 2.4, 62% coverage) by electron-beam lithography with the circle radius varying from 0.2 to 4 μm . The transmitted-light image and pH increase under applied flow and current is shown in Fig. 3.4 as well as a simulation of the expected pH increase calculated below. Because the indicator dye is most sensitive near its pK_a , it cannot quantitatively measure pH changes above about 1 unit above its pK_a , so any higher values are shown here as white. Since the Au circles were deposited with a finite 50 nm thickness, the sidewall area varied between patches, resulting in area-enhancement factors of at least 1.025, 1.25, 1.063, 1.5, and 1.125 from top to bottom relative to just the top projected area. When negative current was applied to the entire sample, the increased surface areas of the smaller circles is clear in the increased pH profile near those patches. The projected current density effectively increases with local surface area which is clearly

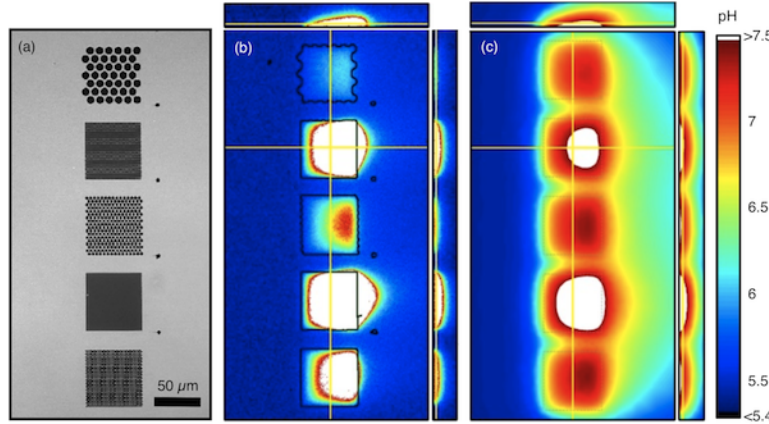


Figure 3.4 – Au circles patterned with varied surface area per patch where the circle radius of each patch from top to bottom is 4, 0.4, 1.6, 0.2, and 0.8 μm . (a) Optical transmission image, (b) 3D orthonormal projection image of pH with $-4 \mu\text{A}$ applied to sample and flow from left to right, and (c) finite element simulation of pH profile.

seen using this technique. Note that in this case the applied current and flow were chosen to clearly show the differences between the various patches rather than achieve the highest resolution, so the individual circles are not distinct in the pH image.

Fig. 3.4(c) shows a simulated three-dimensional finite-element analysis of the pH increase at a water-splitting cathode at the experimental background pH and overall current adjusted to most closely match the experimental image. The actual current density of each patch was then set by the area-enhancement factor. The simulated pH profile shows qualitative agreement with the experimental profiles though with less dependence on circle size. The e-beam lithography and liftoff process likely left rough edges and higher local Au surface area than calculated for the smallest circles. The simulation is useful to compare expected changes in pH with the measured image, and in this case reveals a bigger effect for smaller Au circles than that calculated considering only geometric differences.

The local pH increase can also indicate areas with higher catalytic activity rather than just increased surface area. To demonstrate the dependence on electrocatalyst material, a sample was prepared with islands of different metals patterned by photolithography, and connected electrically in parallel on a FTO substrate. A sample containing 80 nm each of Ag, Pt, Ni, and Au is shown in Fig. 3.5 as well as the pH in-

crease under current flow before and after an electrochemical cleaning cycle. A video of the pH profile during a cyclic voltammetry cycle is shown online in supplemental material [75]. First, the FTO shows no activity, confirming its high overpotential for water reduction. Second, the Ag initially shows a very large pH change in Fig. 3.5(b) under negative current flow which could be due to reduction of an oxide layer present after the sample fabrication and elevated temperature during photoresist bakes in air. After cycling the sample bias from -1.5 to +1.5 V and back multiple times to clean the surface, Fig. 3.5(c) shows no activity from the Ag patch because it has completely oxidized away during the cycle and become insulating. Third, the noble metals Au and Pt show an increase in activity after the cleaning cycles because surface contaminants present from sample fabrication have been oxidized away, and surface restructuring during the cycles is also a possible reason for the increase [76]. Both before and after the cycling, the Ni patch shows little pH change because its electrochemical activity is less than the other areas during this experiment, so the current tends to flow through the parallel paths that require less overpotential. The present set of metals were chosen based on their different exchange current densities and locations on either side of a ‘volcano’ plot [77], and the results seen here more or less agree with the expected trends given the surface conditions and near-neutral pH. Though the precise nature of the surface and quantitative kinetics of the various metals has not been thoroughly characterized here, the relative differences for the water reduction reaction between different materials under the same conditions are clearly seen using this technique.

The differences in local pH change in Fig. 3.5 for the different metals of identical geometric area also confirms that the reactions are not mass-transfer limited. The reactant supply and product movement away from each location is the same, yet the various locations display different behavior due to the differences in reaction rates. In this galvanostatic two-electrode experiment, the behavior reveals varied current density of different materials held at the same potential even without a reference electrode. A reference electrode would help determine the working potential but was not included here for a simpler flow cell design in the microscope.

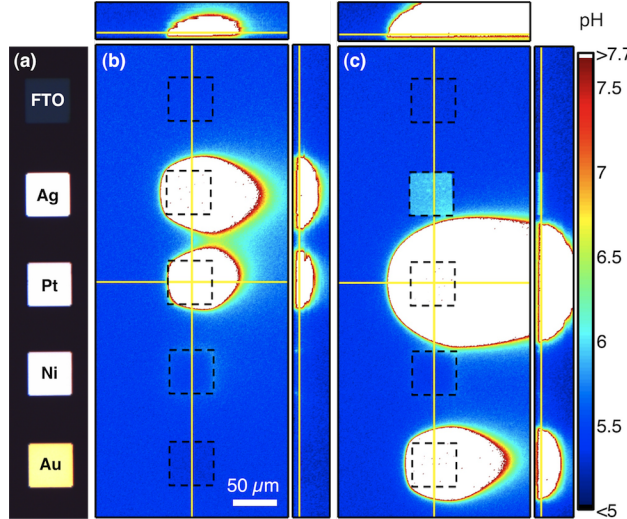


Figure 3.5 – Sample with varied metal electrocatalysts in parallel on FTO with polymer over most of the FTO. (a) Optical brightfield microscope image, showing patches from top to bottom of bare FTO, Ag, Pt, Ni, and Au, (b) 3D orthonormal projection image of pH with $-1 \mu\text{A}$ applied to sample at -1.56 V bias and flow from left to right, and (c) same conditions as in (b) but after cycling sample bias from $+1.5$ to -1.5 V ; here the sample bias was -1.50 V .

The use of a ratiometric 2-color indicator fluorophore largely eliminates variations due to laser intensity or dye concentration across the image, but care still must be taken near surface features. If the focal plane (confocal slice) is near or below the surface, spectral variations in the surface reflectivity may also change the intensity ratio which was used to calculate the pH. For example, in Fig. 3.5(c) the Ag patch has changed to a rough oxide, affecting the intensity ratio and thus indicating a slightly raised pH, but the patch did not show increased pH with increased current, so the lighter color is a slight artifact. For this reason, the x-y data is presented about 2 microns above the sample surface where the confocal slice volume barely includes the surface.

3.5 Numerical simulation of pH increase

The pH change at an electrode in a cell of arbitrary geometry and with various chemical species can be calculated by finite element techniques to solve the differential equations involved [66, 67, 78, 79]. The governing equation is the Nernst-Planck

equation:

$$\frac{\partial c}{\partial t} = \nabla \cdot [D \nabla c - uc + \mu z c \nabla \phi] + R, \quad (3.6)$$

where c is the species concentration, t (s) is time, D (m^2/s) is the diffusivity, u (m/s) is the convective flow, μ ($\text{m}^2 \text{ V}^{-1} \text{ s}^{-1}$) is the electrophoretic mobility, z is the valence, ϕ (V) is the electric potential, and R ($\text{mol m}^{-3} \text{ s}^{-1}$) is a source term accounting for reactions. The expression inside the brackets is the negative concentration flux accounting first for diffusion, second for convection, and third for electromigration. Under the assumptions of steady state conditions, isotropic diffusivity, high electrolyte conductivity so little potential drop in the electrolyte, and an incompressible fluid, this equation reduces to

$$0 = D \nabla^2 c - u \cdot \nabla c + R, \quad (3.7)$$

which can be readily modeled using finite element simulation. To model the pH change at a water-splitting cathode near neutral pH, both protons (hydronium ions) and hydroxyl ions must be taken into account as mentioned previously. The applied (negative) current will be distributed between the proton reduction or water reduction reactions depending on the pH, assuming no metal oxide or dissolved oxygen reduction. We further assume that the proton reduction reaction is limited only by the reactant supply at near-neutral pH conditions due to its generally simpler reaction mechanism. For simplicity, the fluorescent pH indicator is assumed to not participate in the electrode reactions or appreciably affect the ion concentrations during the finite element modeling; its effect as a buffer is taken into account after the proton and hydroxyl ion concentrations are calculated. The overall current density is then related to the ion fluxes,

$$\frac{I}{AF} = J_{H^+} - J_{OH^-}, \quad (3.8)$$

where I is the applied current, A is the electrode area, F is Faraday's constant and the species fluxes J_{H^+} and J_{OH^-} are in $\text{mol m}^{-2} \text{ s}^{-1}$. At near-neutral pH, most of the current will be carried by the hydroxyl ion flux and likely reflect the kinetics of the water reduction reaction rather than the proton reduction reaction. The dissociation

of water is much faster than diffusion, so local equilibrium will hold for the water dissociation reaction Eq.[3] which has forward and backward rate constants $k_{w,f}$ and $k_{w,b}$ and equilibrium constant $K_W = k_{w,f}/k_{w,b} = 10^{-14}$ in excess pure water. Correcting for 200 mM ionic strength, $K_W = 10^{-13.73}$. It is easiest to implement this local equilibrium in COMSOL as a reaction for both species with rate

$$R_{H^+} = R_{OH^-} = (k_{wf} - k_{wb}[H^+][OH^-]), \quad (3.9)$$

using $k_{w,f} = 10^{-6.865}$. The above equations are solved in COMSOL using the Transport of Diluted Species module including convection and diffusion for both protons and hydroxyl ions coupled to the Laminar Flow module to simulate the fluid flow with a no-slip boundary condition along the flow cell walls. The flow cell was modeled in three dimensions over a channel length, width, and height of 1.8, 1.5, and 0.7 mm, respectively, with the electrocatalyst patches on the bottom of the channel. The ion concentrations in the bulk and on the inlet boundary were set by the initial pH of the electrolyte. At the electrocatalyst patches, the proton concentration was set to 10^{-11} mol/m⁻³ which is approximately zero, representing the facile proton reduction. Based on that boundary condition, the current due to proton reduction at the electrocatalyst patches was subtracted from the applied current, and the remainder of the current was set as an incoming flux of hydroxyl ions. The ionization of water was set as a bulk reaction term for both ions. The diffusivity of protons and hydroxyl ions was set to 9.30×10^{-5} and 4.62×10^{-5} cm²/s, respectively (14). Following the COMSOL simulation, the resulting profiles of proton and hydroxyl ion concentrations were imported in Matlab to calculate the buffering action of the BCECF indicator dye. At each spatial location, we treat the simulated proton concentration as a concentration of strong acid of concentration [A] and the hydroxyl ions as a strong base of concentration [B]. Treating the fluorophore as a weak acid with $pK_F = 7$ and concentration [F], the charge and mass balance result in the equation for [H+],

$$[A] + \frac{[F]}{[H^+] + K_F} + \frac{K_W}{[H^+]} = [B] + [H^+], \quad (3.10)$$

which has one positive root used to calculate the solution pH as shown in Fig. 3.4(c), where qualitative agreement is seen with the experimental results. The described approach is very similar to previous calculations of pH involving weak fluorophore buffers [66, 68], with possible slight differences in the treatment of the acid-base equilibria of both water molecules and the fluorophore. The simulation could be used to calculate the quantitative local current density at a clear surface feature by varying simulated current until the pH profile matches the experiment. The volume and area of an iso-pH surface would make a simple fitness function as long as the fluid flow and fluorophore concentration were carefully controlled in the experiment. However, the patterned catalyst islands of interest must be sufficiently removed from other catalysts so that the diffusion profiles do not overlap in steady state.

3.6 Conclusions

We have demonstrated the use of pH-sensing fluorophores to quantitatively image pH gradients resulting from reductive currents in aqueous electrochemical cells. Confocal laser-scanning microscopy was utilized for good signal-to-noise and 3D imaging capabilities. Micron-scale information is possible with the use of a flow cell to overcome diffusion, a resolution which approaches that of scanning probe electrochemical techniques while minimally perturbing the electrochemical conditions. The pH profiles were shown to sensitively respond to variations in both electrocatalyst surface area and inherent catalytic activity. In such an experiment, the area on a substrate with the highest catalytic activity was immediately obvious from the fluorescence profile. This technique could be expanded for use in combinatorial catalyst discovery, where a single substrate was patterned with electrocatalysts with varied composition or growth conditions. In a flow cell, however, the flow should be uniform over the field of view, and pH changes at one spot on the electrode may affect the downstream profiles. Time-resolved images or alternating voltage could also provide good resolution without the use of a flow cell. The images presented here were taken in steady state, but the fast laser scanning allows image acquisition in less than a second. Photo-

toelectrodes could be analyzed by switching the illumination sources analogous to a photobleaching experiment, where snapshots of the pH profile are taken after broad illumination of the sample. The primary limitation of this technique lies in the narrow pH range that is accessible, but other fluorophores could be used with different pK_a values. For example, Oregon Green is another fluorescein derivative with a pK_a of 3-4 where hydrogen-evolution catalysts are typically more active [80]. Alternatively, for the oxygen-evolution reaction, a fluorophore that shows increased fluorescence with decreased pH is quinine [63, 65], or many dyes are quenched in the presence of dissolved oxygen [81]. The added dyes also should interact minimally with the surface to avoid changes in surface chemistry. Due to both diffusion limitations and the diffraction limit of visible light, it is unlikely that the resolution of this technique could be extended below a micron as implemented here. However, some interesting extensions could be done using super-resolution microscopy in which isolated dye molecule fluorescence events are analyzed to achieve subwavelength resolution.

Chapter 4

Photoelectrode minority carrier diffusion length measured via wedge geometry

While imaging the water splitting reaction rate is important for the chemical reaction and catalysis aspect of photoelectrochemical cells, the semiconductor light absorber lies at the heart of the device, and an important piece of a tandem solar fuel generator is missing at present—a stable photoanode with a bandgap around 1.7 eV. As the Joint Center for Artificial Photosynthesis searches with high-throughput methods for such a material, in-depth yet rapid techniques are needed to measure the semiconductor parameters of the multicomponent metal oxides, sulfides, and nitrides likely to be found. One important material parameter is the minority carrier diffusion length, and after a search considering a few different techniques, the measurement method presented in this chapter was developed to provide an independent determination of the diffusion length on an arbitrary semiconductor material.

4.1 Introduction

Efficient energy conversion from light to electrical energy can be accomplished either by thermal processes in which a macroscopic body is heated by the absorbed photons or by quantum processes in which each photon excites an electron-hole pair whose energy is directly utilized in the device. The thermal energy-conversion effi-

ciency increases with increasing temperature differences in the heat engine used to extract work, and the upper limit is given by the Carnot efficiency. From a practical standpoint, it is often desirable to avoid high temperatures, and so quantum energy-conversion processes such as photosynthesis and the photovoltaic effect are attractive. In this case, excited electrons must be physically separated from the corresponding hole before recombination within a characteristic lifetime. Semiconductor materials offer a good balance of light absorption and electron lifetime, and thus efficient energy conversion is possible by inducing charge separation at junctions in semiconductor photovoltaic and photoelectrochemical devices.

The excited charge-carrier lifetime depends on many properties of the bulk material such as the underlying band structure, the defect density, and the presence and electronic properties of surfaces. Unfortunately the carrier lifetime often strongly decreases with increased impurity concentration, therefore highly pure semiconductors, which increase cost, are required for efficient photovoltaic devices. Rather than just discuss carrier lifetime, a more relevant parameter for device construction is the diffusion length,

$$L = \sqrt{D\tau}, \quad (4.1)$$

where L is the diffusion length, D is the carrier diffusivity, and τ is the carrier lifetime. The diffusion length represents the average distance travelled by an excited charge carrier or exciton in the absence of electric fields before recombination, and it determines the allowable characteristic dimensions of the device's active absorbing layer. For light incident on a bulk slab of semiconductor material, the carrier generation rate G is obtained by differentiating Beer's law of exponential absorption,

$$G(x) = \alpha\Phi(1 - R)e^{-\alpha x}, \quad (4.2)$$

where x is the distance into the semiconductor, α is the absorption coefficient, Φ is the incident photon flux, and R is the reflection coefficient. From equation 4.2, the other characteristic dimension relevant to the device performance is the absorption length $1/\alpha$. For best device efficiency, the diffusion length should be long enough

that $L\alpha > 1$. Most semiconductor devices consist of doped materials where it is the photogenerated minority carriers that must reach an interface to be collected and captured as electrical or chemical energy, so the important material characteristic is the *minority carrier diffusion length*.

In the search for new semiconductor materials that meet all the requirements for photoelectrochemical water splitting, it is important to know the minority carrier diffusion length in addition to other device or material properties such as the bandgap energy, spectral absorbance, illuminated open circuit voltage, and band edge energetic positions. Though the minority carrier lifetime can also be measured, the minority carrier diffusivity/mobility is usually unknown, and a direct measure of diffusion length is more directly useful and applicable to the device design. In particular for n-type photoanodes, the minority carriers are holes with a diffusion length L_p , but equivalently the technique could be applied to p-type photocathodes to evaluate L_n . This chapter will discuss the development of an alternative, independent technique to quickly assess L_p by scanning strongly absorbed illumination along a photoanode with a gradient in absorber-layer thickness.

4.1.1 Theory and choice of wedge geometry

To understand the minority carrier diffusion length, it is useful to consider the spatial distribution of generation and collection of minority carriers in a n-type one-dimensional generic device. The device model assumes abrupt, full depletion of minority holes at a depletion-width boundary at a distance W_d from a barrier-type contact, a back contact with an arbitrary recombination velocity, low-level injection with bulk lifetime τ , and simple exponential light absorption with each absorbed photon generating one electron-hole pair. The geometry used to set up the following model is shown in Figure 4.1 where light is incident on the left side of a semiconductor slab at $x = 0$ through a transparent contact (Contact 1) and any light that is not absorbed escapes through Contact 2 on the right side. Photogenerated charge carriers are lost either by bulk recombination or by collection at either boundary with

a collection (or recombination) velocity s , and the solution to the diffusion equation for excess minority holes is given generally by [82]

$$\Delta p(x) = Ae^{-x/L_p} + Be^{x/L_p} + Ce^{-\alpha x}, \quad (4.3)$$

where the coefficients are given by

$$\begin{aligned} A &= C \left(\frac{(S_2 - \alpha L_p)(1 - S_1)e^{-\alpha W} + (S_1 + \alpha L_p)(1 + S_2)e^{W/L_p}}{(1 - S_1)(1 - S_2)e^{-W/L_p} - (1 + S_1)(1 + S_2)e^{W/L_p}} \right), \\ B &= C \left(\frac{(S_2 - \alpha L_p)(1 + S_1)e^{-\alpha W} + (S_1 + \alpha L_p)(1 - S_2)e^{-W/L_p}}{(1 - S_1)(1 - S_2)e^{-W/L_p} - (1 + S_1)(1 + S_2)e^{W/L_p}} \right), \\ C &= \frac{(1 - R)\Phi\tau\alpha}{1 - \alpha^2 L_p^2}, \end{aligned}$$

and dimensionless boundary collection/recombination velocities are defined as $S = sL_p/D$ which are evaluated at the edges of the quasi-neutral region of width W . If the junction is on the left side of the device, assumed full minority carrier sweep-out implies $S_1 \rightarrow \infty$, whereas if the junction is on the right side, $S_2 \rightarrow \infty$. The photocurrent density resulting from full collection by drift in the depletion region as well as partial diffusion collection by considering the continuity equation for carriers that diffuse to the depletion region boundary is then

$$J_{photo} = J_{drift} + J_{diffusion} \quad (4.4)$$

$$|J_{photo}/e_c| = \int_{DR} G(x)dx + D \frac{d\Delta p}{dx} \Big|_{W_d}, \quad (4.5)$$

where DR denotes the depletion region and e_c is the charge on an electron. To fairly evaluate various techniques for diffusion length extraction with the fewest assumptions, eqn. 4.5 was implemented in Mathematica as described in Appendix B and plotted with various conditions. A few results of interest will be discussed below.

The traditional technique used to measure the diffusion length utilizes the spectral response, where the absorption length is varied with front-illumination of the junction as is the case in Figure 4.1. In this configuration a barrier is created near the front,



Figure 4.1 – Geometry for diffusion length calculations with both the junction and illumination shown on the left side as for spectral response. For the wedge geometry, the junction is on the right side instead.

ideally with a short depletion width, and the sample thickness must be a few times greater than the absorption length. Under the assumptions $W \geq 4L_p$, $W_d \ll L_p$, $W_d \ll 1/\alpha$, and $W \gg 1/\alpha$, eqn. 4.3 at the depletion region boundary reduces to

$$\Delta p(W_d) \approx \frac{(1-R)\Phi\tau}{(1+S_1)} \frac{1}{(1/\alpha + L_p)} \quad (4.6)$$

or

$$\left. \frac{d\Delta p}{dx} \right|_{W_d} \stackrel{S_1 \rightarrow \infty}{\approx} (1-R)\Phi\tau L_p \frac{1}{(1/\alpha + L_p)}. \quad (4.7)$$

Thus the spectral response measured as either a function of surface photovoltage $V_{SPV} \approx (kT/p_{no}e_c) \Delta p(W_d)$ [83] or photocurrent $J_{photo} \approx e_c D (d\Delta p/dx)|_{W_d}$ can reveal the diffusion length. Typically the inverse of the spectral response is plotted as a function of the absorption length where the photon flux is held constant or at least known, and the diffusion length is given by the intercept on the horizontal axis as seen in Figure 4.2. This technique is sometimes called the G  rtner analysis [84]. With this technique it is important that the diffusion length be less than the sample thickness, or the technique will instead indicate an effective diffusion length of less than half the sample thickness. Perhaps of greater concern is the depletion layer thickness which is not necessarily much smaller than the absorption or diffusion length, and a thick depletion layer will return an artificially high effective diffusion length (slightly less than the depletion width) which is not immediately obvious in the measurement. On the other hand, recombination at the back surface is not a strong effect. One practical difficulty with this measurement is the necessity of accurate knowledge of the

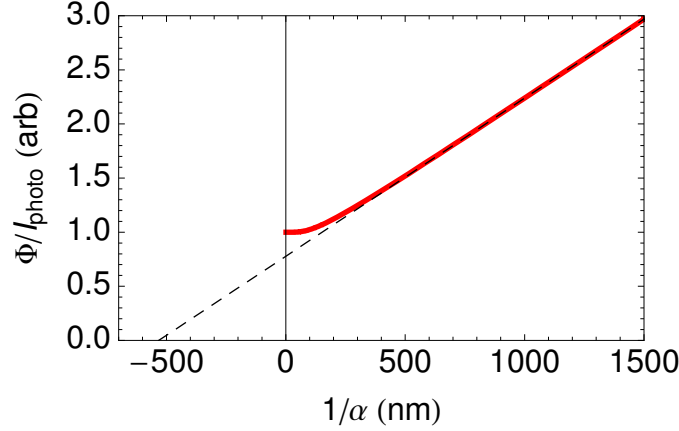


Figure 4.2 – Simulated spectral response measurement of diffusion length. The x-intercept of the extrapolated line gives the diffusion length.

spectral absorbance for wavelengths where the absorption length is much smaller than the measured sample's thickness. The spectral response measurement of diffusion length is highly dependent on the measurement of the absorbance, whereas the wedge technique developed here does not require extensive characterization of the absorption coefficient for multiple wavelengths.

A second common technique to measure diffusion length is electron-beam or optical-beam induced current (EBIC or OBIC). In this case a localized solid-state junction is formed and electron-hole pairs are locally excited at varying distance from the junction using a focused electron or optical beam; the resulting current exponentially decays away from the junction. For this technique, the surface recombination away from the junction can strongly affect the measured current, and fabrication of a solid-state junction is required. One might expect a higher resolution excitation from a sub-nm focused electron beam, but the generation volume within the solid can still have dimensions of a few hundred nanometers for a 10 kV beam.

An alternative method explored here to measure the minority carrier diffusion length holds the absorption depth constant with single-wavelength back illumination while the sample width is varied in a wedge geometry. The general expectation is that for strongly absorbed light, holes will be generated near the back of the sample and must diffuse to the front junction to be collected as photocurrent, so an exponential decrease of photocurrent with increasing sample thickness should be seen. In this case,

the junction is defined by Contact 2 in Figure 4.1 so $S_2 \rightarrow \infty$ and the depletion width is measured from the right side. A calculated plot of the photocurrent as a function of thickness is shown in Figure 4.3. Under the assumptions $W \geq 4L_p$, $L_p \gg 1/\alpha$, and $W \gg 1/\alpha$, the photocurrent due to diffusion evaluated at $x = W$ reduces to

$$J_{photo} \approx \frac{2(1-R)\Phi(1+S_1/\alpha L_p)}{(1+S_1)} e^{-W/L_p}, \quad (4.8)$$

so the diffusion length is easily extracted by the slope of a plot of $\ln[J_{photo}]$ as a function of quasineutral (or sample) thickness W . Here the requirements are only strongly absorbed light and a thick enough quasineutral region; back-contact surface recombination has a small effect. Additionally, the prefactors in eqn. 4.8 should not depend on sample thickness, so the absolute value of the light entering the sample or back-surface carrier recombination does not affect the measurement as long as a photocurrent is measurable. The absorption coefficient need only be known at the excitation wavelength, and it places a lower limit on the measurable diffusion length. On the other hand, the photocurrent expression in the weakly absorbed limit where $W \ll 1/\alpha$,

$$J_{photo} = \frac{(1-R)\Phi\tau\alpha}{(1+\alpha L_p)L_p} e^{-\alpha W}, \quad (4.9)$$

and the effective measured diffusion length from the graphed slope would actually be the absorption length.

Though fabricating a sample with varied thickness can require nontraditional processing, extracting the diffusion length from a wedge geometry should require less detailed measurements and fewer assumptions about the material under study than the spectral response or EBIC techniques for new semiconductor materials. Previously this technique has been applied to diffused solid-state homojunctions and called the “angle-lapped junction” method [82], but the ability to create a solid-state junction is not straightforward for new materials. However, liquid junctions can be formed quickly and allow junctions to be formed on a wide variety of materials through the many choices of redox couples and aqueous or nonaqueous electrolytes. We chose to further develop this technique for screening minority carrier diffusion lengths and

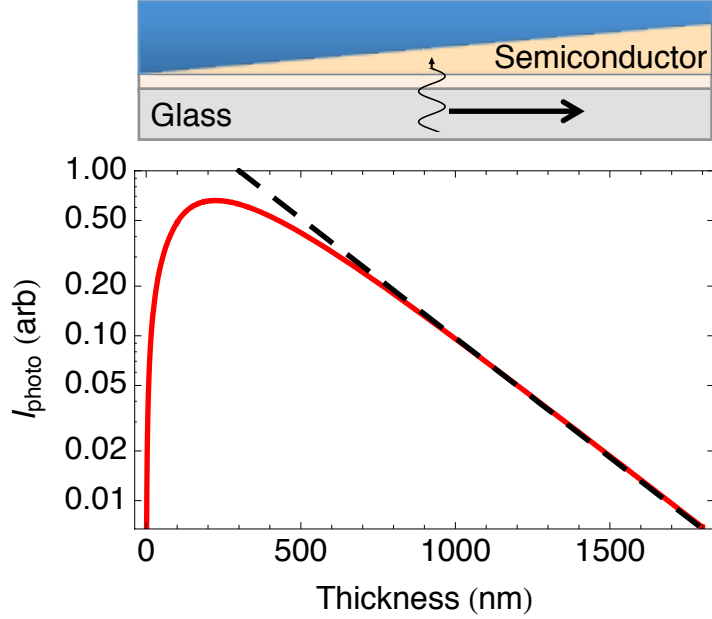


Figure 4.3 – Wedge geometry for diffusion length measurement. The photocurrent for back illumination is plotted as a function of thickness. In this example the absorption length is 150 nm, the diffusion length is 300 nm, the depletion width is 100 nm, and the back-surface recombination is assumed to be low. The diffusion length is simply extracted from the slope of the line toward the thick side.

demonstrate it using a solid-state silicon wedge and a liquid junction with a graded-thickness tungsten oxide photoanode film.

4.1.2 Assumptions and requirements

The above mathematical treatment is accurate for numerical calculations, but it is somewhat unclear to discern the range of parameters over which the limiting case of exponential decay of photocurrent with thickness applies. Several different cases are plotted below in Figure 4.4 where the x-axis is a dimensionless thickness so that the exponential decay of eqn. 4.8 is evident as a slope of -1. A basic test case is shown as the black solid line where the photocurrent first increases with thickness due to increased light absorption and full collection within the depletion width, then after the sample becomes thicker than the depletion width, the photocurrent begins to exponentially decay due to carrier diffusion limitations. The effective diffusion length is given by the line slope which is plotted in the right side of Figure 4.4. For the base

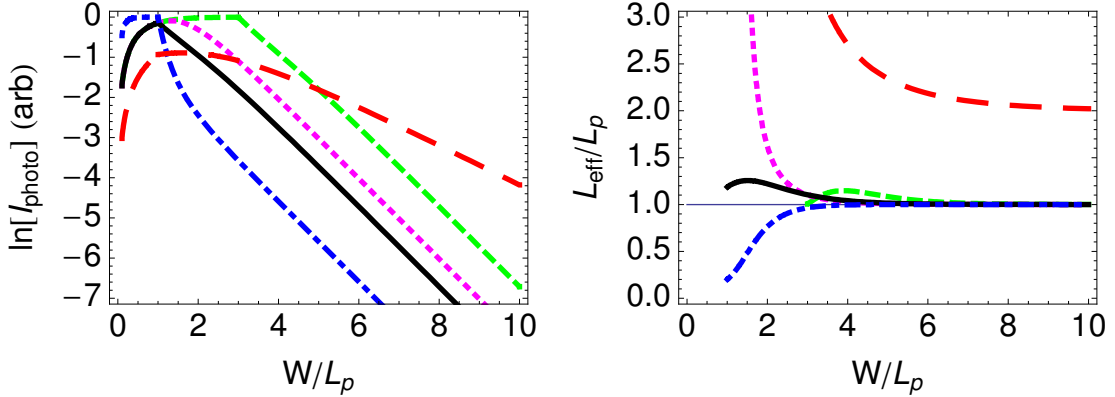


Figure 4.4 – Calculated photocurrent (left) and corresponding effective diffusion length from the local slope (right) as a function of number of diffusion lengths of film thickness. Black solid line: base case where $L_p = 2/\alpha$, $W_d = L_p$, and high back-contact surface recombination. Purple dotted: low back-contact surface recombination. Green dashed: $W_d = 3L_p$. Blue dash-dotted: $L_p = 10/\alpha$. Red coarsely dashed: $L_p = 0.5/\alpha$.

case, the effective diffusion length becomes the true diffusion length when the film thickness is 3-4× the true diffusion length.

The other lines in Figure 4.4 show the effect of varying other parameters in the material and geometry. While the base case assumed high carrier recombination at the back (ohmic) contact, the profile for low back-contact recombination is shown as the dotted purple line. Low recombination increases the photocurrent due to the ability of minority carriers to reflect off the back contact but does not appreciably change the overall shape. If the depletion width is wider than the diffusion length, the initial increase of photocurrent with thickness will be in effect until larger thicknesses are reached, as seen in the green dashed line. Essentially, the depletion width on the front of the sample just thins the quasineutral region width, but it does not change the exponentially decaying behavior once the sample is thicker than the depletion width, since illumination is from the back. The case of longer diffusion length compared to the absorption length is shown as the blue dash-dotted line; here high back-contact surface recombination has a stronger effect because the effectively shorter absorption length means carriers are generated closer to the back surface. Finally, the important case of diffusion length shorter than the absorption length is shown as the red coarsely-

dashed line, and it is clear that the effective diffusion length never approaches the true diffusion length. This reflects the limiting case in eqn. 4.9 where the absorption length is longer than the diffusion length. Even though the photocurrent vs. thickness curve may show an exponential decay, the value extracted will be the absorption length rather than the diffusion length. However, this lower limit on measurable diffusion length can be determined by a simple optical transmission measurement on a film of appropriate thickness at the wavelength used for measurement.

The initial portion of the photocurrent vs. thickness curve can show various behaviors depending on the depletion region width, back-contact surface recombination, and absorption length. Thus, it is difficult to extract quantitative information from the initial rise in photocurrent with thickness. Similarly, it is tempting to propose a similar experiment with front illumination on a wedge expecting that the photocurrent should reach a maximum when the thickness is equal to the diffusion length, but no such simple interpretation was found in numerical simulations. It should be noted that these calculations were done assuming a constant thickness for the illuminated area requiring a small illumination spot. Any change in thickness over a relatively large illuminated area will smear out the photocurrent vs. thickness curve but should not have a strong effect in the exponentially decaying regime if the thickness change is approximately linear.

Though porosity and nanostructuring can be a critical part of efficient electrode design for photoelectrochemical devices, any deviations from a dense, approximately planar film are a problem for electrochemical diffusion length measurements. Porosity in the film causes the 1D approximation to break down because photogenerated carriers can be collected by electrolyte that has filled in any cracks or connected pores, so the effective film thickness for collection is not the true film thickness. The simple 1D model can be modified by replacing the film thickness with an effective film thickness given by

$$W_{eff} = W_{film} \sin \left[\arctan \left(\frac{W_{grain}/2}{W_{film}} \right) \right] \quad (4.10)$$

where the geometry under consideration is shown in Figure 4.5. In the limit that

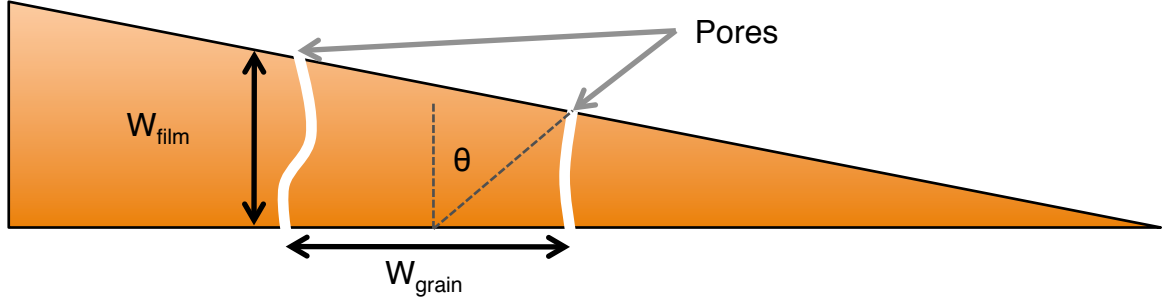


Figure 4.5 – Pore geometry considered to motivate eqn. 4.10.

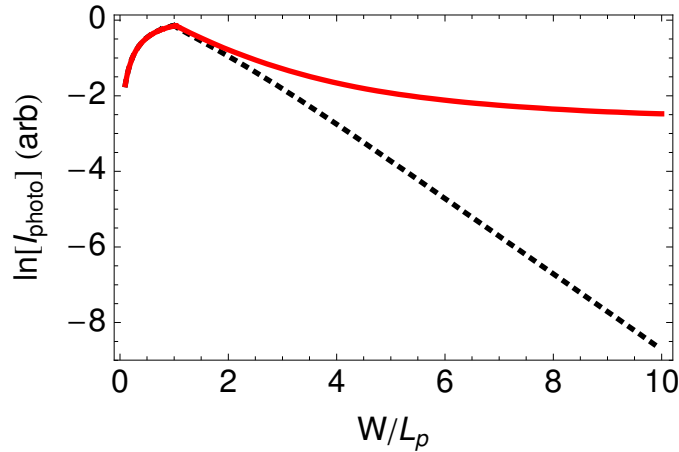


Figure 4.6 – Photocurrent behavior with pores. The black dotted line shows the base case (from Fig. 4.4) without pores and the red solid line is calculated with grains of width $W_{grain} = L_p/25$.

$W_{grain} \rightarrow 0$, $W_{eff} \rightarrow 0$, while in the limit that $W_{grain} \rightarrow \infty$, $W_{eff} \rightarrow W_{film}$. Though this is a very crude correction to the 1D model, it reasonably reproduces the behavior expected when 3D collection is active. Then the photocurrent will tend to become constant as a function of apparent film thickness as shown in Figure 4.6 where a correction is made to the dotted-line base case without pores.

As described by the mathematical analysis and graphical examples, the following requirements apply to the back-illuminated wedge technique for diffusion length measurement:

1. $3L_p < W < 10L_p$. The film thickness must be in the exponentially decaying carrier-diffusion-limited regime but not so thick that the photocurrent is unmeasurable.

2. $1/\alpha < L_p$. The absorption length sets a lower limit on measurable diffusion length. However, a measured diffusion length longer than the absorption length should be reliable.
3. Dense films and one-dimensional transport.

The presence of grain boundaries can also affect minority carrier lifetimes, so in many cases the measured effective diffusion length may not represent the true bulk diffusion length. However, the measured value still truly represents the distance a minority carrier can travel on average in a given material, so perhaps a better term would be the “minority carrier collection length.” However, the phrase “diffusion length” can still be applied if it is recognized that in a highly polycrystalline film with small grains the measured value is not necessarily the true bulk minority carrier diffusion length.

4.2 Fabrication of materials in the wedge geometry

The back-illuminated wedge technique does not necessarily require a wedge but rather just a well-controlled variation in thickness across a single sample or multiple samples. However, to reduce the uncertainty resulting from sample-to-sample variation, true wedges were made and measured for demonstration. The fabrication and material characterization of both silicon and tungsten oxide wedges is discussed here, and the scanned photocurrent results will be discussed in Section 4.3.

4.2.1 Polishing silicon into a wedge

To first test the wedge technique, a silicon wafer was chosen for its well-established properties and preparation techniques. A prime-grade 530- μm -thick (100) n-type wafer of resistivity $0.11 \Omega\text{-cm}$ measured with a four-point probe was chosen because its doping level of $5.3 \times 10^{16} \text{ cm}^{-3}$ corresponds to an easily measurable diffusion length of 100-200 μm [85]. A $1 \times 2 \text{ cm}^2$ piece of the wafer was made into a wedge by first carefully mounting it flat on a South Bay Technology Model 590 tripod polisher and adjusting the rear micrometers to create a slight angle. Polishing was done with

successively finer diamond lapping films from 30 μm down to 1 μm grit size on an 8 inch polishing wheel.

After polishing, the sample was briefly dipped in HF, and a Pt Schottky contact was deposited over most of the flat side by electron-beam evaporation. The bulk Si wafer was ohmically contacted with In/Ga eutectic and silver paint, while the top Pt was contacted with a spring-loaded wire. The Pt/Si junction showed diode-type behavior, albeit a leaky one, with ideality factor 3-4. The quality of the diode was nonetheless sufficient to collect photogenerated minority carriers at short circuit.

4.2.2 Sputtering WO_3 under a shutter

As the objective for developing this technique is to screen semiconductor photoelectrodes for water splitting, the oxide semiconductor tungsten trioxide was chosen as a model photoanode material [86]. It can be fabricated via wet chemical techniques [87, 88], electrodeposition [89], and vacuum physical-vapor deposition [90, 91]. For photoelectrodes that can be made by physical-vapor deposition, the substrate can be moved during deposition to create a thickness gradient. However, for sputtering, an even simpler way to make a wedge is by placing a shutter partway over the substrate during deposition. The large source size, mTorr chamber pressures, and slight source angle in the AJA sputter-deposition system used mean that the deposition profile is not highly line-of-sight (as in evaporation), and a clear thickness gradient develops in the deposited film over the scale of mm to cm, depending on the distance of the partial shutter above the substrate. We used a shutter fixed at about 1 cm above the samples which gave rise to a thickness gradient over about 2 cm on the samples as seen in Figure 4.7. Substrates were either VWR microscope slides for optical characterization, out-of-the-box silicon wafer pieces for thickness profiles, or cleaned F: SnO_2 -coated glass (Pilkington TEC15) for electrochemical measurements. Tungsten trioxide films were deposited by reactive RF magnetron sputtering from a 2-inch-diameter tungsten target at 200 W with 20-25% O_2 in Ar at 6-10 mTorr, and the substrate temperature was varied from 180-400 °C. These conditions allowed

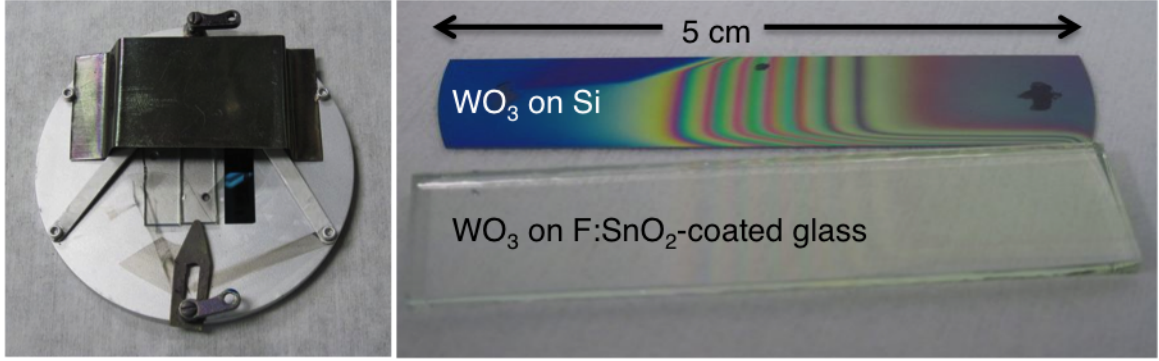


Figure 4.7 – Sputter deposition setup for thin-film wedge fabrication. A 1-cm-tall shutter is halfway over samples (left), and resulting optical fringes are seen from film thickness gradient (right).

a film growth rate of roughly 500 nm/hour. The targeted maximum film thickness ranged from 1.5 to 4 microns.

To characterize the gradient in thickness, the film that was simultaneously deposited on the Si wafer was imaged in an optical microscope. The Si wafer provided a clear view of the optical reflectance fringes so that a reflectance image with 500 nm illumination allowed determination of the film thickness profile as shown in Figure 4.8. An ellipsometry measurement for a known thickness WO_3 film was used to determine that the index at 500 nm was 2.34, so each maximum in the interference fringe profile corresponded to a thickness increase of $\lambda/(2n) = 107 \text{ nm}$. The thickness profile referenced to an end or to a scratch on the middle of the sample then could be easily measured and fitted to a sigmoidal function. Additionally, the films deposited on FTO were often cleaved at the thick side to image the cross-sectional film morphology in a scanning electron microscope (SEM), and the maximum thickness could be verified or used to adjust the optical data. The films grown on FTO could also be used to image the thickness fringes, but the lower index contrast at the substrate as well as the underlying FTO roughness gave less interference contrast.

Varying the sputtering temperature or oxygen partial pressure during deposition causes different film morphologies and differences in photoelectrochemical response [90, 91]. While initial films were deposited at higher temperatures of 400-500 °C, the nonideal photocurrent vs. thickness behavior due to porosity motivated deposition

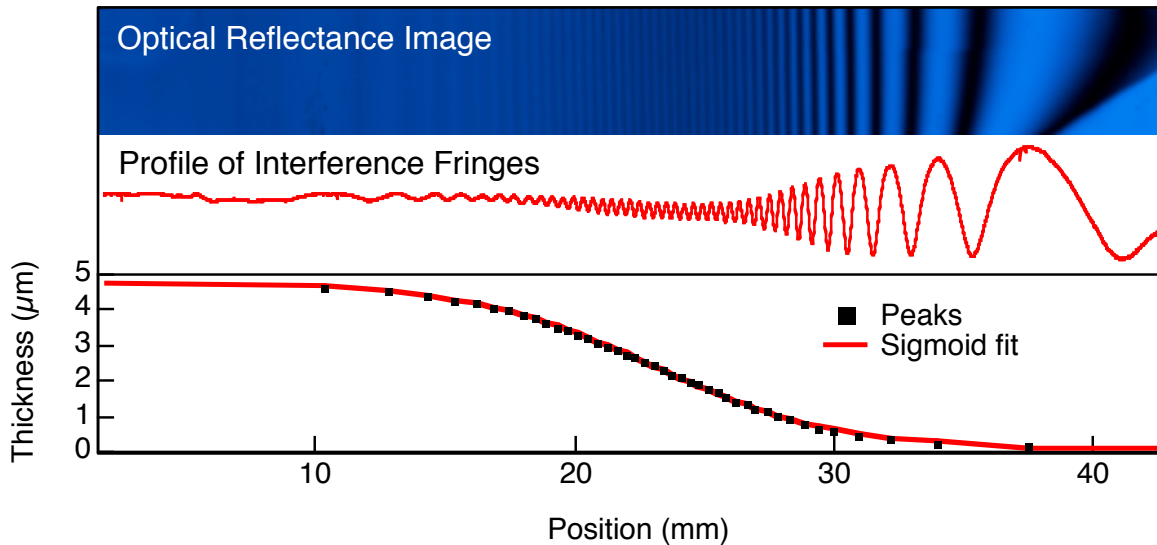


Figure 4.8 – Optical determination of sputtered film thickness profile. (Top) The image of reflection of 500 nm light; (middle) a line profile of the reflection fringes; (bottom) spatial thickness profile determined from the position of each fringe maximum.

at lower temperatures down to 200 °C to obtain a more compact film morphology. Some representative SEM images of the film microstructure are shown in Figure 4.9 at varied temperatures, and it is clear that the lower temperature depositions consisted of a denser film with fewer voids between crystallites and perhaps smaller grain sizes. A cross section of a cleaved sample with high-temperature deposition shows the glass substrate on the left, the FTO nucleation layer and film, and finally the thick WO₃ film revealing columnar growth which is common for sputter deposition. The lower-temperature growths also showed similar columnar cross sections but with denser packing and a smoother top surface.

With the variation in processing conditions, the crystal structure was measured by x-ray diffraction (XRD) to verify the phase. The films all deposited as polycrystalline with XRD patterns consistent with the monoclinic phase of WO₃ for films deposited from 200-500 °C as seen in Figure 4.10. However, the highly oriented nature of the film growth and similarity to other phases made it difficult to definitely identify the phase, and the orthorhombic or sub-stoichiometric (WO_{2.9}) phases seen in previous work [90] could not be ruled out. Some initial samples were also deposited amorphous at lower temperature then annealed in air and crystallized at 400 °C, but the thermal

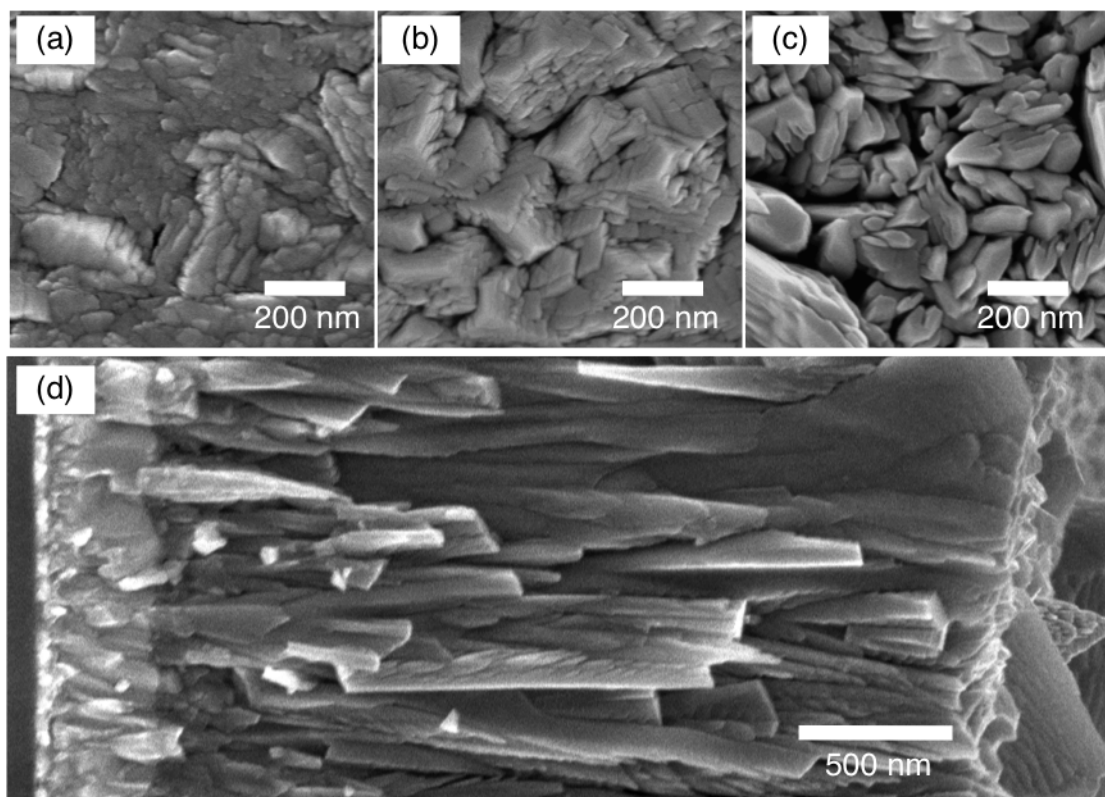


Figure 4.9 – Top surface morphology SEM images of WO₃ deposited at (a) 200 °C, (b) 300 °C, and (c) 400 °C on FTO. The cross section is shown in (d) for the film grown at 400 °C, and the lighter layer to the left is the FTO.

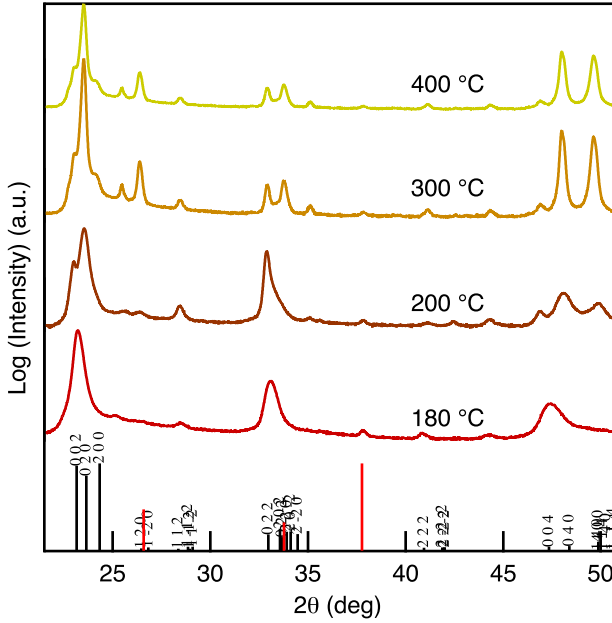


Figure 4.10 – XRD of WO₃ deposited at various temperatures. The peaks for monoclinic WO₃ (black labeled) and the substrate SnO₂ (red unlabeled) are also shown.

stresses or phase transition during this processing caused the films to crack and cause voids in the film that violated the requirement of a dense film with 1D transport.

After sputtering, the tungsten oxide was often found to be too porous to get good electrochemical data. The wedge technique (as well as most diffusion length measurement techniques) requires that carrier collection be one-dimensional, and the presence of pores changes the apparent film thickness with a liquid contact as discussed in Section 4.1.2. Our films were apparently nanoporous, as has been reported for similarly deposited films [91]. To insulate any electrochemically active pores or grain sidewalls, we chose to coat the entire sample surface with a 10 nm layer of aluminum oxide deposited by atomic layer deposition (ALD). A long cycle time was used to allow the precursors to fully infill the structure. After the ALD treatment, the surfaces showed an identical morphology by SEM to Figure 4.9 but with perhaps more charging from the insulating surface. The ALD-treated samples showed no electrochemical activity or photocurrent, verifying that the alumina was largely conformal and insulating as desired. To expose the top surface, the samples were mounted on the tripod polisher and carefully leveled using a flat glass plate and minimizing the number of Newton's

rings visible between the plate and the sample. Gentle polishing was then done using 50 nm colloidal diamond slurry (Buehler MetaDi Supreme 0.05um) on a porous polyurethane pad (Eminess Politex Reg) for 10-30 minutes on a polishing wheel at about 50 rpm. The best results and uniformity were obtained when the sample was rotated once or twice during polishing. The effect of the polishing on the top film morphology is shown in Figure 4.11. For short polishing times, only the tops of the largest and highest-protruding grains were polished off, evident in the low SEM contrast and flat profile in an atomic-force microscope (AFM) scan. With a bit longer polish, most of the top grains were polished smooth as seen in Figure 4.11(c). As the sample was polished even longer, it became extremely flat and difficult to image in the SEM. One sample was also gently sputtered away using the RF substrate bias in the AJA sputtering system; this revealed the pores that had been insulated by aluminum oxide because the tungsten oxide was more readily sputtered, leaving behind the aluminum oxide that had been coating the sidewalls as protrusions. The ALD insulation was also attempted on the annealed samples with cracks, but the photocurrent results showed less success than on the high-temperature-deposited samples.

The spectral absorbance was measured via optical transmission and reflection for films deposited on the glass substrate. The raw and processed data for a 880-nm-thick film deposited at 300 °C is shown in Figure 4.12. In the strongly absorbing regime, the transmitted light intensity T for a freestanding thin film is [92]

$$T \approx (1 - R)^2 e^{-\alpha W_{film}}, \quad (4.11)$$

where R is the reflection from the air/dielectric interface which is approximately equal to the measured reflectance. The absorption coefficient can then be calculated as

$$\alpha = \frac{\ln[T/(1 - R)^2]}{W_{film}} \quad (4.12)$$

if the film is absorbing strongly enough to neglect Fabry-Perot interference effects. Here the transmission value used should be corrected for the transmission of the sub-

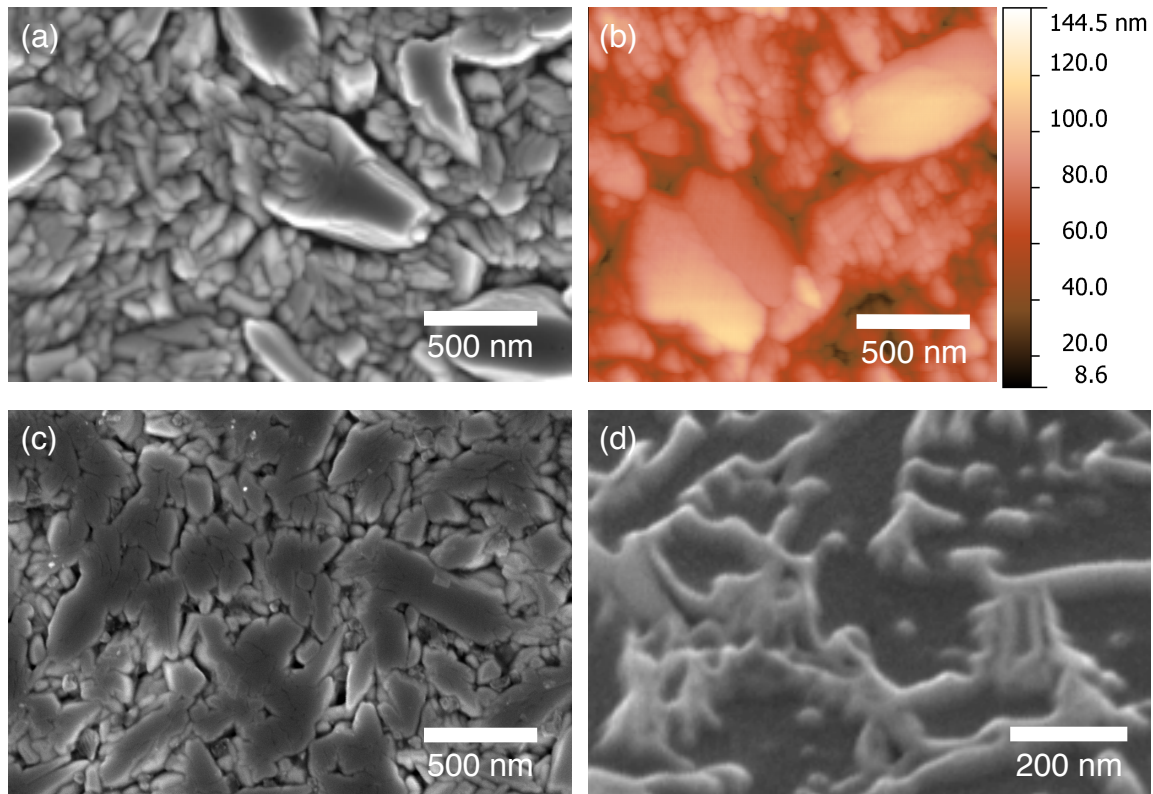


Figure 4.11 – Top surface morphology of polished WO_3 . (a) and (b) are SEM and AFM images for short polishing time, and (c) is for a longer polish. In (d) the surface has also been sputtered, revealing the alumina around the grains; this image was taken at a 45° angle.

strate, in this case a reduction of the intensity of about 4% from one air/glass interface. The WO_3 absorption length is shown in Figure 4.12(b) as well as the spectrum illuminating the film in the experiment calculated by multiplying the nominal 365 nm LED spectrum by the nominal optical filter transmission and measured transmission of the FTO substrate, then normalizing the overall power to the power measured in the experimental setup described in Section 4.3. At an illumination wavelength of 372 nm the power has dropped to 10% of the peak value at 365 nm, and here the absorption length is 400 nm. Thus, for the sputtered WO_3 thin films, the estimated minimum measurable diffusion length is 400 nm from requirement #2.

The optical bandgap E_g can also be determined from the spectral absorbance from the relation [86]

$$\alpha \propto \frac{(h\nu - E_g)^{n/2}}{h\nu}, \quad (4.13)$$

where $h\nu$ is the photon energy and $n = 4$ for indirect bandgaps or $n = 1$ for direct bandgaps. Thus a plot of $(\alpha h\nu)^{1/2}$ or $(\alpha h\nu)^2$ versus $h\nu$ reveals the indirect or direct bandgap, respectively, via the x-intercept (a Tauc plot). For the sputtered WO_3 films, this analysis gave an indirect bandgap of just below 2.8 eV similar to previous measurements of 2.6-2.8 eV [86, 90]. The direct gap appears to be in the range 3.4-3.6 eV, but the linear extrapolation is less clear.

4.2.3 Polishing films at an angle

The more general technique to make a wedge-shaped thin-film electrode is to polish a flat sample at an angle. However, since the films are on the order of 10^{-6} mm thick and the thickness gradient should be over 10^{-3} mm, very small angles are required and deep scratches can be a problem. In addition, slurries are often designed for polishing specific materials via both chemical and physical means, so a wide variety of polishing options are available but can also etch the sample. For example, the tungsten oxide films are unstable in basic conditions, so they were visibly damaged by polishing with colloidal silica slurry which is typically at pH 9-10. The best results were obtained by polishing with colloidal diamond at neutral pH which should be applicable to a wide

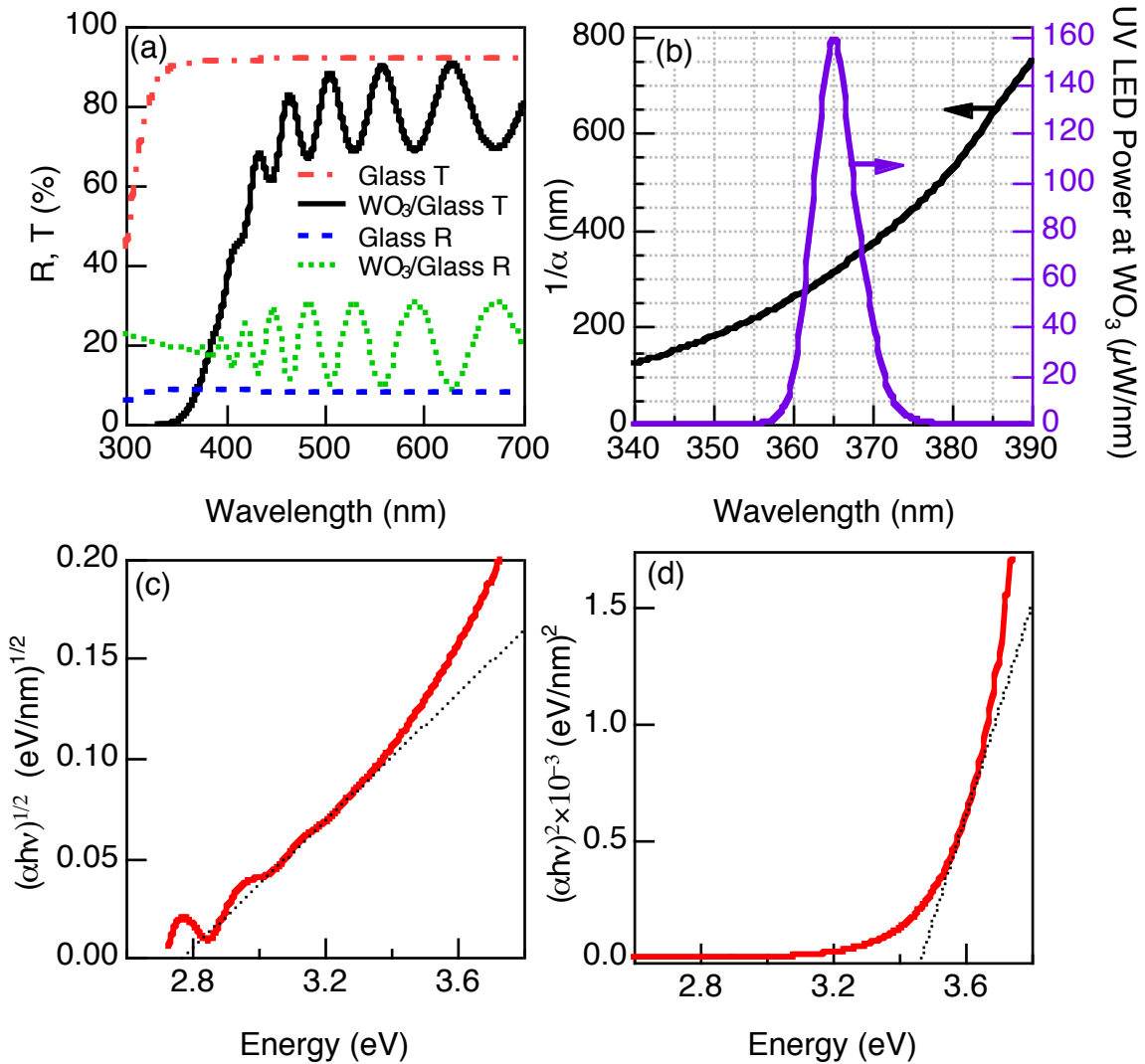


Figure 4.12 – Optical properties of WO_3 . (a) Reflection (R) and transmission (T) for glass and films on glass. (b) Absorbance calculated from R and T as well as calculated spectral power incident on WO_3 in the scanning photocurrent setup shown in Figure 4.13. (c) and (d) Absorbance plots determining indirect and direct bandgaps.

variety of materials. The tripod polisher can be used to define a very specific angle for polishing. A few tests were done to polish thin films into a wedge and the results were promising, but the sample preparation was tedious and time-consuming. However, polishing should provide a general technique for making a thickness gradient out of a wide variety of thin-film materials with further development.

Though polishing can leave many surface defects and damage on the polished surface, it was not found to be very detrimental to the performance of the tungsten oxide thin films. The photoresponse was very similar for films tested before and after polishing at least in the saturation photocurrent regime.

4.3 Diffusion length measurement: Photocurrent with scanned illumination

For back-side illumination of a wedge, a custom electrochemical cell with a fixed working electrode position and scanned illumination was built. The measurement requires strongly absorbed illumination and thus ultraviolet (UV) light for wide-bandgap semiconductors, but the substrate must be transparent to the illumination as well. A common substrate is F:SnO₂-coated glass, and the bandgap of tin dioxide is about 3.6 eV, limiting the shortest possible wavelengths of illumination to about 330-340 nm. Alternatively, a thin metal film back contact on quartz or sapphire would allow shorter wavelength illumination, but the semiconductor growth and quality may change on the metal electrode in any high-temperature steps that could cause diffusion of metal impurities. An ideal illumination source would be a UV argon-ion laser or UV excimer laser, but for space and cost considerations we chose to utilize a compact, high-power UV light-emitting diode (LED). A photo of the experimental setup is shown in Figure 4.13. The entire optical assembly was mounted on a movable stage and consisted of (from bottom to top) a Thorlabs high-power 365 nm LED, a 1 mm pinhole mounted close to the LED, a 365 nm center/10 nm full-width-half-max bandpass interference filter, a fused silica collimating condenser lens, a dichroic

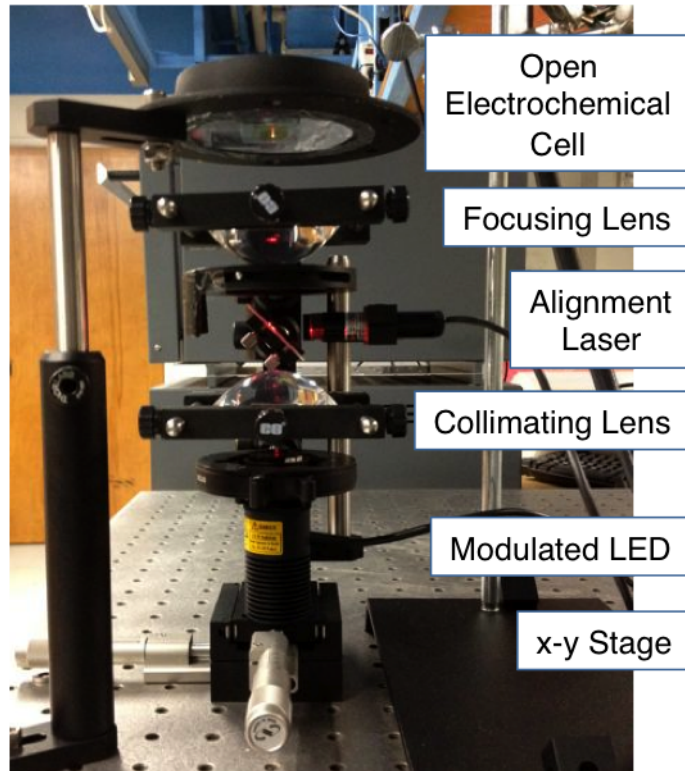


Figure 4.13 – Illumination and cell setup to scan illumination across an electrode.

mirror with a side-mounted 633 nm diode laser for alignment, an iris, and a fused silica focusing condenser lens. The LED could be conveniently modulated, and for these experiments it was chopped with a square wave at 0.5-2 Hz with a function generator. With this setup a focused spot about 1 mm in diameter with a power of 1.5 mW could be formed at the sample location. The UV LED was primarily used for electrochemical measurements, but other wavelengths at 455 and 500 nm were easily obtainable by simply swapping out the LED head.

The electrochemical cell consisted of a quartz bottom window epoxied to a ring-shaped support flange that could be filled with electrolyte. The sample under test was simply set on the quartz window, and a Ag/AgCl reference electrode and Pt mesh counter electrode were introduced from the top. The working electrode potential was controlled with a Biologic SP-200 potentiostat, and the measured current was output to a SRS830 lock-in amplifier to isolate the photocurrent from the dark current. The electrolyte used was unstirred, air-saturated 1 M H₂SO₄ / 2.4 M methanol, and

control experiments verified that stirring and sample orientation were not important due to the small currents involved and high electrolyte concentration. The methanol was added to act as a hole scavenger so that electrode reaction kinetics were not limiting; a fast redox couple could also be used if a well-defined potential is desired rather than simply good minority-carrier collection. Samples were contacted by gently scratching the WO_3/FTO film with a diamond scribe to expose some FTO, then a Teflon-coated silver wire was attached to the film with silver paint. The connection was protected with Kapton tape, and the wire assembly was finally insulated from solution by application of a few coats of MiccroStop lacquer or epoxy.

The optics were mounted on a motorized stage for easy data acquisition. In these experiments, the stage was moved in 0.5 mm increments with a period of 6 seconds to allow the photocurrent signal from the lock-in to stabilize between movements.

4.3.1 Silicon wedge

The photocurrent at zero voltage resulting from back-side illumination on the solid-state Si wedge/Pt Schottky junction was measured as a function of thickness for various strongly absorbed illumination wavelengths shown in Figure 4.14. The power levels were similar for all three wavelengths; the peak photocurrents for the 365, 455, and 500 nm illumination sources correspond to incident photon collection efficiencies (IPCE) of 3×10^{-5} , 2×10^{-3} , and 6×10^{-3} , respectively. The exponential decrease of photocurrent with thickness was nearly identical for all three wavelengths, and the diffusion length was measured with this technique to be $168 \pm 4 \mu\text{m}$ from the shown dotted-line linear fits, averaging the three wavelengths. The starting wafer doping was measured via four-point-probe resistivity to be $5.3 \times 10^{16} \text{ cm}^{-3}$, and the estimated corresponding diffusion length is $120 \mu\text{m}$ [85] but can vary depending on the wafer quality, so the measured value is well within the expected range. The profiles show excellent agreement with the analytical one-dimensional model with high back-contact surface recombination (compare to the blue dash-dotted trace in Figure 4.4).

The silicon wedge was illuminated from the lapped side which still had many

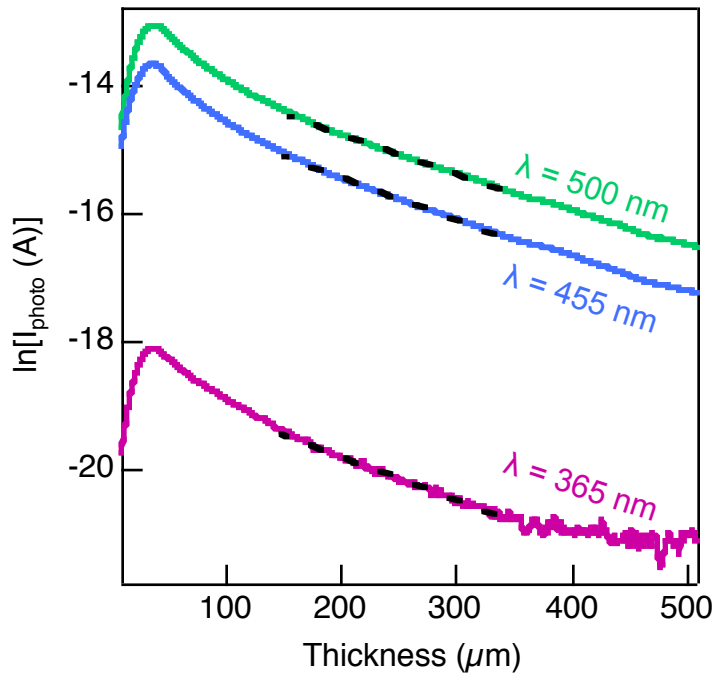


Figure 4.14 – Silicon wedge photocurrent for various wavelength illumination. Diffusion length given by inverse of the slope of the dotted linear fits.

micron-scale scratches left from the polishing procedure. Hence the surface recombination was rather high as evidenced by the lower overall photocurrent from the shorter-wavelength illumination and overall low IPCE values. The close agreement of the diffusion length measured by the three wavelengths shows that the measurement does not depend on the back surface quality or absorption length as long as the light is strongly absorbed.

4.3.2 Tungsten oxide wedges

The tungsten oxide films displayed typical onset potentials and photoelectrochemical behavior. A representative cyclic voltammetry sweep is shown in Figure 4.15 under chopped illumination so that the current both under illumination and in the dark is evident. The sweep was performed with the 1 mm focused illumination at an arbitrary point on the sample and under quiescent conditions with some exposed FTO, so the absolute values are somewhat different than the standard case of fully

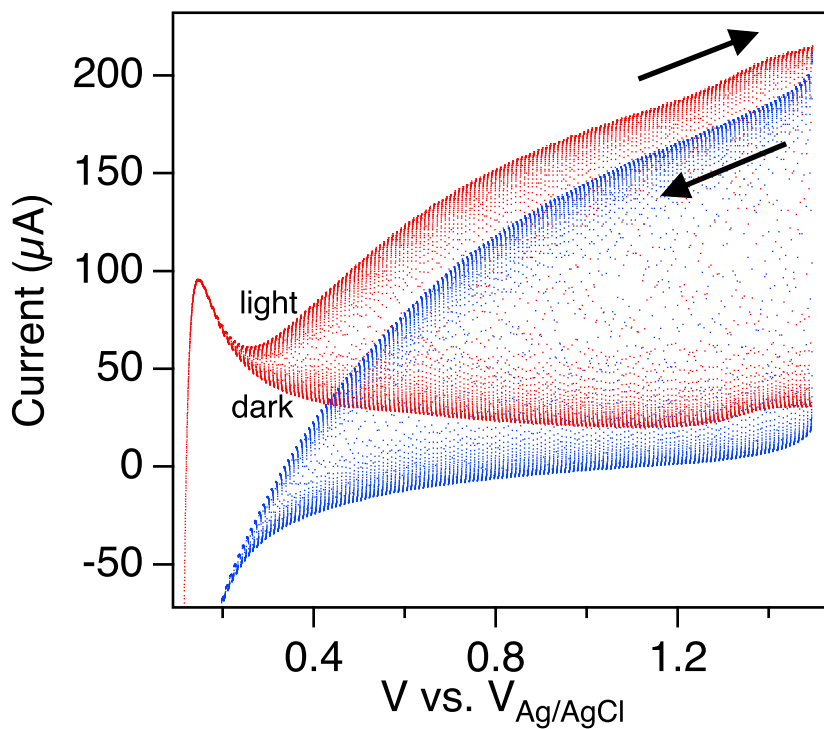


Figure 4.15 – Cyclic voltammetry sweep on a WO_3 sample grown at high temperature with back illumination chopped at 1.1 Hz and focused to a 1 mm spot at mid-thickness. Sweep rate was 10 mV/s in quiescent solution.

filled front illumination of a well-sealed electrode. However, the general curve shape is as expected for WO_3 with an onset potential of 0.2-0.3 V vs. $\text{V}_{\text{Ag}/\text{AgCl}}$ (0.4-0.5 V relative to the hydrogen potential) [91]. The photocurrent never fully saturates in this voltage range but begins to level off at voltages around 0.8-0.9 V vs. $\text{V}_{\text{Ag}/\text{AgCl}}$. For reference, the oxygen-evolution potential in this cell is at 1.03 V vs. $\text{V}_{\text{Ag}/\text{AgCl}}$.

The photocurrent was recorded as a function of thickness with the working electrode set to +1V vs. $\text{V}_{\text{Ag}/\text{AgCl}}$ unless otherwise noted. The WO_3 samples grown at lower temperature with the dense film morphology showed the expected exponential decay of photocurrent with thickness as shown in Figure 4.16. The rate of exponential decrease indicates a diffusion length of $L_p = 1000 \pm 100$ nm for this film, with the estimated error arising from which part of the profile is chosen to take the slope. The shown dotted line fit corresponds to $L_p = 1030$ nm, for example. This value is a few times higher than the measured absorption length, so it is in the valid measurement

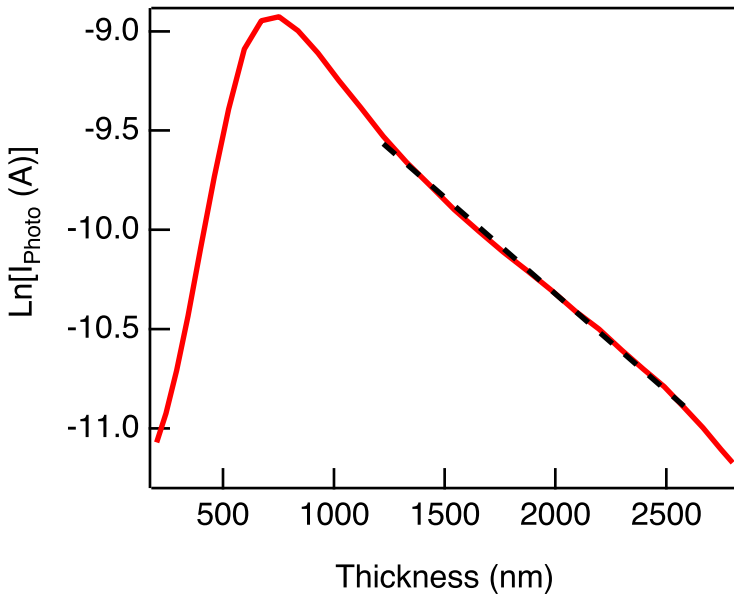


Figure 4.16 – Photocurrent as a function of thickness for back-illuminated WO_3 wedge electrode deposited at 180 °C. The inverse of the slope of the dotted line fit is the diffusion length.

regime.

The photocurrent vs. thickness profiles could depend on the voltage applied as seen in Figure 4.17. The system should be in photocurrent saturation but not fully depleted. For applied voltages just above the photocurrent onset threshold, the photocurrent could still show a decay with increasing thickness, but the slope of the decrease was different until a high enough voltage was applied to be in saturation. As in a spectral response measurement, the device should be in a light-limited regime, because nonideal effects such as junction-side recombination causes the assumptions of the theory behind this measurement to break down. For the WO_3 samples used here, an applied voltage of +1 V vs. $\text{V}_{\text{Ag}/\text{AgCl}}$ was sufficient to get results that did not depend on voltage. The sample in Figure 4.17 was deposited at 200 °C, and the measured diffusion length was slightly shorter at about 700 nm.

Though the XRD data for the sample shown in Figure 4.17 indicated the presence of the correct crystalline phase, the sample was annealed in air at 400 °C for two hours to ensure full crystallinity. After the anneal, the photocurrent no longer decreased with increasing thickness, and inspection under an optical microscope as well as SEM

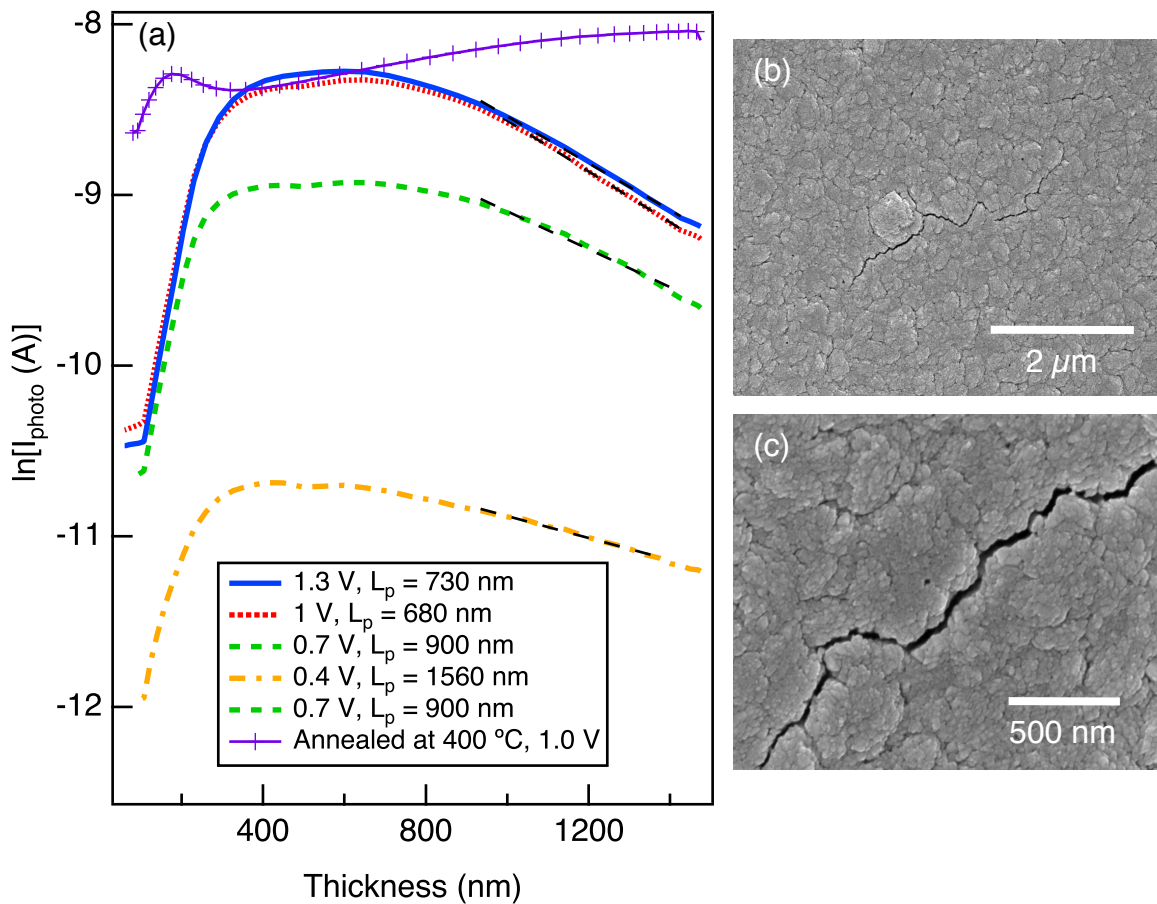


Figure 4.17 – WO_3 wedge photocurrent dependence on voltage and effect of annealing. (a) Photocurrent for sample deposited at 200 °C at various voltages; the effective diffusion length for each voltage shown in legend. Top curve is photocurrent after anneal at 400 °C. (b) and (c) SEM images of cracks resulting from anneal.

revealed the presence of cracks in the WO_3 film seen in Figure 4.17(b) and (c). The electrolyte could then enter the cracks and collect photogenerated carriers laterally rather than normal to the film surface. More cracks were present at the thicker side of the film due either to thermal stresses or growth defects, so the photocurrent actually increased as a function of film thickness even though the sample was illuminated from the back with strongly absorbed light.

For films deposited at 300-500 °C, the WO_3 was clearly crystalline but so porous that as deposited, the back-illuminated photocurrent did not decrease with increasing film thickness. The ALD aluminum oxide plus polishing treatment was necessary to see an exponential decay with thickness as seen in Figure 4.18. To show that this behavior was reproducibly treatable, two separate samples that showed this behavior are displayed. After the ALD and polish treatment, the diffusion length could be measured as 500-550 nm, which is somewhat lower than the samples deposited at lower temperature. The discrepancy could be due to an actual difference in the bulk of the grains, the properties of the grain boundaries, or increased grain-boundary recombination where the aluminum oxide was in contact with the tungsten oxide. This measured diffusion length is still longer than the absorption length. When two slopes for the exponential decay were seen as in Figure 4.18(b), the slope toward the thicker side was used because of the many profiles possible on the thin side (cf. Figure 4.4). For these samples, no dependence on voltage was found over the range 0.6 to 1.2 V vs. $\text{V}_{\text{Ag}/\text{AgCl}}$. These results open the possibility to use this technique on a wide variety of materials, relaxing the requirement of dense films; the effective collection length with an insulator on some grain surfaces is the measured parameter. To our knowledge the method of insulating porosity and sidewalls by ALD and polishing to achieve 1D carrier transport in photoelectrochemical cells has not been used before, but it is very useful for measuring semiconductor parameters on polycrystalline thin films.

The diffusion lengths measured here for tungsten oxide are similar to those found in the literature which range from 0.5 μm [86] to about 5 μm [93], and the particulars of the sample preparation are sure to cause variations in the material.

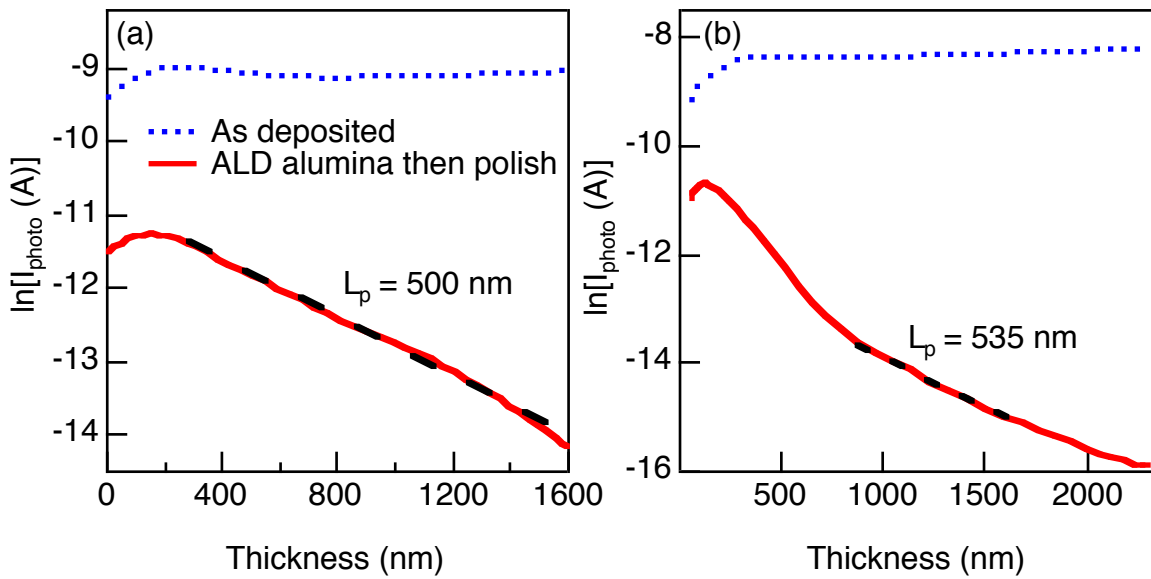


Figure 4.18 – Photocurrent for two separate electrodes (a) and (b) deposited at 400 °C both for samples as deposited with porosity and samples treated with ALD alumina and top surface polishing. Diffusion length determined by slope of dotted linear fit after pore insulation.

4.4 Conclusion

As a screening measurement to determine the minority carrier diffusion (collection) length in new semiconductor materials, the back-illuminated wedge technique has good potential as an independent measurement that does not require extensive knowledge of other semiconductor parameters. The calculations using one-dimensional diffusive transport in a quasineutral semiconductor and collection at an abrupt liquid-induced junction showed that the measurement is largely insensitive to the depletion width and back surface recombination. The technique was proven using both a polished silicon wedge and sputtered tungsten oxide wedge in which the diffusion length was measured in the range 500-1100 nm. However, the lower limit of measurable diffusion length is set by the light absorption length which practically means a few hundred nm for the photoelectrochemically stable wide-bandgap materials under consideration. As the bandgap decreases or becomes direct, the lower limit of measurable diffusion lengths should also decrease; for Si and GaAs the absorption length at 365-nm illumination is on the order of 10 nm. Another interesting, relevant case is GaP

with an indirect bandgap of 2.26 eV; for 365 nm illumination the absorption length is 50 nm [94].

Due to the high lower limit on measurable diffusion lengths via this technique, it is worth revisiting the use of a carrier lifetime measurement as a screening tool. Using the Einstein relation, eqn. 4.1 can be rewritten as

$$\tau = \frac{L^2 q}{\mu k T}, \quad (4.14)$$

where μ is the minority carrier mobility which is usually unknown but could be estimated as perhaps 0.1 cm²/Vs. A 100-200 nm diffusion length then corresponds to a lifetime around 100 ns which is within the measurable range for time-resolved measurements such as photoluminescence, photoabsorption, or microwave conductivity. If an order-of-magnitude estimate is possible for the minority carrier mobility/diffusivity, then a lifetime measurement could also provide a suitable screening method.

For measuring diffusion length, no single technique can provide an unambiguous answer for materials with largely unknown properties. The back-illuminated wedge technique can provide an accurate measurement of diffusion length requiring very few assumptions about the material under test, but the sample preparation can take some effort to create the wedge and ensure one-dimensional transport. The technique should be extended to other materials including electrode materials deposited by simpler methods such as spray pyrolysis or electrodeposition. In principle, polishing a wedge, insulating the sidewalls with a dielectric ALD layer, and then a final polish to expose the top surface should allow measurement on a wide variety of materials and assist the search for the ideal solar energy-conversion device material.

Chapter 5

Plasmonic hot carrier internal photoemission for energy conversion

The possibility of enhancing semiconductor photoelectrochemistry with plasmonics is intriguing, and the traditional enhancements applied to solar cells with light scattering and concentration should apply as well [95, 96]. However, we were interested to know if a plasmon resonance could affect the overpotentials in catalysis, and this line of thinking led to metallic hot carrier effects [97] involving photoemission of electrons into solution. However, since the details of plasmon to hot electron coupling are not fully understood, we chose to utilize a solid-state device inspired by the solid-state plasmonic hot electron infrared detector experiment by Knight and Halas [98]. This chapter explores the efficiency limits of solid-state internal-photoemission energy conversion devices and discusses an experiment to test the assumptions of the classical theory.

5.1 Introduction

Many semiconductor devices that convert light energy to electrical energy have been developed, but a fundamental limitation on the spectral range and efficiency arises due to the threshold of light absorption at the bandgap energy. Once excited, electron-hole pairs in semiconductors can be long-lived and thus separated and collected. Adding a second material interfaced with the semiconductor opens up the possibility to absorb and collect sub-bandgap photons as in dye-sensitized solar cells or Schottky-

barrier focal-plane-array infrared detectors. In this case, the photon is absorbed in the second material, and an excited “hot” electron or hole is injected into the semiconductor and collected. In this context, a hot electron refers to an electron not in thermal equilibrium with the electron gas but instead with an energy larger than that expected from the thermal distribution. It has recently been demonstrated that nanometer-scale metallic particles or antennas with a surface plasmon resonance can enhance this sub-bandgap absorption which leads to increased efficiencies and spectral selectivity [98, 99, 100, 101]. Here we focus on the case of metallic plasmonic devices in a solid-state Schottky-barrier device or metal-insulator-metal geometry. We will refer to the hot carriers as electrons considering n-type semiconductors, though similar considerations apply to hot-hole devices.

The decay of surface plasmon resonances is usually a detriment to the field of plasmonics [102], but here we are utilizing the damping to excite and collect hot electron-hole pairs. The possibility to capture the energy normally lost to heat would open new opportunities in photon sensors and energy conversion devices. Dephasing of the electron gas oscillation leads to hot electron-hole pair generation with the energy separation determined by the incident photon energy [103], and the yield of incident photons converted to hot charge carriers is enhanced in the presence of a plasmon resonance due to increased local electromagnetic fields and absorption. These hot electrons thermalize with the electron gas on the order of 10-100 femtoseconds, slightly increasing the temperature of the electron distribution relative to the lattice; phonon coupling subsequently increases the lattice temperature within a few picoseconds to reach thermal equilibrium. For internal photoemission, we are most interested in the dynamics of the hot electron quasiparticles before thermalization with either the electron gas or the lattice; though the timescales involved are very short, the high Fermi velocity means that hot electrons can travel tens of nanometers while retaining energy up to the plasmon energy above the Fermi energy.

In the field of photoelectrochemistry, direct utilization of the hot carrier energy would be particularly useful for two reasons. First, the semiconductor materials that are stable for oxygen evolution are typically oxides with wide bandgaps which absorb

little of the solar spectrum [25], and any way to collect the sub-bandgap light would be very useful. Second, electrochemical reactions involve activation-energy barriers for electron transfer from the absorbing material to the molecules of interest which lead to unwanted overpotentials. Hot electrons could more easily bypass these barriers if they could be captured in the molecule before back transfer, so in this way light would be enhancing the performance of dark electrocatalysts or semiconductor surfaces [104, 105]. For example, the CO₂ reduction reaction involves an initial electron-capture step with an overpotential of about 0.4 V [106], and the use of plasmonics to directly inject hot electrons into solution would open new opportunities in photoelectrochemistry and solar fuels. However, some fundamentals of plasmonic hot-electron emission are still unclear, so to better understand the physics involved we chose to test solid-state devices rather than photoelectrochemical devices.

Though many experiments show increased yield with plasmonic particles, the hot-electron emission effect often can be difficult to distinguish from various other effects such as local field-enhanced excitation of subgap states in the semiconductor, physical changes induced in the defect structure, localized heating, or chemical effects. Plasmonic enhancement has been presented for photoelectrochemical devices [107, 100, 108, 96, 109, 110], photochemical devices and processes [111, 112, 113, 114, 115, 116, 117, 118], and heterogeneous catalysis processes [119, 120]. Though many of the results have been presented as a plasmon-to-hot-electron mechanism, the enhancement mechanism can be ambiguous even for solid-state devices (see Section 5.2.8), and when a chemical reaction is involved thermal effects should not be overlooked.

A mature technology based on internal photoemission is Schottky near-infrared (NIR) detectors which are mainly interesting because the fabrication is compatible with traditional complementary metal-oxide-semiconductor (CMOS) processing, enabling large focal-plane-array detectors [121]. Though the quantum efficiency is low compared to photovoltaic-type NIR detectors at about 1% [122], it was discovered that very thin emitter films enhanced emission through scattering into the small escape cone of hot carriers, and coupling to Fabry-Perot optical cavities could retain high absorption and enable appreciable efficiency [121]. Plasmonics offers a new way

to enhance the absorption for these detectors and enables spectral selectivity as well [98].

For Schottky-barrier photodetectors, the spectral dependence of the internal photoemission yield has long been known to follow a Fowler law [123, 124] based on a semiclassical description of the hot electron excitation, transport, and emission from the metal into the nearby semiconductor known as the three-step model which is outlined in Section 5.2. The magnitude of the internal photoemission yield is typically very small due to the energy distribution of excitation energy and to the small escape cone, and here we examine whether the underlying physics and approximations also apply to plasmonic hot carriers or if other effects are expected in Section 5.2.7. If we assume that carrier excitation is nondirect so as to de-correlate the electron momentum distribution with the original plasmonic electric field, the maximum external quantum efficiency is on the order of 10^{-2} on resonance. The presence of a lossy adhesion layer such as titanium can also affect the spatial hot carrier generation as well as the barrier energy and quality. Here, we couple optical finite-element simulations of such devices to the internal photoemission model for hot-carrier collection efficiency and compare calculations to experiment to elucidate the underlying mechanisms. Models for correlated and uncorrelated electron distributions are compared to experimental measurements for Au/Si hot carrier injection quantum efficiency as a function of electric field wavevector and polarization. A buried-antenna geometry was fabricated in order to test any correlation between hot-electron momentum and plasmon polarization, detailed in Section 5.4.

The possibility of solid-state solar energy-conversion devices is also analyzed in Section 5.2.5. In this case the diode is operated in forward bias, and the thermionic emission current is a major detriment. Considering the power conversion efficiency as a function of barrier energy, the best-case values (total solar absorption in a 20 nm thick metal film) are limited to around 0.3% at room temperature. Increasing the maximum efficiency of such devices is possible by either cooling or relaxing the escape cone restriction, possibly by correlation of the plasmon electric field with the hot carrier electron momentum. The aim for higher possible efficiencies motivated

the experimental work here in attempts to direct the hot electron momentum normal to the collecting interface.

5.2 Theory of plasmon-enhanced internal photoemission

The hot carriers can be emitted from the metal into a dielectric or semiconductor contact, measurable in an internal or external photoemission current. A traditional photoemission yield calculation consists of the three-step model: (1) photon absorption, (2) hot carrier transport, and (3) emission over the surface barrier leading to the Fowler expression for photoemission yield [92],

$$Y_{Fow}(\hbar\omega) = C_F \frac{(\hbar\omega - \phi_b)^2}{\hbar\omega} \quad (5.1)$$

where $\hbar\omega$ is the photon energy, ϕ_b is the barrier height energy, and C_F is the Fowler coefficient on the order of $(8E_F)^{-1}$ but depends somewhat on materials and geometry. Eqn. 5.1 will be re-derived below and the assumptions analyzed in hopes that the yield can be enhanced by clever choice of geometry or materials. Here we assume similar physics hold in the presence of a plasmon resonance which serves to increase absorption in the metal. Only the collection of one type of hot carrier is considered, in this case hot electrons over a barrier ϕ_b to the conduction band because either a large valence band barrier or a Schottky-barrier electric field can reduce hot hole photocurrent into an n-type semiconductor. The basic device band structure under consideration is shown in Figure 5.1(a). In this geometry, the z direction is normal to the metal/dielectric interface.

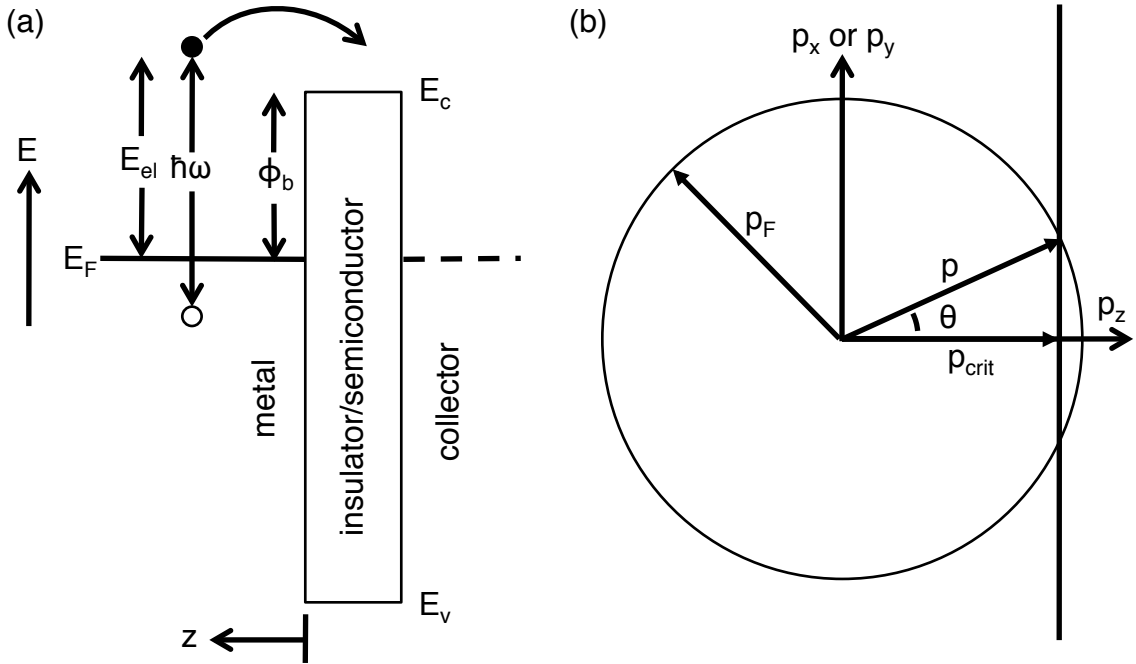


Figure 5.1 – (a) Band structure for internal photoemission and (b) momentum escape cone.

5.2.1 Hot electron excitation

Light absorbed in a metal can be fundamentally described quantum-mechanically where the photon's field is a perturbing Hamiltonian of the form

$$H' = -\frac{e}{m} \mathbf{A} \cdot \mathbf{p} \quad (5.2)$$

where e is the electron charge, m is the electron mass, \mathbf{A} is the vector potential of the electromagnetic field, and \mathbf{p} is the momentum operator [125]. Due to this perturbation, the optical absorption between quantum states $|i\rangle$ and $|f\rangle$ ignoring the small photon momentum is proportional to $|\mathbf{a} \cdot \langle f | \mathbf{p} | i \rangle|^2$ where \mathbf{a} is the unit vector parallel to \mathbf{A} . Thus the electronic transition should have a momentum component along the direction of photon polarization to be allowed. Practically, the effects of quantum mechanical transitions and overall responses of the material to perturbing photons are described by a frequency-dependent dielectric function ϵ that is determined experimentally. Classical electrodynamics then describes the energy flow as a

Poynting vector $\mathbf{S} = \mathbf{E} \times \mathbf{H}$ where \mathbf{E} and \mathbf{H} are the electric and magnetic fields. The spatial power absorption is given by the divergence of the Poynting vector which by Maxwell's equations can be written as [126, 127]

$$P_{abs} = -\frac{1}{2}\text{Re}[-\nabla \cdot \mathbf{S}] = -\frac{1}{2}\omega |E|^2 \text{Im}[\epsilon], \quad (5.3)$$

where P_{abs} is the absorbed power and ω is the photon frequency. This calculation of spatially absorbed power is easily applied to full-field finite-element software methods where the fields are calculated throughout an arbitrary structure. If the imaginary part of the dielectric function is assumed to represent the excitations of single electron-hole pairs only (no direct coupling between photons or plasmons with phonons or other excitations), then in this approximation the absorbed power normalized to the incoming photon energy directly represents the generation rate of hot electron generation per volume or length, $\eta_e(z)$. Note that this correspondence between spatial power absorption and spatial hot electron generation is an assumption linking classical electrodynamics with quantum quasiparticle excitations through a simple homogeneous, local, linear permittivity ϵ determined from measurements on bulk materials. The details of the actual photon interaction with the crystal lattice including the dephasing of the conduction electrons' response in the presence of surfaces and collective plasmon excitations would require a detailed quantum mechanical calculation beyond the scope of this thesis. The assumed one-to-one correspondence between photons and hot electron-hole pairs neglects other photon/plasmon absorption pathways involving phonons or other excitations because the probability of interaction is lower for processes involving more quasiparticles.

After absorption, the excited electron's energy and momentum is distributed according to the density and band structure of initial and final states in the metal. The hot electron may have an energy E_{el} above the Fermi energy ranging from zero up to the photon energy. Its probability distribution depends on the detailed band structure, but for excitations not too far from the Fermi level, a parabolic band structure is a good approximation where the density of states $g(E)$ is proportional to the

square root of energy. For the gold structures considered here, the electronic density of states is a roughly constant function of energy within ± 1.6 eV of the Fermi energy [128]. Since the optical transitions must therefore be nondirect intraband transitions with the missing momentum supplied by surfaces, defects, or phonons, the transition probability is just the multiplied probability of an occupied initial state and the probability of an unoccupied final state [129]. At zero Kelvin the hot electron excitation energy distribution is given by

$$P_0(E_{el}) dE = \frac{(\text{final states})(\text{initial states})}{\text{all transitions}} \quad (5.4)$$

$$= \frac{g_{final}(E)g_{initial}(E) dE}{\int g_{final}(E')g_{initial}(E') dE'} \quad (5.5)$$

$$\stackrel{\text{free electron, 0 K}}{=} \frac{\sqrt{E_F + E_{el}}\sqrt{E_F + E_{el} - \hbar\omega} dE}{\int_{E_F}^{E_F + \hbar\omega} \sqrt{E'}\sqrt{E' - \hbar\omega} dE'} \quad (5.6)$$

which slightly favors hot electron over hot hole production, though the difference is small if E_F is large as in gold where $E_F = 5.5$ eV [130]. Note that this hot electron energy distribution function breaks down for higher photon energies that can excite intraband transitions. For intraband transitions, the probability of direct momentum-conserving vertical transitions is much higher and the joint density of states should be considered. However, for all yield calculations performed here, nondirect transitions were assumed. While eqn. 5.4 has meaning under an integral, a plot of $P_0(E_{el})\hbar\omega$ gives an idea of the transition probability to various energies compared to a uniform distribution $P_{0,\text{uniform}} = (\hbar\omega)^{-1}$. Figure 5.2 shows the excitation probability for both the case of free-electron-like bands with $E_F = 5.5$ eV and the case considering the DFT-calculated density of states of gold [128]. These plots should be interpreted as the relative probability that a photon of a given energy will excite a hot electron to a certain energy, and an integral along a horizontal line will return the photon energy (not 1) for clearest visualization comparing different photon energies. For free-electron-like bands, the distribution does not vary much from a uniform distribution, while for Au this approximation is most reasonable up to 1.6 eV. The tails of the Fermi distribution at finite temperature will slightly affect P_0 , but here the distribution at

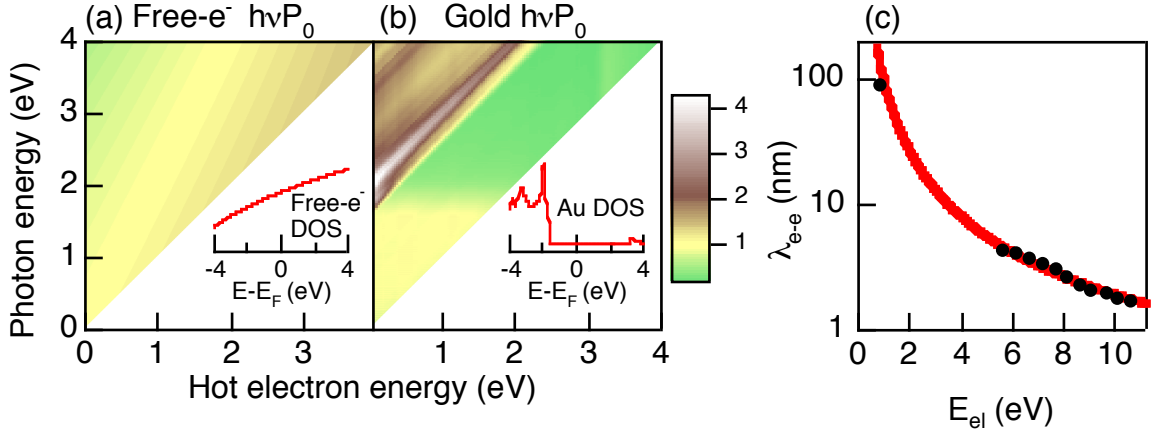


Figure 5.2 – Energy distribution probabilities (a) and (b) and mean free path for hot electrons in Au (c). The insets show the density of states (DOS) of either a free-electron approximation (a) or a DFT calculation (b), and the color scale shows the probability of excitation to a given energy. The electron-electron scattering mean free path model is shown in (c) along with experimental data points from ref. [131].

0 K was used for calculations.

5.2.2 Hot electron transport

Once excited, the hot electrons move as quasiparticles through the material and undergo quasi-elastic electron-phonon collisions as well as inelastic electron-electron collisions. Even though the hot carriers may decay in less than a picosecond, the Fermi velocity around 10^{15} nm/s means that an excited electron may travel hundreds of nm before losing its energy. In addition, electrons with energy slightly above the Fermi level may only scatter off electrons with energy slightly below the Fermi level. A good analytical model for the mean free path of electron-electron scattering was developed by Quinn and given mathematically as [132, 133]

$$\lambda_{e-e}(E_{el}) = \frac{24a_0\sqrt{\alpha_e r_s/\pi}(3E_F/E_{el}^2 + 2/E_{el})}{\tan^{-1}\sqrt{\frac{\pi}{\alpha_e r_s}} + \frac{\sqrt{\alpha_e r_s/\pi}}{1+\alpha_e r_s/\pi}}, \quad (5.7)$$

where a_0 is the Bohr radius (0.0529 nm), $\alpha_e = \sqrt{4/9\pi}$, and r_s is the radius of a sphere equal to the volume of one electron in units of the Bohr radius. For gold, $r_s = 3$. This distance represents the average energy a hot electron travels before losing half

its energy, and here it is assumed that this energy loss is sufficient to eliminate any chance of emission over the barrier. Eqn. 5.7 is plotted in Figure 5.2(c), and good agreement is seen with the experimental points. For now we ignore phonon scattering, assuming that no energy is lost during these quasi-elastic collisions.

The direction of hot electron motion after excitation is unclear, but two scenarios are considered here. The first common assumption [134, 135, 136, 137] is that the distribution of the excited quasiparticle momentum is isotropic because nondirect transitions could be allowed from any part of the Fermi surface (within the photon energy) to an excited state. In this approximation, there is no preference for a given direction in k -space for the hot electron. The second scenario assumes that the direction of hot electron motion is fully correlated with the photon polarization because especially in the case of plasmon excitation, a photon's electric field excites motion along the polarization direction which upon excitation of a single electron-hole pair could eject the hot electron along the same direction as the field. These two scenarios will be discussed further and tested experimentally in Section 5.4.

For an isotropic hot electron momentum distribution, the probability that an electron excited at depth z in a semi-infinite bulk slab will reach the interface is given by

$$P_{int}(z, \theta, E_{el}) \sin \theta \, d\theta = \frac{1}{2} \exp \left(-\frac{z}{\lambda_{e-e}(E_{el}) \cos \theta} \right) \sin \theta \, d\theta, \quad (5.8)$$

where the prefactor of $1/2$ is because half the electrons are traveling away from the interface and θ is the azimuthal angle from the surface normal (z).

5.2.3 Hot electron emission

If incident on the metal-semiconductor interface, the probability of emission into the semiconductor depends on both the hot electron energy and the component of momentum normal to the interface in a classical model first proposed by Fowler [138] to best describe the experimental energy dependence of the photoemission yield. The component of electron momentum normal to the surface p_z must be high enough to overcome the barrier p_{crit} , which leads to a small escape cone of allowed momenta

shown schematically in Figure 5.1(b). The critical momentum p_{crit} of electron emission defines a maximum angle of hot electron incidence that still allows escape,

$$\theta_{max} = \cos^{-1} \frac{p_{crit}}{p} = \cos^{-1} \sqrt{\frac{E_F + \phi_b}{E_F + E_{el}}}, \quad (5.9)$$

and since for internal photoemission typically $E_F \gg E_{el}$, this defines a rather small angle. In particular the fraction of electrons incident on the interface that are reflected rather than emitted is

$$\begin{aligned} R_{elec} &= 1 - T_{elec} = 1 - \int_0^{\theta_{max}} \sin \theta \, d\theta \\ &= \sqrt{\frac{E_F + \phi_b}{E_F + E_{el}}} \approx 1 - \frac{E_{el} - \phi_b}{2E_F} \end{aligned}$$

which is not far from 1 due to the large Fermi energy (or large size of the Fermi surface in k -space) compared to the barrier height or photon energy.

The critical angle of escape analysis assumes a perfect, planar interface, but for a rough interface the escape cone may be larger and the normal momentum constraint relaxed. As a best-case scenario, one could consider that all hot carriers reaching the interface with sufficient energy can escape regardless of momentum direction which can be considered here by setting $\theta_{max} = \pi/2$ so that $R_{elec} = 0$. Also accounting for one specular reflection of a hot carrier at the back surface of a thin film, the probability of reaching the collecting interface becomes

$$P_{int,refl}(z, \theta, E_{el}) \sin \theta \, d\theta = \left[\frac{1}{2} e^{\left(-\frac{z}{\lambda_{e-e}(E_{el}) \cos \theta} \right)} + \frac{1}{2} e^{\left(-\frac{2w-z}{\lambda_{e-e}(E_{el}) \cos \theta} \right)} \right] \sin \theta \, d\theta, \quad (5.10)$$

where w is the structure thickness.

5.2.4 Fowler yield and extensions

Having now developed the three steps of photoemission, the overall yield for one type of hot carrier can be calculated at a given photon energy as

$$Y(\hbar\omega) = \int_{\phi_b}^{\hbar\omega} dE_{el} \int_0^{\theta_{max}} \sin \theta \, d\theta \int_0^\infty dz \, P_0(E_{el}) P_{int}(z, \theta, E_{el}) \eta_e(z, \hbar\omega), \quad (5.11)$$

where any reductions from quantum mechanical reflections or back-scattering in the collector from defects or image forces are neglected. In addition, quantum-mechanical tunneling for energies below the barrier has been neglected due to its small contribution [99, 139]. Under the conditions (i) $p_{crit} \approx p_F$ so that the escape cone is small, (ii) absorption length $1/\alpha$ short compared to λ_{e-e} , and (iii) constant distribution of hot electron energies so that $P_0(E_{el}) \approx (\hbar\omega)^{-1}$, the integrals can be simply evaluated to return eqn. 5.1. A notable property of the Fowler yield expression is the small prefactor, which means that the yield increases slowly for photon energies slightly above the barrier height.

In the case of thin metal emitters where the thickness is on the order of the electron-electron scattering mean free path, the yield can be enhanced significantly due to Lambertian reflections of the back interface. In addition, phonon scattering with a mean free path λ_{e-p} which is around 20 nm [133] can actually enhance the yield because it can redirect the charge carrier momentum to directions within the escape cone, and the energy lost during photon scattering is small [140, 141]. Again considering the case of $p_{crit} \approx p_F$ where the escape cone is small, Dalal [135] has derived an enhanced yield expression considering phonon and back-surface scattering. In this model, the angular integral over P_{int} is replaced with a function $q(z)$ such that the enhanced yield is given by

$$Y_{enh}(\hbar\omega) = \int_{\phi_b}^{\hbar\omega} dE_{el} \int_0^\infty dz \, P_0(E_{el}) q(E_{el}, z) \eta(z, \hbar\omega), \quad (5.12)$$

$$q(E_{el}, z) = A_w e^{\mu z} + B_w e^{-\mu z},$$

$$A_w = e^{-2\mu w} B_w,$$

$$B_w = \frac{1 - R_{elec}}{(1 - R_{elec})(1 + e^{-2\mu w}) + (1 + \lambda_{e-e}/\lambda_{e-p})^{-1/2}(1 + R_{elec})(1 - e^{-2\mu w})},$$

$$\mu = \sqrt{(\lambda_{e-e}^{-1} + \lambda_{e-p}^{-1})^2 - \lambda_{e-p}^{-1}(\lambda_{e-e}^{-1} + \lambda_{e-p}^{-1})},$$

where w is the structure thickness. The above integral was performed numerically for various geometries considered below. For the case of emission from a bulk emitter, phonon scattering effectively boosts the yield by a factor $\sqrt{\lambda_{e-e}/\lambda_{e-p}}$ [141, 133].

If the initial electron motion is correlated with photon polarization, the probability of the direction of motion being within the escape cone can be much higher for the correct polarization direction. However, phonon scattering is considered here to isotropically redirect the momentum, so the effect will only change the results for excitation within a short distance of the collecting interface; after phonon scattering, eqn. 5.12 will hold. On the other hand, if the photon polarization is parallel to the interface, the carriers can only be collected after a phonon scattering event. The following two expressions were used for polarization-dependent internal photoemission yield, where \perp and \parallel refer to perpendicular (p) and parallel (s) polarization, respectively:

$$Y_{enh,\perp} = \int_{\phi_b}^{\hbar\omega} dE_{el} \int_0^\infty dz P_0(E_{el}) \left[\frac{1}{2} e^{-z/\lambda_{e-p}} + \left(1 - \frac{1}{2} e^{-z/\lambda_{e-p}}\right) q(E_{el}, z) \right] \eta(z, \hbar\omega) \quad (5.13)$$

and

$$Y_{enh,\parallel} = \int_{\phi_b}^{\hbar\omega} dE_{el} \int_0^\infty dz P_0(E_{el}) e^{-\lambda_{e-p}/\lambda_{e-e}} q(E_{el}, z) \eta(z, \hbar\omega). \quad (5.14)$$

5.2.5 Voltage dependence and power conversion efficiency

Current-voltage curves can be calculated by considering the voltage dependence of the barrier height and reverse current. As voltage is applied to the metal emitter, the band structure will adjust as shown in Figure 5.3 for a few cases of voltage. At this point also we generalize to an asymmetric metal-insulator-metal (MIM) structure [99] with different barrier heights on either side of the insulator; a metal-semiconductor Schottky contact is essentially the limit where $\phi_{b,2} \rightarrow 0$. The effect of voltage is

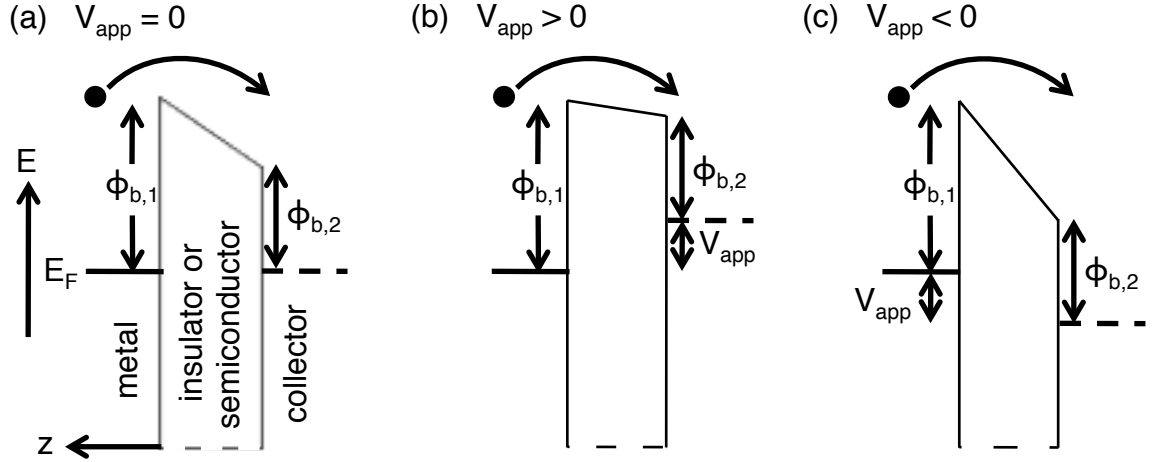


Figure 5.3 – Band structure for IPE with applied voltage for an asymmetric MIM at zero, positive, or negative voltage applied to the metal emitter.

to change the effective barrier heights to electron emission, modifying the limits on the energy integral in the yield equation. The notation is somewhat complex but straightforward for the various cases so it is not written explicitly here. Though such devices can be made with either a Schottky-barrier metal-semiconductor geometry or a metal-insulator-metal diode, the maximum power conversion efficiency of either device was found to be equal as in Figure 5.4(f), so here we primarily discuss Schottky-barrier-type devices.

The reverse dark current is primarily due to thermionic emission from the collector to the metal, especially for positive voltage applied to the metal. The thermionic current is given by (positive currents flow from the metal to the collector)

$$J_{TE}(\phi_{b,1}, \phi_{b,2}, V) = \begin{cases} A^* T^2 e^{-\phi_{b,1}/(kT)} (1 - e^{V/(kT)}) , & V \leq \phi_{b,1} - \phi_{b,2} \\ A^* T^2 e^{-\phi_{b,2}/(kT)} (e^{-V/(kT)} - 1) , & V \geq \phi_{b,1} - \phi_{b,2} \end{cases} , \quad (5.15)$$

where $A^* = 120 \text{ A cm}^{-2} \text{ K}^{-2}$ is the Richardson constant. To better represent thermionic emission involving a semiconductor like silicon, here the optimistic value $A^* = 50 \text{ A cm}^{-2} \text{ K}^{-2}$ was used instead [92] to reflect the change in carrier effective masses. The thermionic emission current is a major detriment for energy conversion devices, though for detectors it can be suppressed by cooling and operating in re-

verse bias [122]. A current-voltage curve can be drawn by summing the photocurrent density for an illumination spectrum $P_{ill}(\hbar\omega)$ in W cm⁻² eV⁻¹ which is $J_{photo} = \int P_{ill}(\hbar\omega)Y_{enh}(\hbar\omega)/(\hbar\omega/q) d(\hbar\omega)$ with the dark thermionic emission current density. The open-circuit voltage is not straightforward to determine, since the free energy of a hot carrier is approximately the difference between the photon energy and barrier height which varies with wavelength. The available voltage increases with increasing photon energy and decreasing barrier height; however, the dark current also increases for decreasing barrier height. Since this hot-carrier emission device is a majority-carrier device, any attempts to reduce the majority carrier dark current by adding a thin insulator barrier layer as in Schottky barrier photovoltaic cells [142] will also reduce the hot carrier current.

The energy conversion efficiency in percent for an illumination spectrum $P_{ill}(\hbar\omega)$ can then be simply written as

$$\% \text{ efficiency} = \frac{\left(\int P_{ill}(\hbar\omega)Y_{enh}(\hbar\omega)/(\hbar\omega/q) d(\hbar\omega) + J_{TE}(\phi_{b,1}, \phi_{b,2}, V) \right) V}{\int P_{ill}(\hbar\omega) d(\hbar\omega)} \times 100. \quad (5.16)$$

The voltage at the maximum power point is not easily extracted, so for these calculations the power was determined at voltages ranging from 0 to ϕ_b , then the maximum power point was numerically extracted. The optimal barrier depends on the illumination spectrum, materials involved, and operating temperature; the optimal operating voltage is around $\phi_b - 0.6$ eV at 300 K or $\phi_b - 0.15$ eV at 77 K which is due to the thermionic emission current at the respective temperatures. For ease of numerical integration in considering solar energy conversion, the sun was approximated as a 5800 K blackbody which reasonably reproduces the AM1.5d spectral shape.

A few example plots of the calculations performed are shown in Figure 5.4 for a top-illuminated Au film on Si where the generation profile is a simple exponential (Beer's law) with an absorption length of 10 nm. Unless varied, in these examples the film is 20 nm thick, the barrier $\phi_{b,1}$ is 0.8 eV, and the incident light has energy 1 eV. The metal is assumed to have free-electron-like bands with $E_F = 5.5$ eV, and the yields shown here are *internal* quantum yields considering only absorbed photons.

The yield can be significantly enhanced by an order of magnitude by accounting for phonon scattering and reflections in thinner emitter layers as shown in the thickness dependence of the yield enhancement in Figure 5.4(a), though in real devices the absolute yield is usually reduced by less light absorption. The spatial distribution of both hot carrier excitation and partial yield is shown in Figure 5.4(b). The generation is just the exponential absorption for this thin film example, and the yield from each point in space follows the generation for the most part because the hot electron mean free path is long enough to allow good collection over this entire film thickness. In Figure 5.4(c), the yield first rises parabolically above the threshold at 0.8 eV, but for higher photon energies the reduced λ_{e-e} lowers the yield. The deleterious effect of thermionic emission is shown in Figure 5.4(e), where current-voltage curves are shown both in the case of neglecting and accounting for J_{TE} at 300 K. The energy conversion efficiency for a variety of MIM configurations is shown in Figure 5.4(f), where it can be seen that the maximum conversion efficiency is equal for any combination of barrier heights though at different barriers; a Schottky-barrier-type device is along the horizontal axis, and the optimum barrier for this absorber geometry is slightly above $\phi_b = 1.1$ eV, similar in this case to the optimum bandgap for a semiconductor photovoltaic device.

It should be noted that in the above equations, only hot electron emission was considered, and it was assumed that the barrier for holes is larger. Similar physics hold for hot hole emission, and if both carrier types are active for internal photoemission, the overall yield will be lower which should be considered in the case of energy conversion for the entire spectrum. Similarly, only hot electron emission was considered from the front emitter layer, and any hot electrons photoemitted backwards from the collector layer will reduce the yield.

The solar energy conversion percent efficiency of some different cases of internal photoemission devices is shown in Table 5.1, where best-case scenarios were considered. The device under consideration is a Schottky-barrier-type device with optimal barrier and operating voltage. The illumination spectrum is a 5800 K blackbody up to a cut-off energy $\hbar\omega_{max}$ such as a semiconductor bandgap, 1.1 eV for Si or 3 eV for

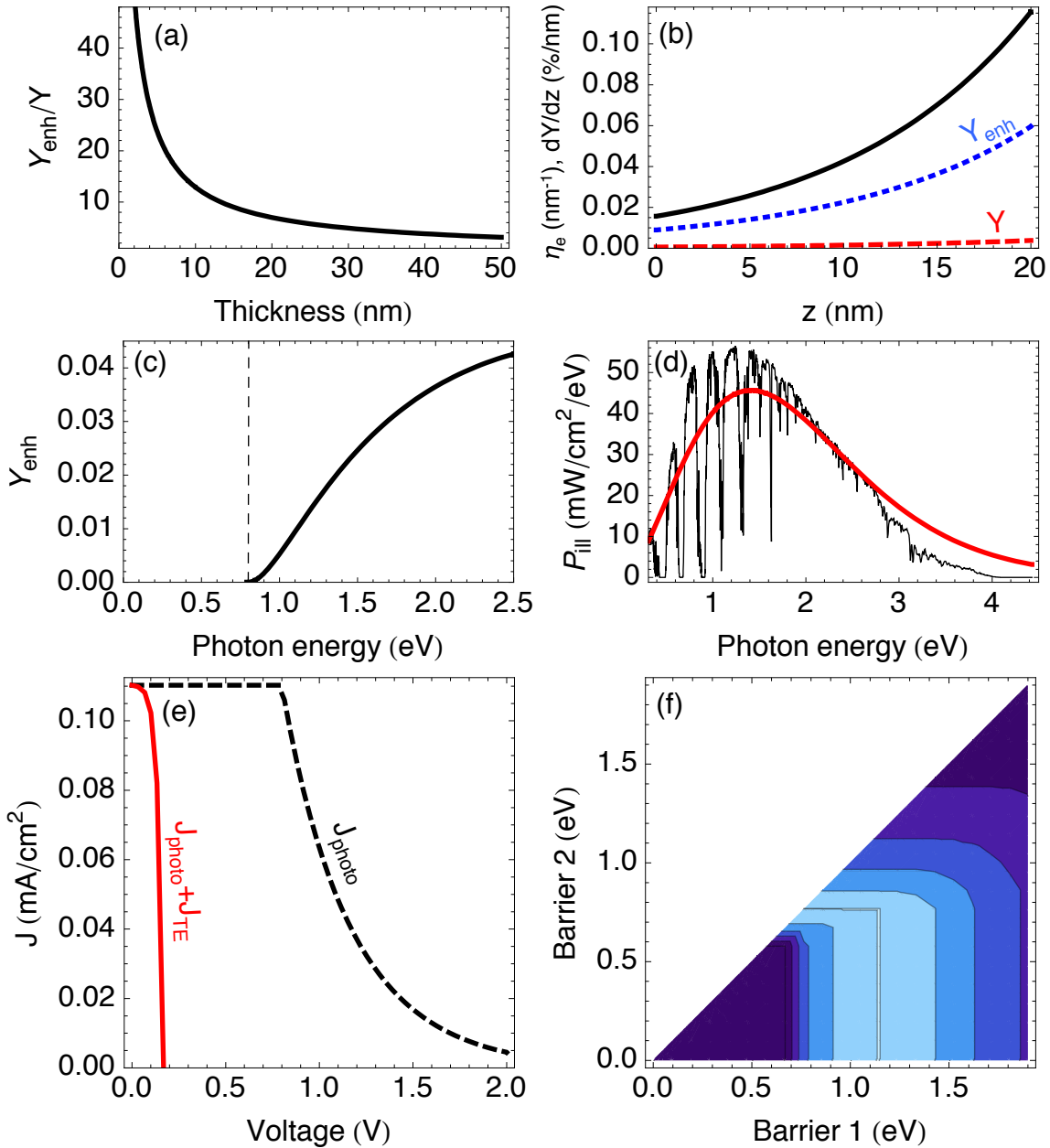


Figure 5.4 – Sample IPE calculations and considerations for a thin-film emitter. (a) Yield enhancement considering phonons and reflections. (b) Yield as a function of depth in a 20-nm-thick film. (c) Yield as a function of photon energy. (d) AM1.5D and 5800 K blackbody spectrum. (e) Photocurrent and total current as a function of voltage. (f) Solar conversion efficiency at optimum voltage, with equally spaced contours up to the max value of 0.018% for this example.

$w \backslash \hbar\omega_{max}$	(a) 1.1 eV	(b) 3 eV	(c) 4 eV	(d) 4 eV (77 K)	(e) 4 eV ($R_{elec} = 0$)
0 ($R_{elec} = 0$)	0.39 (0.74)	7.5 (1.1)	9.0 (1.2)	18 (0.82)	9.0 (1.2)
20 nm	0.0049 (0.75)	0.24 (0.97)	0.28 (1.0)	1.2 (0.44)	3.4 (1.0)
100 nm	0.00056 (0.78)	0.042 (1.0)	0.051 (1.0)	0.25 (0.44)	0.93 (0.95)

Table 5.1 – Maximum efficiency (%) of internal photoemission energy conversion devices for the solar spectrum integrated up to $\hbar\omega_{max}$ assuming complete absorption in a film of thickness w with the optimum Schottky barrier ϕ_b in eV given in parenthesis. The temperature is 300 K unless otherwise specified. The case $R_{elec} = 0$ assumes that all electrons encountering the interface with sufficient energy are collected (2π escape cone).

TiO_2 , or over the whole solar spectrum of about 4 eV. The illumination is assumed to be completely absorbed in a film of thickness w with a uniform generation profile across the film thickness ($\eta_e(z) = 1/w$, or for $w = 0$, $\eta_e(z) = \delta(z)$). Note that this level of absorption is unreasonably high (and violates detailed balance) but is used to demonstrate the efficiency limits, and recently broadband visible absorption of 70-80% has been demonstrated with plasmonic structures of thickness around 100 nm [143]. The device is assumed to be operating at room temperature or liquid nitrogen temperature with 1 sun illumination intensity. In the cases marked as $R_{elec} = 0$, which implies no escape cone restrictions, equation 5.11 was used with equation 5.10 and $\theta_{max} = \pi/2$; otherwise the yield considering phonon scattering and multiple carrier reflections from equation 5.12 was used. The absorber/emitter material was assumed to have free-electron-like bands with $E_f = 5.5$ eV as for Au with nondirect transitions so that the excitation energy distribution is as shown in Figure 5.2(a). For real devices, the true joint density of states and transition probability including direct transitions should be used especially in the ultraviolet, but this is a reasonable first approximation. As stated earlier, deleterious effects from hot hole emission, reverse hot carrier emission from the collector to the emitter, back-scattering in the collector, energy loss from phonon scattering, hot electron “surface recombination” [99], and carrier tunneling for a highly doped collector and thin barrier were not included. Additionally, any positive effects from hot carrier tunneling and hot electron multiplication from electron-electron scattering [144] were not included.

A few general conclusions can be drawn from the maximum efficiencies in Table 5.1. The energy conversion efficiency is overall low, primarily because high barriers are needed to avoid thermionic dark current. As a way to increase sub-bandgap absorption in existing devices using semiconductors such as Si or TiO₂, columns (a) and (b) reveal that the expected efficiency gains from integrating an internal photoemission component are much less than a percent if the standard model of internal photoemission used here is applicable. Decreasing the thickness can greatly help due to carrier reflections inside the material increasing the chances of emission, but in real devices the absorption will also decrease with very thin layers even considering plasmonic or optical cavity enhancement, though perhaps multilayers or nanoparticle dispersions [145, 146, 147] could regain high absorption. Comparing columns (c) and (d), it is clear that cooling the device gives appreciable gains in efficiency by allowing lower barriers which emphasizes the effect of thermionic current, but such cooling is difficult to envision in practice. Concentrating illumination would also help, but the possible corresponding increased temperature would be harmful. The only cases showing appreciable efficiency are where $R_{elec} = 0$ as in the last column (e) or first row, and thus ways are needed to avoid the escape-cone restriction which is based on a semiclassical quasiparticle momentum model. One way to increase yield even if the escape cone is applicable is if the hot carrier momentum can be preferentially directed normal to the interface, perhaps by photon polarization which was tested experimentally in Section 5.4.

The efficiencies presented here are somewhat lower than previous published calculations. Wang and Melosh [99] considered power conversion using Kretschmann coupling to surface plasmon polaritons in a symmetric metal-insulator-metal geometry corresponding to the diagonal line in Figure 5.4(f), where the maximum efficiency was calculated as 2.7%. Their calculation assumed no escape cone restriction, no carrier reflections, a uniform energy distribution of excited carriers, and an energy-independent $\lambda_{e-e} = 56$ nm, and the result is on the same order as that calculated here with no escape cone restriction (for which the justification is unclear). An older calculation by Schmidt et al. [148] postulated energy conversion efficiencies up to

10% even with the escape cone restriction; however, they neglected the thermionic dark current and used the barrier height as the operating voltage V in eqn. 5.16, which is not correct.

5.2.6 Geometrical considerations

The standard theory of either thermionic emission or photoemission is based on the concept of momentum normal to a planar interface, but on the nanoscale interfaces are not necessarily smooth, so the escape cone may not be quite as restrictive as considered above. Additionally, small particles with a high surface-area-to-volume ratio inherently allow emission from a range of angles even with a small escape cone; however, the enhancement due solely to the geometry of a sphere is only about a factor of 4 [149].

In vacuum photoemission studies, some anomalously high emission has indeed been observed for silver nanoparticles less than 10 nm diameter where the calculated yield only matches experiment if the escape cone restriction is completely relaxed [149, 150], but the enhanced yield depended strongly on the surface condition and did not occur for gold nanoparticles [151, 152]. Since the work function and dielectric function can vary with a nanoparticle's surface chemistry, the specific mechanism of enhancement seen in that experiment was difficult to identify.

5.2.7 Unique properties of plasmons

A plasmon can be described as a charge density fluctuation, and as such it can couple with single electron-hole excitations through the Coulombic fields resulting from decoherence in the collective electron gas oscillation [153, 154]. Surface plasmon polariton excitations can also re-emit photons in radiative damping, but here we are concerned with absorption only. A surface plasmon is thought to decay preferentially to electron-hole pairs which can fulfill the necessary momentum and energy conservation, though the short femtosecond-scale plasmon lifetime may allow excitation of multiple hot electrons due to energy uncertainty [155]. The decay time of plasmons

into hot electron excitations is on the order of 10 fs, and the hot electrons subsequently scatter off other electrons also within fs to slightly raise the temperature of the electron gas [156]. The electron gas then reaches thermal equilibrium with the lattice via phonon scattering within picoseconds [157, 158]. Though the plasmon and hot electron lifetimes are very short, the high Fermi velocity means that a hot electron can travel tens of nanometers before losing its energy. Since the surface plasmon excitation is a resonance, it can lead to high absorption in nanostructured geometries, especially if the optical resonance overlaps with a dark resonance with no dipole moment leading to a Fano lineshape that suppresses radiative decay [159, 144]. These considerations simply mean that surface plasmon resonances can increase absorption in a metal compared to the bulk case but do not otherwise comment on the yield of hot electron emission.

One might expect that the collective nature of the plasmon excitation would also mean that the decay occurs in a collective manner such that the energy gain of a given electron in a system of N electrons would be $\hbar\omega/N$, but theory and experiment have shown that the hot electron energy can be up to the photon energy. The phenomenon of photoemission in vacuum from surface plasmon decay was observed not long after the discovery and description of plasmon excitations [160, 161, 162, 153]. The effect was also seen for emission into electrolyte contacts on rough silver surfaces [163, 97, 164]. Recently it has been shown that the surface plasmon excitation, while involving many electrons, preserves the quantum information of the exciting photon [165], and as such it should excite single electron-hole pairs because of the lower probability of many-body collisions.

The surface plasmon resonance may also affect the hot electron emission yield beyond simply enhancing absorbance. In vacuum photoemission, a surface photoeffect is observed in which the probability of nondirect transitions is increased due to the presence strongly varying fields at a metal surface that can help contribute the required missing momentum [166, 167], and surface plasmon fields decay quickly away from the surface. Though photons in free space have low wavevector k , the high localized field confinement resulting from the surface plasmon allows high- k field components

that help relax the momentum conservation rule for electronic transitions. The surface photoeffect is most significant for p-polarized light with a component normal to a planar surface; this effect may therefore cause a correlation between the photon polarization and the hot electron emission yield. However, this effect proposed for vacuum photoemission is difficult to experimentally separate from other effects (such as surface plasmon resonances!) [129], and the situation may also change for internal photoemission into another material rather than vacuum.

Another interesting mechanism of enhancement may be carrier acceleration away from the emitter due to ponderomotive or quiver forces. The strong oscillating field gradients around a plasmonic particle can push charges of either sign away from the surface, and such effects have been seen near plasmonic nanostructures [168, 169, 170]. Here the fields would most strongly affect the hot electron after escape from the metallic emitter, so the effect should be small on the yield calculations performed here because we have already assumed unity probability of collection after escape. However, the ponderomotive effect may help avoid back-scattering of carriers in the collector, and any resulting enhancement would be correlated with photon polarization because the plasmonic fields are often highest along the photon polarization direction. A possible implementation to take full advantage of this force would involve a thin metal emitter near a plasmonic structure [170] rather than having both be the same structure.

Plasmonic structures can also create photocurrent or photovoltage due to the heating [171] or the photon drag effect [172, 173], but these effects are separate from the photoemission mechanism considered here.

5.2.8 Alternate sources of subgap photocurrent

5.2.8.1 Pseudo-internal photoemission

While a perfect and infinitely periodic semiconductor has no electronic states within the bandgap, real materials have defects and surfaces that create discrete states in the bandgap that give rise to subgap absorption. If this subgap absorption generates

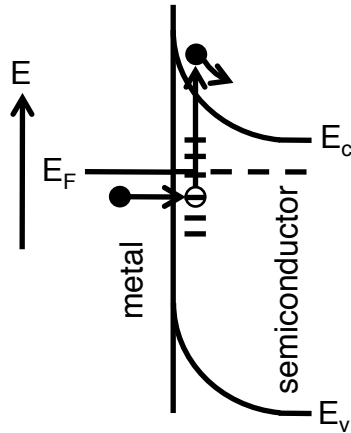


Figure 5.5 – Pseudo-internal photoemission band diagram.

a mobile, delocalized electron or hole, the resulting photocurrent termed “pseudo-internal photoemission” of carriers excited within the collector can be difficult to distinguish from the true internal photoemission of carriers excited within the emitter [141]. The excitation still occurs from states near the Fermi level, so the onset threshold will be similar. The spatial location of the subgap states should be near the emitter such that carriers can tunnel or otherwise transport for neutralization so that a steady-state current can exist. Even though the density of these defect or interface states may be low, the probability of collection can be much higher because no escape cone restriction exists. Additionally, the lifetime and mean free path may be longer in the collector because of reduced electron-electron scattering. A schematic of this process is shown in Figure 5.5.

The contribution from pseudo-internal photoemission can be especially high near a metallic surface or particle with a plasmon resonance because the local fields are greatly enhanced. In surface-enhanced Raman scattering, the electromagnetic field intensity at plasmonic hot spots can be enhanced by a factor of 10^5 [174], exponentially decaying away from the hot spot over tens of nm. If a large number of subgap localized states are near hot spots, the increased plasmonic fields will sensitize the subgap absorption.

In a well-characterized semiconductor such as silicon, the purity is sufficient so that the number of bulk midgap states should be negligible. Surface or interface

states can still contribute to a photocurrent, and a typical interface-state density for silicon is $D_{it} = 10^{12} \text{ cm}^{-2} \text{ eV}^{-1}$ with an optical excitation cross section around $\sigma_n(E) = 10^{-18} \text{ cm}^2$ [175, 176, 177, 178]. Assuming that the illumination does not change the state occupancy (fast tunneling), energy-independent D_{it} and σ_n , and equal chance of escape into either the metal emitter or the semiconductor collector, the pseudo-internal photoemission yield can be estimated as

$$\begin{aligned} Y_{pseudo}(\hbar\omega) &= \frac{1}{2} \int_{\phi_b}^{\hbar\omega} D_{it}(E_{el} - \hbar\omega) \sigma_n(E_{el}) dE_{el} \\ Y_{pseudo}(\hbar\omega) &\approx \frac{1}{2} (\hbar\omega - \phi_b) D_{it} \sigma_n \sim 10^{-7}. \end{aligned}$$

In comparison, the internal photoemission yield can be up to the order of 10^{-1} as in Figure 5.4(c) for an ideal case, and more typically is on the order of 10^{-3} when image force scattering and reflection losses exist in a real experiment [133]. Thus the full plasmonic field enhancement of 10^5 would need to be active over an entire surface to make Y_{pseudo} comparable to Y_{enh} for a pure, well-characterized semiconductor interface.

However, the case may be different for impure semiconductors such as metal oxides. A very rough estimate of the interface-state density could be calculated as one per surface atom distributed over the bandgap, $(10^{23} \text{ cm}^{-3})^{2/3} \text{ eV}^{-1} \approx 10^{15} \text{ cm}^{-2} \text{ eV}^{-1}$. In addition, significant absorption tails are often seen due to bulk subgap states as in TiO₂[179, 180, 181], though the estimated interfacial number of midgap trap states is still around 10^{12} cm^{-2} [182, 183]. A high density of subgap states could give rise to Y_{pseudo} comparable to Y_{enh} especially with plasmonic enhancement. Though many experiments have shown plasmonic enhancement of subgap absorption in TiO₂ which has been attributed to hot carrier emission [100, 184, 185, 186, 108, 187], the possibility of pseudo-internal photoemission should not be ruled out especially because in some cases the yields are higher than the maximum calculated by the above theory for Y_{enh} . For this reason we chose to use Si/metal interfaces to test plasmonic hot carrier emission rather than a more defective wide-bandgap oxide semiconductor.

5.2.8.2 Thermionic emission from temperature gradient

Any absorbed illumination will increase the temperature of the sample, and if a temperature gradient exists between the emitter and collector, a photocurrent resulting from thermionic emission will result even at zero applied bias. The maximum temperature increase at the surface of a heated sphere is given by [188]

$$\Delta T_{max} = \frac{P_{dis}}{4\pi k_t r}, \quad (5.17)$$

where P_{dis} is the optical power dissipated in the sphere into heat, k_t is the thermal conductivity of the surroundings, and r is the sphere radius. The increase in temperature can in turn increase the thermionic emission current from the emitter, $J_{TE} = A^*T^2e^{-\phi_b/(kT)}$ by the amount [141]

$$\frac{\partial J_{TE}}{\partial T} = A^*Te^{-\phi_b/(kT)} \left(2 + \frac{\phi_b}{kT} \right). \quad (5.18)$$

This thermionic emission current relative to the internal photoemission current can be significant for barriers less than about 0.4 eV even with a temperature differential as small as 10^{-4} K [134]. Note that ΔJ_{TE} is somewhat nonlinear with illumination intensity, though the deviation from linearity is small if the induced temperature change is less than a few Kelvin. However, for most of the cases considered here, the power dissipated in a single $r \sim 100$ nm nanoantenna is on the order 10^{-11} W resulting in a temperature increase of only 10^{-7} K, and the thermal contribution to the photocurrent should be negligible.

5.3 Numerical simulations

If the metal geometry supports a surface plasmon resonance, the absorption increases significantly and is easily calculated by the finite-difference time domain (FDTD) method. Here we simulate the absorption profile using Lumerical FDTD then import the spatial absorption into Mathematica to calculate the yield. The optical FDTD

simulation requires a fine mesh spacing of a few nm and careful interpolation where the Yee cell overlaps a metal-dielectric interface. For Au the dielectric function measured by Johnson and Christy [189] was used, and for Si and Ti the dielectric functions measured by Palik [190] were used. The results presented here were calculated using broadband simulations, but tests found that the same essential behavior resulted from single-wavelength simulations. The full 3D profile of absorbed power was reduced to just the distance away from a collecting interface; e.g., if the interface is along the z direction, the absorbed power was integrated along the x and y directions to give the probability of carrier generation η_e as a function of z only,

$$\eta_e(z) = \iint P_{abs}(x, y, z)/P_{inc} dx dy, \quad (5.19)$$

where P_{inc} is the incident power. This normalization will give the external quantum yield (EQY). To clarify notation, EQY denotes electrons collected per incident photon and is also known as external quantum efficiency (EQE) or incident photon collection efficiency (IPCE). The internal quantum yield (IQY) can be found by dividing by the absorption of the emitter structure, also known as the internal quantum efficiency (IQE) or absorbed photon collection efficiency (APCE). Additionally, sometimes the photocurrent is expressed as responsivity rather than yield, and the two are related by

$$\text{Responsivity (nA/mW)} = \frac{Y}{\hbar\omega} \times 10^6.$$

To validate the calculations made above, the yield was calculated for various specific cases of plasmonic hot carrier emission shown in the literature and modeled here in Lumerical, and the results are presented in Table 5.2. Here equations 5.12 and 5.19 were used at zero voltage (short circuit) which include the escape cone restriction and the enhancement of phonon scattering and carrier reflections but no correlation of hot electron momentum with polarization. The energy of illumination was chosen to match the experimental conditions and the strongest resonance of the plasmonic structures, and the barrier height was taken from the values mentioned in the references except for the Au/Ti/TiO₂ antenna for which the value of a Ti/TiO₂

Structure	$\hbar\omega$ (eV)	Absorption (%)	ϕ_b (eV)	EQY (calc.)	EQY (exp.)
20 nm Ag on Al ₂ O ₃	4.7	42.7	3.9	4.5×10^{-4}	1×10^{-4} [139]
Au/Al ₂ O ₃ /Au SPP	1.96	62.5	1.4	1.8×10^{-3} (net)	3×10^{-8} [99]
Au/Ti/Si antenna	0.92	15.3	0.5	3.8×10^{-3}	1×10^{-5} [98]
Au/Ti/TiO ₂ antenna	1.1	14.2	0.2	1.2×10^{-2}	8×10^{-2} [100]

Table 5.2 – External quantum yield examples for various internal photoemission geometries. (1) 20 nm Ag film on Al₂O₃ illuminated at normal incidence; (2) 30 nm Au/4 nm Al₂O₃/35 nm Au films on glass illuminated at 45.8 ° from glass side on SPP resonance; (3) 28 nm Au/2 nm Ti antenna, 110×50 nm on Si illuminated at normal incidence on LSP resonance polarized along long axis; (4) 38 nm Au/2 nm Ti antenna, 200×100 nm on TiO₂ illuminated at normal incidence on LSP resonance polarized along long axis.

barrier was used [191].

For the simple case of a Ag metal film on an Al₂O₃/Al collector, the magnitude of calculated EQY agrees well with experiment, and better agreement would result if hot hole emission and back emission from the collector were included [139]. The absorption in a thin film can be very high in the case of Kretschmann coupling to a propagating surface plasmon polariton (SPP) which was exploited in the metal-insulator-metal device realized with Al/Al₂O₃/Au by Wang and Melosh [99]. The hot electron emission of both Au films was calculated, and the result shown is the net EQY which is much higher than the low experimental value, probably due to imperfections in fabrication. Two examples of Au dipole antennas supporting localized surface plasmons (LSP) are shown. The Au/Ti/Si antenna by Knight and Halas [98] was all solid-state, and the experimental EQY is smaller than that calculated here, again perhaps due to diode imperfections. The only case for which the experimental value was higher than our calculation is for an Au/Ti/TiO₂ antenna by Nishijima and Hisawa [100] with an electrochemical contact, but the possibility of pseudo-internal photoemission from the TiO₂ or thermal effects from a small barrier and chemical kinetics also may have increased the EQY. Additionally, the absorption on resonance was calculated here as 14.2% whereas the measured value was reported as 70% which

would bring the experiment and calculated EQY closer together.

Overall the experimental demonstrations of hot electron emission either from standard photon absorption or from surface plasmon decay show lower EQY values than the values predicted from the three-step internal photoemission model. Therefore, the solar energy conversion efficiency values from Table 5.1 can be regarded as upper limits. Additionally, the standard model including the escape cone restriction and the assumption of an isotropic momentum distribution of hot carriers resulting from plasmon decay is a reasonable description of the results in the literature so far.

5.4 Experiment: Is yield correlated with polarization?

Though the yield of internal photoemission is rather low due to both the finite probability of exciting a hot carrier to an energy below the barrier and the quasiparticle momentum requirement normal to the interface described by the small escape cone in Figure 5.1, the possibility of either energy conversion devices or photon detectors can have appreciable efficiency or responsivity if the escape cone restriction is relaxed as in the case $R_{elec} = 0$ in Table 5.1. Additionally, the efficiency could perhaps be boosted by picking metals with a favorable density of states perhaps with d-bands at a level favorable to hot hole emission into a solid-state or chemical collector [115, 116, 108] to manipulate $P_0(E_{el})$. Though the escape cone restriction may be relaxed somewhat by interface roughness or interface chemistry, experimental yields for the most part agree with the Fowler yield magnitude including the momentum restriction.

Even if the escape cone is small, the yield could still be high if the hot carrier momentum could be directed normal to the interface, i.e., into the escape cone. A localized surface plasmon resonance can be simply described as the resonant oscillation of the “jellium” electron cloud about the fixed ion cores due to the forcing of the photon electric field, so the collective electron motion is in a well-defined direction set by the photon polarization. The nonradiative plasmon damping can occur by

random dephasing of the collective electron gas motion into a hot electron-hole pair [155] with the surface plasmon energy $\hbar\omega_{sp}$, and one might assume that the hot electron momentum would also be correlated with the photon polarization. In this case, the correct choice of plasmonic emitter geometry supporting a resonance polarized normal to a collecting interface would increase the yield as described previously in equation 5.13.

5.4.1 Reproducing dipole antenna response

The nanostructure geometry will of course affect the coupling strength and absorption for different photon polarizations, and an initial experiment was done with Au/Ti dipole antennas on Si shown in Figure 5.6 to duplicate the experiment of Knight and Halas [98] and show this polarization dependence. $120 \times 120 \mu\text{m}^2$ arrays of $100 \times 40 \text{ nm}$ gold rods spaced by 250 nm in each direction were patterned by electron-beam lithography with polymethylmethacrylate (PMMA) on a n-type (100) Si wafer of resistivity 1-10 $\Omega\text{-cm}$. The wafer had a 50 nm dry thermal oxide grown before patterning, and the oxide was etched away with a 40 second dip in 12:1 H_2O :Buffered Oxide Etch (BOE) solution to expose the bare silicon surface under each antenna right before electron-beam evaporation and liftoff. The antennas were 20 nm thick, with 2 nm Ti and 18 nm Au. In the SEM, the medium-grey region is the SiO_2 film, and the dark circles around the antennas are exposed Si regions from the HF dip. A top contact to the Au was formed by sputtering 90 nm of indium tin oxide at room temperature, and the ITO was contacted by wire bonding with Al wire. The silicon wafer was contacted on the back side with indium-gallium eutectic.

A schematic of the sample measurement setup is shown in Figure 5.7. Samples were illuminated with monochromated light from a 4W Fianium supercontinuum laser chopped at 25 Hz and fiber-coupled into a WiTec microscope. A double-side polished Si wafer was placed in the beam path to eliminate any visible light. The laser spot at the sample was about 70 microns in diameter, and the power was 1-5 μW . A linear polarizing film was placed directly above the $20 \times 0.4\text{NA}$ objective and

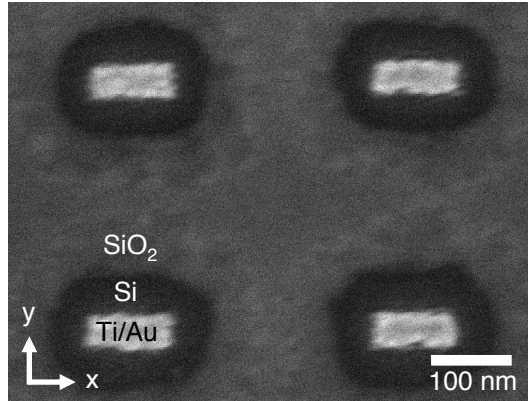


Figure 5.6 – SEM image of Au dipole antennas on Si. This top view shows the wells in the SiO_2 and metal plasmonic antennas.

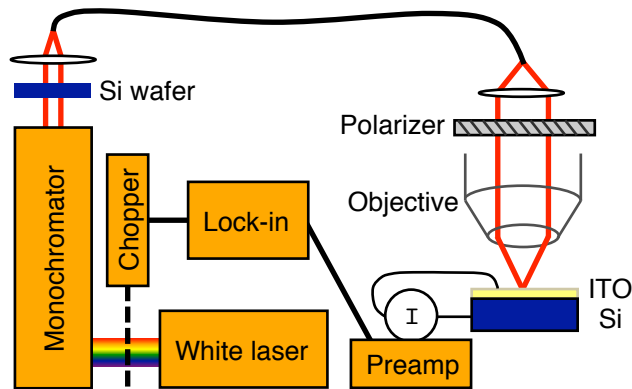


Figure 5.7 – Measurement apparatus schematic for testing responsivity. The sample was mounted in a ceramic chip carrier that is not shown.

rotated to polarize light either along the antenna long dimension (the x -direction) or short dimension. The illumination power at the sample position was measured with a calibrated Thorlabs FDG05 Ge photodiode for each polarization before testing the samples, and a separate power detector was used to monitor the laser beam to ensure that the illumination power was not changing over the course of the measurement. The photocurrent was measured with a Stanford Research Systems SR570 preamp and SR830 lock-in amplifier at zero applied bias.

The photocurrent responsivity of the dipole antennas is shown in Figure 5.6. As expected, light polarized along the long axis of the plasmonic antennas is more strongly absorbed at the antenna resonance between 1400-1500 nm, and more hot carriers are generated causing the peak in responsivity. On the other hand, light

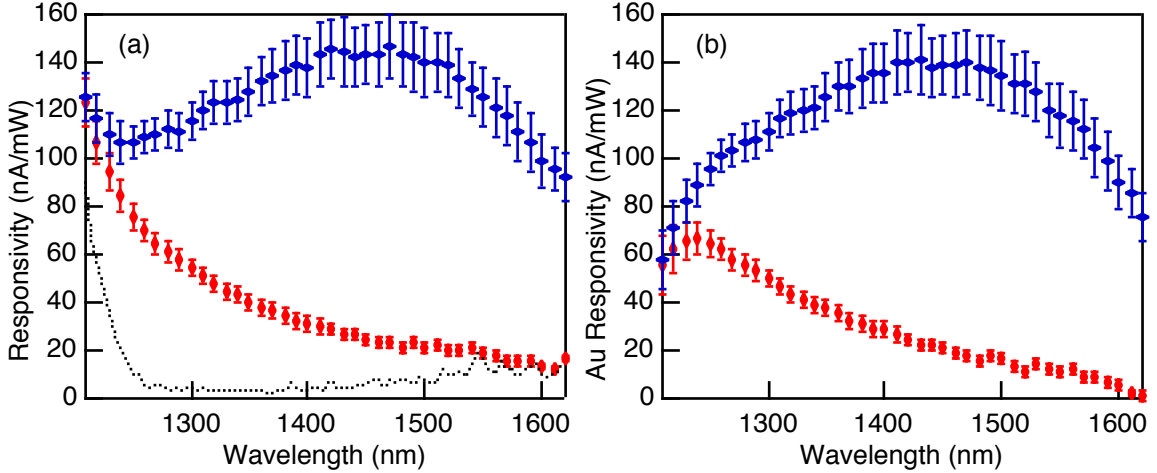


Figure 5.8 – Responsivity of Au dipole antennas. Blue horizontal diamonds show x-polarized light along the antenna long axis, and red vertical diamonds show y-polarized light. (a) Raw data including the background photoresponse (black dotted line) from an area with no Au; (b) background response subtracted to show just current from Au. Error bars reflect the roughly 10% variation in power measurement.

polarized along the short axis is not in resonance, and the IPE yield (and hence responsivity) shows just the expected Fowler behavior proportional to λ^{-2} near the onset and no peak. The samples showed a background current when illuminated away from the patterns for wavelengths below 1250 nm, possibly from band tail absorption in the silicon, so in Figure 5.8(b) the background has been subtracted to show the response from hot carrier injection from the gold. The error in the measurement was primarily from a 10% relative variation in the polarizer transmission and reproducibility of the power incident on the sample when changing polarizer positions. Additionally, due to the absorption in the gold, the background subtraction can lead to an inflection near 1250 nm unrelated to the plasmon peaks; later data is presented without this background subtraction since it is better judged by eye. The responsivities shown here are consistent with the results in [98], though the magnitude is about 20 \times higher than the previous data. In this geometry, the collecting interface plane is parallel to either polarization direction, so the changes in yield with polarization are due to increased coupling to the antenna rather than any correlation between photon polarization and hot electron momentum direction; a different experiment is needed to test that correlation.

5.4.2 Angled illumination to add p-polarization

An attempt was made to design an experiment in which the angle of illumination would change, thus varying the s- (x,y) and p- (z) polarization of incident light on a structure that could support spectrally overlapping resonances both parallel and perpendicular to the interface. For example, a cube in free space supports dipolar resonances along all three axes, and the fields inside are primarily aligned to the polarization vector of the incoming photons. In the FDTD simulations the full fields are spatially calculated, and the power absorbed due to various field directions can be separated based on a more detailed version of eqn. 5.3,

$$P_{abs,x} + P_{abs,y} + P_{abs,z} = -\frac{1}{2}\omega\text{Im}[\epsilon] (|E_x|^2 + |E_y|^2 + |E_z|^2). \quad (5.20)$$

For the example of a cube in free space, FDTD simulations showed that the absorbed power due to the different field components largely matched with the photon electric field components. However, with a high-index dielectric substrate included on one side of the cube as would be the case in the experiment, the asymmetry caused absorption due to field components other than just the field components of the incident light. The phase differences at the interface and presence of sharp corners allowed scattering of the incident light into the strongest modes of the structure, and the relationship between the photon's electric field and the induced fields inside the metal was weakened. Even for varied side dimensions of a rounded rectangular structure, no suitable geometry was found here that would allow simply changing the incident angle to test the correlation between field direction and hot electron momentum direction.

5.4.3 Buried antenna geometry

Instead, an analogue to the previously fabricated dipole antenna was chosen for this experiment in which the collecting interface was placed at the antenna end instead of at the bottom interface by burying the antenna in a Si trench, with a unit cell geometry shown schematically in Figure 5.9 that supported a similar resonance for

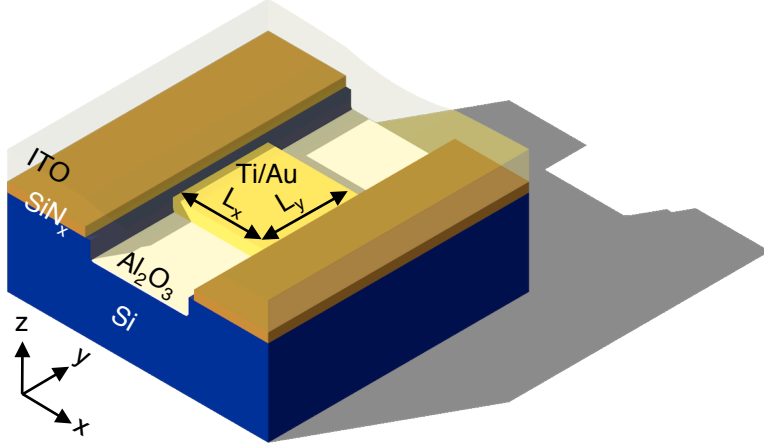


Figure 5.9 – Buried antenna schematic geometry.

both x-polarized and y-polarized light. A thin layer of Al_2O_3 was placed under the Ti/Au rectangle to act as an insulator between the metal emitter and Si collector so that hot carriers could only be injected in the x-direction; a silicon nitride layer was used as an insulator between most of the ITO and Si. Rather than an elongated rectangle as in Figure 5.6, the plasmonic antennas were approximately squares that still supported dipolar resonances in the x- and y-directions, but the collecting interface was normal to the x-direction. The energies of the x- and y- resonances were determined primarily by the dimensions of the Au square, but the Si in the x-direction weakened and broadened the x-resonance so that the power absorbed at the peak was approximately halved for the same resonance energy.

An example broadband FDTD simulation of the power absorption is shown in Figure 5.10 for a plasmonic buried rounded-square antenna of side dimension 175 nm. The absorption shown in Figure 5.10(a) peaks for both polarizations around 1440 nm wavelength, and the field profiles in the insets show that this mode is dipole-like with field nodes at the edges of the square. For the rounded-square antenna, the internal fields largely match the incident field polarization, though for y-polarized light some small scattering into E_x and E_z fields occurs. The fields are concentrated near the edges, so the hot electron generation profile $\eta_e(x)$ appears very different for x- and y-polarized light as seen in Figure 5.10(b). The sharp features are effects from the finite (2 nm) mesh size in FDTD at either the Au or Ti edges but only slightly af-

fect the general behavior. In Figure 5.10(c), the collecting interface is assumed to be only on the left side of the buried square, and the hot electron generation profile was used together with eqn. 5.12 or eqns. 5.13 and 5.14 (where z is replaced with x , and without integrating along x) to determine the expected internal photoemission yield for either the case of isotropic hot electron momentum or the case of hot electron momentum being fully determined by the field direction. The full yield is found by integrating along x : for isotropic hot electron momentum, the yields for x - and y -polarized light are 2.23×10^{-4} and 5.49×10^{-4} , respectively; for polarization and momentum correlation, the yield works out to be 2.02×10^{-3} for both polarizations. Therefore, if momentum is isotropic the yield largely follows the magnitude of absorption which is stronger for y -polarized light, whereas if momentum and polarization are correlated the yield for x -polarized light is increased to be equal to the yield for y -polarized light. Other simulation geometries showed that the x -polarized yield could actually be greater than the y -polarized yield for momentum-polarization correlation, overcoming the difference in absorption.

5.4.4 Buried antenna fabrication and responsivity

The buried plasmonic antenna geometry was considerably more difficult to fabricate than the standard dipole antennas shown in Figure 5.6, but good results were achieved with a combination of nanoimprint and electron-beam lithography with various wet and dry etches. A 53 nm layer of silicon nitride was deposited by plasma-enhanced chemical vapor deposition on clean n-Si wafers of resistivity 1-10 $\Omega\text{-cm}$. A set of grooves were patterned in the y -direction by nanoimprint lithography in which a 140 nm silicon oxide sol-gel was spun on the wafers and stamped by hand with a polydimethylsiloxane (PDMS) stamp with the desired grating pattern in $500 \times 500 \mu\text{m}^2$ arrays [192]. The PDMS stamp was made with a double layer PDMS cast on a silicon wafer that had been patterned by electron-beam lithography and reactive ion etching (RIE). After stamping, the samples were allowed to cure for an hour after which the PDMS stamp was peeled off. Grooves were etched into the SiN_x/Si with an

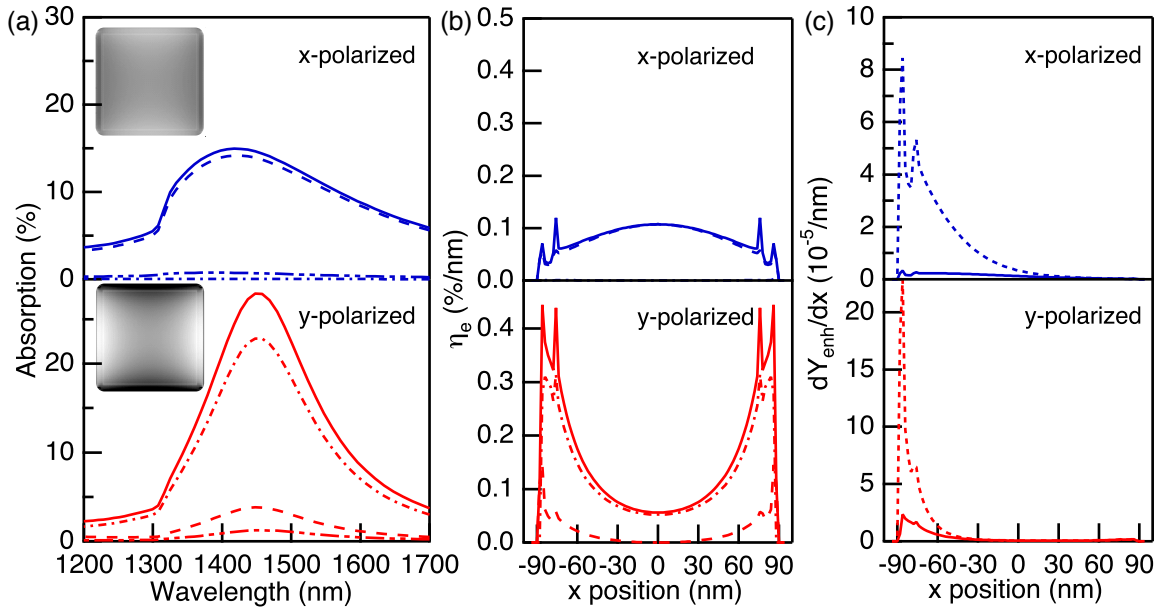


Figure 5.10 – Simulations of absorption and yield for buried square antenna of side dimension 175 nm for both x-polarized and y-polarized normally incident light. (a) Total absorption (solid line) as well as components due to E_x , E_y , and E_z (dash, dash-dot, and dash-dot-dot lines, respectively). Insets show x-y profile of $|E|^2$ integrated along z with the same intensity scale. (b) Hot electron generation profile as a function of x at 1440 nm illumination from integrating $|E|^2$ along y and z , with different field components shown as in (a). (c) Partial IPE yield as a function of x at 1440 nm illumination considering isotropic hot electron momentum (solid line) or correlated momentum and polarization (dotted line) where the collecting interface is on the left.

RIE etch following the “pseudo-Bosch” recipe [193] consisting of a SF₆ etch gas and C₄F₈ passivating agent tuned to achieve smooth, vertical sidewalls; after this etch, the samples were briefly oxygen plasma cleaned to remove any fluoropolymer layer. 12 nm of Al₂O₃ was deposited in the trench bottoms by normal incidence electron-beam evaporation. Next a 200 nm PMMA layer was spun over the patterns, and 100×100 μm² arrays of horizontal stripes in the x-direction were patterned by electron-beam lithography, roughly aligned to the previous grooves. Before metal deposition, the samples were dipped in 120:1 H₂O:BOE for 8 seconds to remove the native oxide from the sidewalls but leave the Al₂O₃ and sol-gel silicon oxide intact. The samples were immediately loaded into a vacuum chamber to electron-beam evaporate 2 nm of Ti and 30 nm of Au at either normal incidence or 5-10° off-normal angle to ensure contact of the metal with a trench sidewall. The metal was lifted off with a 1-2 hour soak in Remover PG heated to 60 °C and a brief sonication in isopropyl alcohol (IPA). The remaining silicon oxide and top parts of the metal stripes were removed with a 25 second dip in 60:1 H₂O:BOE and brief sonication in H₂O followed by drying in a nitrogen stream. Some representative SEM images of these buried plasmonic antennas are shown in Figure 5.11. Top contact was formed as before with 90 nm of sputtered ITO wire-bonded to a ceramic chip carrier, and the silicon was contacted with indium-gallium eutectic.

Samples with the metal deposited at normal incidence showed no internal photoemission response from the metal because a slight gap existed between the metal and the silicon groove sidewall seen in Figure 5.11(a) due to the electron-beam evaporation processing. This provided a useful control to ensure that the Al₂O₃ layer performed as designed to eliminate any contact between the metal and the trench bottom. In contrast, with the metal deposited at a slight angle to the sidewall as in Figure 5.11(b-e), a clear IPE current resulted with a plasmonic peak similar to the previous dipole antenna case. For samples with the metal deposited at an angle, a metal tab was present on one side of the buried square antenna, but FDTD simulations indicated that the overall behavior was similar to that shown in Figure 5.10 for a rounded square with somewhat more scattering into field polarizations not aligned

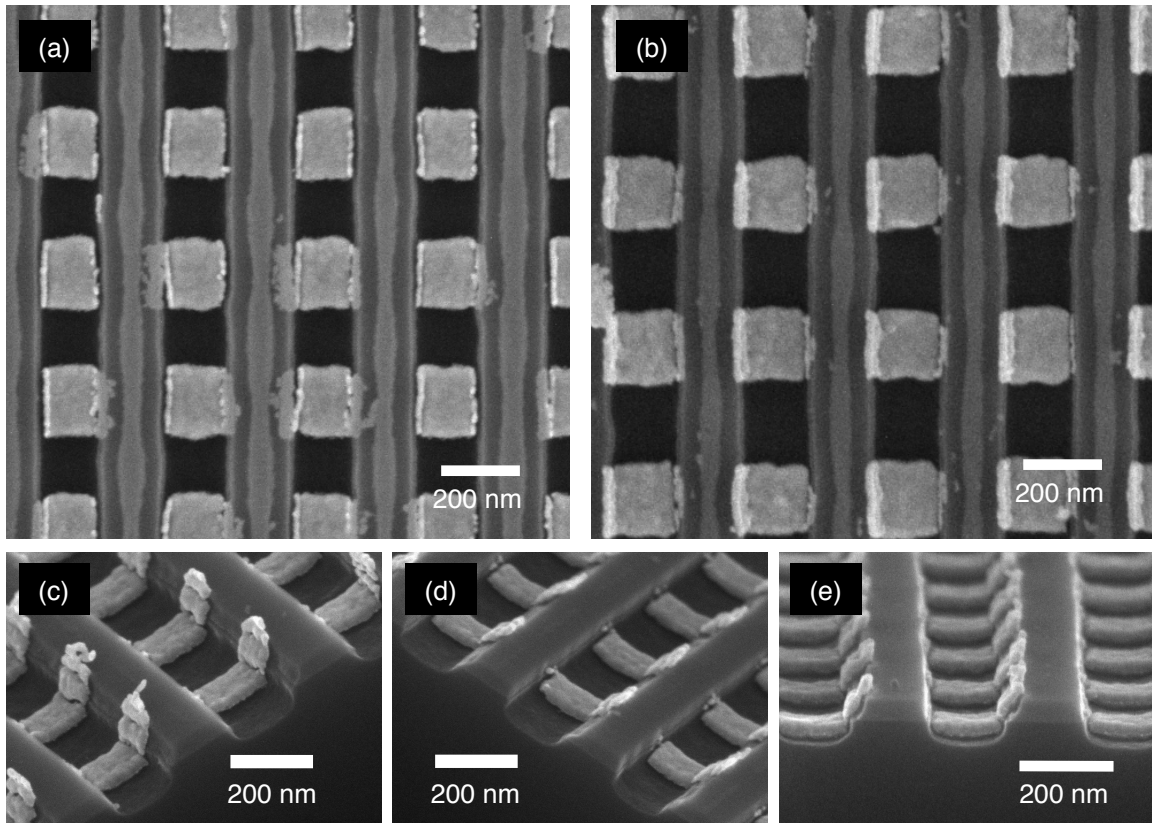


Figure 5.11 – SEM images of buried antenna arrays. (a) Top view of sample with metal deposited at normal incidence, (b) top view of sample with metal deposited at 7° off normal, (c-e) various angle views of a cross section of an angled deposition sample. In (a) and (b) some sol-gel silica remains as narrow vertical stripes.

with the incident polarization.

The responsivity (or the related EQY) was measured for both x- and y-polarized light where the collecting interface plane is normal to the x-direction. Some results for various values of buried antenna side dimensions L_x and L_y are shown in Figure 5.12. The experimental responsivity for light of both polarizations is shown as well as the simulated response based on FDTD simulations coupled with the yield calculations considering an isotropic momentum distribution with no polarization/momentum correlation. The agreement between the magnitude of the experimental and calculated responsivity is remarkable; the calculated values are roughly only $5\times$ higher than the experimental values. For all geometries tested, the yield was higher for y-polarized light because of the stronger coupling and sharper resonance in the y-direction, and any increased yield from preferential x-momentum from x-polarized light was not visible. Figure 5.12(a) shows the response for an array with a large wavelength separation between the x- and y-resonances, and the plasmon peak is very clearly seen for y-polarized light; however, this geometry is not optimal to compare the two polarizations. Figure 5.12(b-d) shows the results for arrays with geometries with overlapping plasmon peaks for both x- and y-polarized light, and slight peaks are seen in the experimental data resulting from the plasmon resonance. Due to the imperfect nature of the fabrication, there may be a background response and broadening from some Ti/Au features that are not perfectly rounded rectangles as the simulations assume, so direct comparison between the experimental magnitude and simulated magnitude is difficult. However, no evidence was found to support correlation between the hot electron momentum and the photon/plasmon field polarization.

Though the microscopic view of a plasmon resonance as an oscillation of the electron gas around the fixed positive ion cores is a useful picture, it can be taken too far as an intuitive view, and it does not necessarily mean that hot electrons will be ejected along the direction of polarization upon plasmon decay. The plasmon is an oscillation of the Fermi energy surface in k-space, so this means that electron states with wavevectors distributed all around k-space are involved, and the decay is unlikely to excite only electrons that originally had momentum along the field polarization.

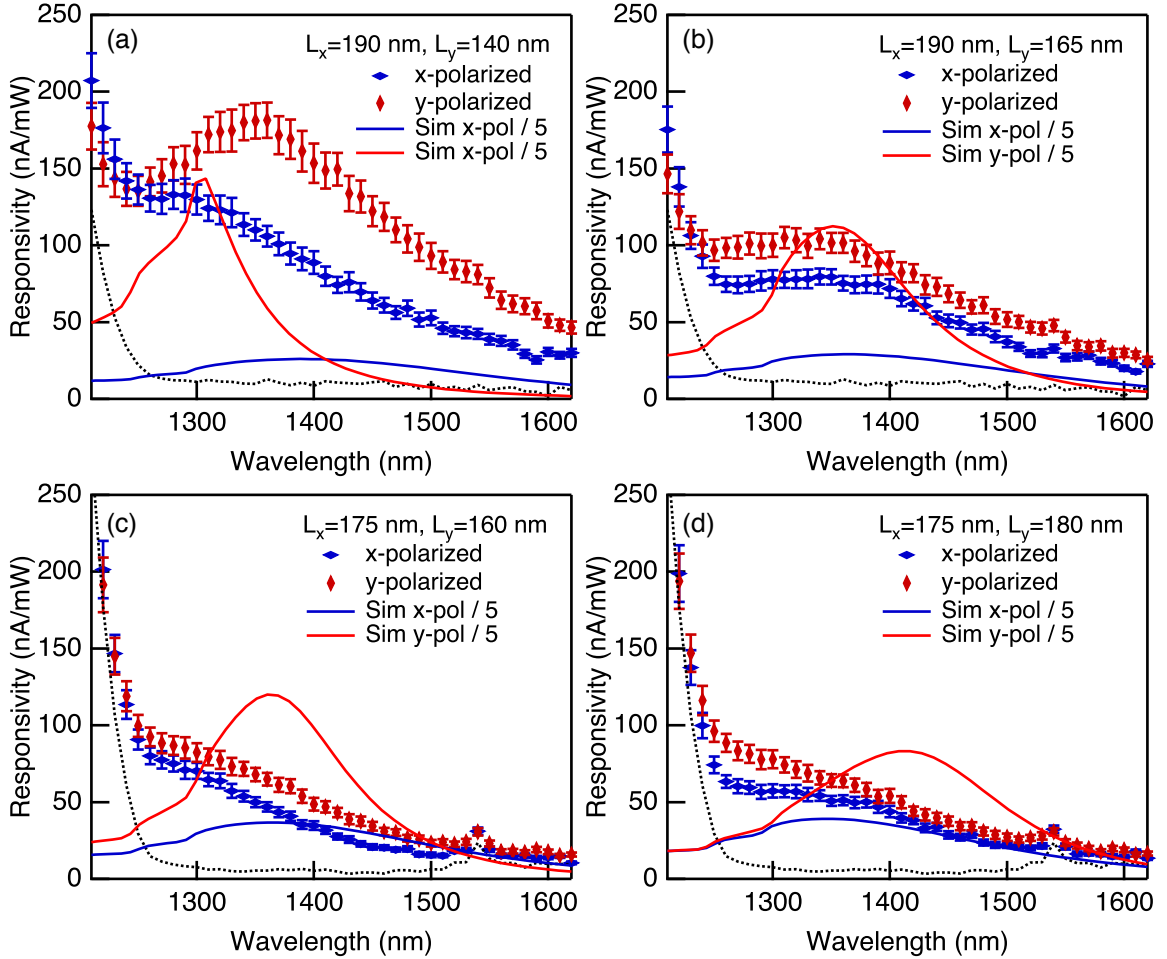


Figure 5.12 – Responsivity for buried antennas with various side dimensions. Experimental results shown as diamonds with error bars resulting from polarizer transmission variations, and simulated response shown as solid lines reduced by a factor of 5. The background photocurrent for an illuminated area adjacent to the antenna arrays is shown as black dotted lines.

The transitions involved for infrared photon energies are necessarily nondirect for Au, so some source of momentum is involved in any case that may also reduce any hot electron momentum-polarization correlation. Even if the photon or plasmon does impart some momentum determined by its polarization, the excited electron originally could have been traveling in any direction and thus could be traveling in any direction after excitation as well with a slightly perturbed momentum because the Fermi wavevector is large compared to photon wavevectors. The peculiarities of the collective nature of a plasmon excitation may change the situation somewhat with the high field confinement resulting in larger plasmon wavevectors, but the detailed quantum treatment of the photon/plasmon/hot electron interactions are beyond the scope of this thesis.

5.4.5 The role of the titanium

The optical response of these Ti/Au antennas is dominated by the geometry and dielectric function of the gold, but the role of the titanium adhesion layer should not be dismissed. In the experiments performed here, the 2 nm Ti layer was essential to see significant photocurrent response and a plasmon peak. The thin Ti acted to lower the Schottky barrier height as seen in the current-voltage curves in Figure 5.13 for planar film Schottky diodes fabricated with similar processing as the buried antenna devices. With no Ti present, the diode showed excellent behavior with an ideality factor near 1 and a barrier height of 0.78 eV consistent with the literature value of 0.8 eV for Au/Si; with the Ti adhesion layer, the ideality factor was around 1.5 and the barrier height 0.57 eV was consistent with the literature value of 0.63 eV [92]. The lower barrier resulted in stronger photocurrent response as expected from the basic Fowler behavior of internal photoemission where the yield is small for photons of energy near the barrier energy. In addition to lowering the barrier, the absorption is higher in the Ti layer and hot electrons are more likely to be generated in the Ti. However, due to the long mean free path of hot electrons near E_f , the spatial location of hot electron generation in these antennas is not a dominating factor. On the other

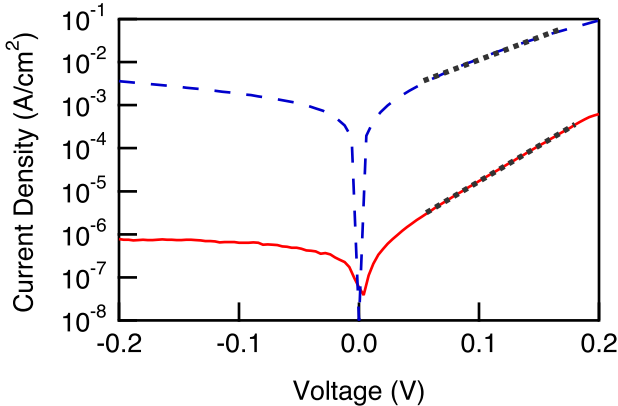


Figure 5.13 – Current-voltage behavior of Au/Ti/Si (blue dashed line) and Au/Si diodes (red solid line). Black dotted linear fits were used to determine the diode ideality factors and barrier heights.

hand, the higher dissipation in the Ti could possibly be used with more complicated geometries to increase the yield for a very thin film of Ti sensitized by a nearby Au antenna.

5.5 Summary

It is possible to absorb and collect light with energy below the bandgap energy of a semiconductor using internal photoemission from metal/semiconductor contacts, and the external quantum yield of photons to collected electrons can be increased by coupling into metallic plasmon resonances which allows increased absorption. The collective plasmon excitation can decay into hot electron-hole pairs, and experiments both here and in the literature show clear plasmonic internal photoemission photocurrents.

Photovoltaic or photoelectrochemical solar energy conversion devices would benefit greatly if sub-bandgap light could be harvested, and here a model was developed for the energy conversion efficiency of internal photoemission devices. Unfortunately, even with various best-case scenarios and values, the energy conversion efficiency of devices based on hot-carrier emission from metals is low due to (1) dark thermionic reverse current in forward bias, (2) the distribution of hot electron energies ranging

from zero up to the photon energy, and (3) the small escape cone considering momentum normal to the interface. While the thermionic emission currents could be lowered by cooling and the distribution of hot electron energy could be modified by choice of absorbing metal joint density of states, the small escape cone is an assumed restriction in the semiclassical model for internal photoemission.

The hot electron or hole quasiparticle momentum must be normal to the interface to be emitted, but the escape cone is somewhat larger for rough or chemically modified interfaces. Even if the escape cone is small, it would be less restrictive if the hot carrier momentum could be preferentially directed normal to the interface rather than the traditionally assumed isotropic momentum distribution, so an experiment was designed where the collecting interface was one side of a buried plasmonic antenna for which the polarization could be directed either parallel or perpendicular to the interface. If polarization was correlated with hot electron momentum, the photocurrent responsivity would have been higher for normally polarized light or at least equal for both polarizations. However, the experiment showed the opposite because the absorption was higher for polarization parallel to the interface, and no evidence was seen for correlation between hot electron momentum and plasmon polarization. The experiment was compared to electromagnetic simulations coupled to yield calculations, and good agreement was found between the traditional theory and the experimental results both in magnitude and spectral shape.

The situation is better for detectors which can be cooled and operated in reverse bias, and efficient spectrally selective devices could be made utilizing plasmonics. Near-infrared detectors have already been commercialized based on Schottky-barrier photoemission due to the ease of array formation and integration with traditional silicon CMOS processing, and plasmon enhancement could be well utilized in this field.

Chapter 6

Summary and outlook

In this thesis, various aspects of solar energy conversion to chemical fuels via semiconductor devices were studied. Following the path of the photogenerated charge carriers, I will summarize this thesis from back to front. The collection of photons with energy below a semiconductor bandgap was accomplished via plasmon-enhanced internal photoemission of hot electrons, and the mechanism of hot carrier emission from a metal Schottky barrier was determined to be the most likely explanation for the experimental data. The semiclassical model of internal photoemission yield with an isotropic momentum distribution of hot carriers was applied to plasmonic structures, and the experimental yield was consistent with the model. For buried antenna devices fabricated here, the polarization dependence followed the simulated resonance strength rather than showing a correlation between plasmon field polarization and hot electron momentum. With the model thus verified, the low calculated solar energy conversion efficiencies for internal photoemission devices are likely to even be optimistic values.

For an electron-hole pair excited in a semiconductor, the minority charge carrier wanders around the solid until either recombining or reaching a collecting interface, and this minority carrier diffusion length was measured using a novel wedge technique with back-side scanned illumination. The method worked for both solid-state and electrochemical devices, but the tungsten oxide photoanode thin-film wedges required some treatment to insulate the porosity that resulted from high-temperature deposition or annealing. Sputtered tungsten oxide had a diffusion length of 0.5-1 μm

which was consistent with previously reported values. The wedge technique provides a complementary measurement of diffusion length; it is likely that a traditional spectral response measurement that does not require fabrication of a wedge would provide a quicker measurement though with perhaps more uncertainty.

After encountering a collecting junction, the minority carriers are swept to the surface where they can either react with a chemical species (e.g., split water) or transfer to a catalyst before reaction. Two techniques were developed to image the efficiency of the water-splitting reaction over an electrode surface, one that looked at the product bubbles and one that looked at the reactant concentration profile as pH via a fluorescent indicator. Both techniques were able to quantitatively measure the local reaction rate on a well-controlled surface with a resolution of tens of microns, and the fluorescent indicator avoided the complications arising from the presence of a bubble. Though these measurements were performed *in situ*, the experimental conditions were somewhat different than the operating conditions of a complete solar fuel device which will probably run at broad illumination and pH 0 or 14. These techniques required focused illumination for bubble imaging and near-neutral pH for fluorescence mapping.

Future directions

- Considering bubble evolution, there is research to be done about the effects of bubbles on nanostructured and microstructured electrodes. While imaging bubbles turned out to be nonideal for examining the microscopic local reaction rate at an electrode, the phenomenon of bubble nucleation and growth may eventually dictate the type of surface morphologies permissible for a solar fuel device, for at 10 mA/cm^2 the bubble coverage is reasonably large. A question of interest is whether a structured surface is detrimental because all the crevices fill up with gas or if it is beneficial because it allows many bubble nucleation sites as on a boiling stone. It would also be useful to quantify the effects of surfactants at the highly acidic and basic pH values both on the bubble break-off diameter

and the electrochemistry.

- The fluorescent pH imaging would be most useful if it operated at either acidic or basic pH values, for the modeling would be more straightforward and quantitative if only one oxidation/reduction reaction were dominant. Therefore, other indicator dyes rather than BCECF would be worth trying as suggested above, including oxygen sensor dyes that are quenched in the presence of oxygen. Instead of a flow cell, the speed of the laser-scanning confocal microscope would allow time-resolved imaging of the diffusion fields which could be modeled similarly to the steady-state examples shown here. A major advantage of the confocal fluorescent imaging technique is the ability to build up 3D images, for other techniques to image activity such as scanning electrochemical microscopy are optimized for a flat surface. For example, the pH profile in a silicon water-splitting microwire array could be imaged and compared to finite element simulations of the diffusion limitations. Apart from microscopic imaging, fluorescent indication of pH could also be useful for validating models of water-splitting devices attempting to operate at near-neutral pH to determine the extent of the pH gradients that develop over time.
- Diffusion length measurements with the wedge technique are ready to extend to other materials. For materials that can be sputtered, identical procedures to those used here should give good results. Extensions of the sample preparation would involve further tests of polishing films into wedges using the tripod polishing mount with different pads and slurries to figure out a general recipe to easily create polished wedges. Even apart from wedges, the technique should also work on a set of samples of varying (constant) thickness as long as sample-to-sample variation is minimized. On the experimental setup, the UV LED was sufficient here to prove the principle, but a shorter wavelength laser would be more useful, and the ability to try a few different strongly absorbed wavelengths would confirm that the absorption length is short enough. Also, further modeling of the expected photocurrent response on porous electrodes would be useful,

especially on materials like bismuth vanadate that show higher photocurrent for back illumination than front illumination. Last, setting up the cell to work with nonaqueous electrolytes with very positive or negative potential redox couples should allow a junction to be formed with either p- or n-type semiconductors.

- Utilization of plasmon decay in hot carrier emission is still interesting even though thermionic emission dark current is a detriment for solid-state energy conversion strategies. Emission into an irreversible electrochemical reaction could store the hot electron energy as a sort of energy-selective electrochemical contact. The existence of such an effect should be tested with an easily detectable chemical change such as electrochemiluminescence or combined with surface-enhanced Raman scattering. If the effect is seen with an irreversible reaction, then electron emission into a more reversible reaction such as CO₂ reduction would be interesting to test. In the solid-state area, plasmonic IR detectors could be further optimized by clever tricks of metal layers. For example, the plasmonic dipole antennas in Figure 5.6 could be made with a thin insulating layer between the Ti and the Au antenna which may increase the yield because more absorption occurs in the Ti than the Au, and the very thin 2 nm layer would have a good “thinness” enhancement. Similarly, instead of Ti, a noble metal silicide could be the emitter with a low barrier for hot hole emission as is the case for commercial Schottky IR detectors. Antenna geometries different than the simple bar dipole antenna would enable different shapes of the response spectra. On a fundamental level, a quantum mechanical model that describes photon / plasmon / hot electron / phonon interactions would be useful to help identify the likely hot electron momentum direction for a given polarization.

Apart from just the topics discussed in this thesis, one other idea is worth mentioning here for coupling plasmonics/photonics with photoelectrochemistry. The tandem water-splitting device would be easiest to manufacture if the photoanode and photocathode could sit side-by-side, but that typically means that the energy conversion

efficiency is also halved. However, spectral splitting strategies such as 3D volume holograms or even simple dichroic mirrors may work very well for a solar fuels device. For photovoltaics, the efficiency of stacked multi-junction devices beats spectrum splitting, but in water splitting the plumbing and chemical engineering advantages of avoiding stacked photoanode and photocathode assemblies make spectrum splitting worth a look for photoelectrochemical cells.

Appendix A

Steady-state solution to Poisson's equation for Gaussian source

For a laser incident on a semiconductor surface with a Gaussian intensity profile, $I = I_0 \exp(-r^2/r_{laser}^2)$, both the heat rise in the solid and the diffusion of photogenerated species at the surface can be described by Poisson's equation. An analytic solution to the problem of the temperature rise in a solid when illuminated with a laser was given by Lax [48] considering the steady-state heat equation,

$$\nabla T = -\frac{G_{therm}}{K} = -\frac{I_0}{K} \alpha e^{-\alpha z} e^{-r^2/r_{laser}^2}, \quad (\text{A.1})$$

where G_{therm} is the energy absorbed per unit volume per sec and the sign convention for z is that more positive values move away from the surface. Assuming that no heat is transferred at the surface and that all the heat is generated in an infinitesimal surface layer (essentially if the absorption depth is much smaller than the beam width), the solution obtained is

$$\Delta T(r, z) = \Delta T_{max} N(r, z), \quad (\text{A.2})$$

with

$$\Delta T_{max} = \frac{P_{laser}}{2\sqrt{\pi} K r_{laser}} \quad (\text{A.3})$$

and

$$N(r, z) \xrightarrow{\alpha \rightarrow \infty} \pi \int_0^\infty J_0(\beta r / r_{laser}) \exp(-\beta z) \exp(-\beta^2/4) d\beta. \quad (\text{A.4})$$

Here $P_{laser} = I_0 \pi r_{laser}^2$ and J_0 is the Bessel function of the first kind of order 0.

Using the comparison between heat flow and particle diffusion, this solution can be extended to solve the profile of dissolved gas generated in a Gaussian profile at an electrode. The steady-state diffusion equation including gas generation is

$$\nabla^2 c = -\frac{G_{gas}}{D}, \quad (\text{A.5})$$

where c is the concentration, G_{gas} is the generation rate, and D is the diffusion coefficient. For sake of comparison (recognizing that in the final solution we will take $\alpha \rightarrow \infty$ because all the gas is generated at the electrode surface), the generation of gas can be written as

$$G_{gas} = \frac{P_{laser} \lambda \Phi}{hc \pi r_{laser}^2 Z} \alpha e^{-\alpha z} e^{-r^2/r_{laser}^2}. \quad (\text{A.6})$$

Here we have assumed that all the absorbed photons under a given spot generate charge carriers that then contribute to the gas generation based on the observed quantum yield. In analogy to the solution for heat flow, the dissolved product profile is then given by

$$c(r, z) = c_{max} N(r, z), \quad (\text{A.7})$$

$$c_{max} = \frac{P_{laser} \lambda \Phi}{2\sqrt{\pi} h c r_{laser} Z D}. \quad (\text{A.8})$$

Note that this solution is in steady state, so it represents the highest concentration of dissolved gas for any time.

Appendix B

Mathematica code for diffusion length calculations

The one-dimensional model of photocurrent as described in Chapter 4 was implemented in Mathematica 6 to allow convenient analysis of various limiting cases. The basic code is included below for reference.

```

Ce=α/(1-α^2L^2);
A=Ce*((S2-αL) (1-S1) Exp[-α W] + (S1 + α L) (1 + S2) Exp[W/L])/((1 - S1) (1 - S2) Exp[-W/L] - (1 + S1) (1 + S2) Exp[W/L]));
B=α/(1-α^2 L^2)*((S2-α L) (1 + S1) Exp[-α W] + (S1 + α L) (1 - S2) Exp[-W/L])/((1 - S1) (1 - S2) Exp[-W/L] - (1 + S1) (1 + S2) Exp[W/L]));
deltan[x_,α_,L_,W_,S1_,S2_]:=A*Exp[-x/L]+B*Exp[x/L]+Ce*Exp[-α x];
Jdifffrontill[α_,L_,W_,S1_,S2_,xd_]:=Exp[-α*xd]*L^2 D[deltan[xpr,α,L,W-xd,S1,S2],xpr]/.{xpr->0};
Jdiffbackill[α_,L_,W_,S1_,S2_,xd_]:=-L^2 D[deltan[xpr,α,L,W-xd,S1,S2],xpr]/.{xpr->(W-xd)};
Jdriftfrontill[α_,xd_]:=Integrate[α*Exp[-α*x],{x,0,xd}];
Jdriftbackill[[Alpha],xd_]:=Integrate[α Exp[-α x],{x,W-xd,W}];
Jfrontill[α_,L_,W_,S1_,S2_,xd_]:=Piecewise[{ {Jdifffrontill[α,L,W,S1,S2,xd] + Jdriftfrontill[α,xd],W>xd}, {Jdriftfrontill[α,W],W<=xd} }];
Jbackill[α_,L_,W_,S1_,S2_,xd_]:=Piecewise[{ {Jdiffbackill[α,L,W,S1,S2,xd] + Jdriftbackill[α*xd],W>xd}, {Jdriftbackill[α,W],W<=xd} }];
Leffwedge[α_,L_,W_,S1_,S2_,xd_]:=Jbackill[α,L,W,S1,S2,xd]/D[Jbackill[α,L,Wpr,S1,S2,xd],Wpr]/.{Wpr->W};
Manipulate[GraphicsColumn[{LogPlot[Jbackill[1/absLength,diffusionLength,sampleWidth,Sback,10^3,depletionWidth],{sampleWidth,1,4000},PlotRange->All,FrameLabel->{"Thickness","Current (arb)"},Frame->True,Axes->False,PlotStyle->{Thick}],Plot[{Leffwedge[1/absLength,diffusionLength,sampleWidth,Sback,10^3,depletionWidth]/diffusionLength,1},{sampleWidth,1,4000},PlotRange->{0,2},FrameLabel->{"Thickness","LeffWedge/L"},Frame->True,Axes->False,PlotStyle->{Thick,Dashed}],{{diffusionLength,300},1,2000,Appearance->"Labeled"},{{absLength,100},1,2000,Appearance->"Labeled"},{{Sback,5},0,1000,Appearance->"Labeled"},{{depletionWidth,50},0,2000,Appearance->"Labeled"},FrameLabel->"Wedge photocurrent for back (contact) Illumination"],LeffSR[α_,L_,W_,S1_,S2_,xd_-]:=-1/α+(1/Jfrontill[α,L,W,S1,S2,xd])/D[1/Jfrontill[1/abslength,L,W,S1,S2,xd],abslength]/.{abslength->1/α};
Manipulate[GraphicsColumn[{Plot[1/Jfrontill[1/absLength,diffusionLength,sampleThickness,10^3,Sback,depletionWidth],{absLength,1,2000},PlotRange->All,FrameLabel->{"Absorption Length","1/Current (arb)"},Frame->True,Axes->False,PlotStyle->{Thick}],Plot[{LeffSR[1/absLength,diffusionLength,sampleThickness,10^3,Sback,depletionWidth],1},{absLength,1,2000},PlotRange->{0,2},FrameLabel->{"Absorption Length","LeffSR"},Frame->True,Axes->False,PlotStyle->{Thick,Dashed}],{{diffusionLength,300},1,2000,Appearance->"Labeled"},{{sampleThickness,1500},1,2000,Appearance->"Labeled"},{{Sback,5},0,1000,Appearance->"Labeled"},{{depletionWidth,50},0,2000,Appearance->"Labeled"},FrameLabel->"Spectral Response for Front (liquid) Illumination"]

```

Bibliography

- [1] Mouhot, J.-F. Past connections and present similarities in slave ownership and fossil fuel usage. *Climatic Change* **105**, 329–355 (2010).
- [2] Sandel, M. J. (ed.) *Justice: A Reader* (Oxford University Press, 2007).
- [3] Chu, S. & Majumdar, A. Opportunities and challenges for a sustainable energy future. *Nature* **488**, 294–303 (2012).
- [4] Hermann, W. Quantifying global exergy resources. *Energy* **31**, 1685–1702 (2006).
- [5] International Energy Outlook 2011 (2011). URL [http://www.eia.gov/forecasts/ieo/pdf/0484\(2011\).pdf](http://www.eia.gov/forecasts/ieo/pdf/0484(2011).pdf).
- [6] Lewis, N. S. & Nocera, D. G. Powering the planet: Chemical challenges in solar energy utilization. *Proc. Nat. Acad. Sci.* **103**, 15729–15735 (2006).
- [7] Blankenship, R. E. et al. Comparing Photosynthetic and Photovoltaic Efficiencies and Recognizing the Potential for Improvement. *Science* **332**, 805–809 (2011).
- [8] World Energy Outlook 2012 (2012). URL <http://iea.org/publications/freepublications/publication/>.
- [9] Bernstein, L. et al. Climate change 2007: synthesis report. Summary for policymakers (2007). URL <http://www.ipcc.ch/pdf/assessment-report/ar4/syr/>.
- [10] Spurgeon, J. M. *Wire Array Solar Cells: Fabrication and Photoelectrochemical Studies*. Ph.D. thesis, California Institute of Technology (2010).
- [11] Q2 2012 Clean Energy Policy and Market Briefing (2012). URL <http://www.bnef.com/>.

- [12] \$1/W Photovoltaic Systems (2010). URL <http://www1.eere.energy.gov/solar/sunshot/pdfs/>.
- [13] Green, M. A., Emery, K., Hishikawa, Y., Warta, W. & Dunlop, E. D. Solar cell efficiency tables (version 40). *Prog. Photovolt: Res. Appl.* **20**, 606–614 (2012).
- [14] Polman, A. & Atwater, H. A. Photonic design principles for ultrahigh-efficiency photovoltaics. *Nat. Mater.* **11**, 174–177 (2012).
- [15] Green, M. A. *Third Generation Photovoltaics: Advanced Solar Energy Conversion*. Springer Series in Photonics (Springer-Verlag, 2003).
- [16] Romero, M. & Steinfeld, A. Concentrating solar thermal power and thermochemical fuels. *Energy Environ. Sci.* **5**, 9234 (2012).
- [17] Khaselev, O. & Turner, J. A monolithic photovoltaic-photoelectrochemical device for hydrogen production via water splitting. *Science* **280**, 425–427 (1998).
- [18] Saur, G. Wind-To-Hydrogen Project: Electrolyzer Capital Cost Study. Tech. Rep. NREL/TP-550-44103 (2008).
- [19] James, B. D., Baum, G. N., Perez, J. & Baum, K. N. Technoeconomic Analysis of Photoelectrochemical (PEC) Hydrogen Production. Tech. Rep., Directed Technologies (2009).
- [20] Heller, A. Conversion of sunlight into electrical power and photoassisted electrolysis of water in photoelectrochemical cells. *Acc. Chem. Res.* **14**, 154–162 (1981).
- [21] Gerischer, H. *Photoelectrochemistry, Photocatalysis, and Photoreactors: Fundamentals and Developments* (Reidel, Dordrecht, The Netherlands, 1985).
- [22] Tan, M. X. et al. Principles and Applications of Semiconductor Photoelectrochemistry. *Prog. Inorg. Chem.* **41**, 21–144 (1994).
- [23] Fujishima, A. Electrochemical photolysis of water at a semiconductor electrode. *Nature* **238**, 37–38 (1972).
- [24] Bolton, J., Strickler, S. & Connolly, J. Limiting and Realizable Efficiencies of Solar Photolysis of Water. *Nature* **316**, 495–500 (1985).

- [25] Walter, M. G. et al. Solar Water Splitting Cells. *Chem. Rev.* **110**, 6446–6473 (2010).
- [26] Chen, S. & Wang, L.-W. Thermodynamic Oxidation and Reduction Potentials of Photocatalytic Semiconductors in Aqueous Solution. *Chem. Mater.* **24**, 3659–3666 (2012).
- [27] Harriman, A., Pickering, I. J., Thomas, J. M. & Christensen, P. A. Metal oxides as heterogeneous catalysts for oxygen evolution under photochemical conditions. *J. Chem. Soc., Faraday Trans. 1* **84**, 2795–2806 (1988).
- [28] Jaramillo, T. F. et al. Identification of active edge sites for electrochemical H₂ evolution from MoS₂ nanocatalysts. *Science* **317**, 100–102 (2007).
- [29] Bard, A. J. & Mirkin, M. V. (eds.) *Scanning Electrochemical Microscopy* (Marcel Dekker, Inc., New York, 2001).
- [30] Sivula, K., Le Formal, F. & Grätzel, M. Solar Water Splitting: Progress Using Hematite Photoelectrodes. *ChemSusChem* **4**, 432–449 (2011).
- [31] Nowotny, J., Sorrell, C., Sheppard, L. & Bak, T. Solar-hydrogen: environmentally safe fuel for the future. *Int. J. Hydrot. Energy* **30**, 521–544 (2005).
- [32] Bak, T., Nowotny, J., Rekas, M. & Sorrell, C. Photo-electrochemical hydrogen generation from water using solar energy. Materials-related aspects. *Int. J. Hydrot. Energy* **27**, 991–1022 (2002).
- [33] Kogo, K., Yoneyama, H. & Tamura, H. Photocatalytic Oxidation of Cyanide on Platinized TiO₂. *J. Phys. Chem.* **84**, 1705–1710 (1980).
- [34] Kraeutler, B. & Bard, A. Heterogeneous Photocatalytic Preparation of Supported Catalysts - Photodeposition of Platinum on TiO₂ Powder and Other Substrates. *J. Am. Chem. Soc.* **100**, 4317–4318 (1978).
- [35] Santato, C., Ulmann, M. & Augustynski, J. Photoelectrochemical properties of nanostructured tungsten trioxide films. *J. Phys. Chem. B* **105**, 936–940 (2001).
- [36] McShane, C. M. & Choi, K.-S. Photocurrent Enhancement of n-Type Cu₂O Electrodes Achieved by Controlling Dendritic Branching Growth. *J. Am. Chem. Soc.* **131**, 2561–2569 (2009).

- [37] Kanan, M. W. & Nocera, D. G. In situ formation of an oxygen-evolving catalyst in neutral water containing phosphate and Co²⁺. *Science* **321**, 1072–1075 (2008).
- [38] Lee, J., Ye, H., Pan, S. & Bard, A. J. Screening of photocatalysts by scanning electrochemical microscopy. *Anal. Chem.* **80**, 7445–7450 (2008).
- [39] Cohen, M. I. & Blunt, R. F. Optical Properties of SrTiO₃ in the Region of the Absorption Edge. *Phys. Rev.* **168**, 929–933 (1968).
- [40] Butler, M. A. & Ginley, D. S. Prediction of Flatband Potentials at Semiconductor-electrolyte Interfaces from Atomic Electronegativities. *J. Electrochem. Soc.* **125**, 228–232 (1978).
- [41] Bocarsly, A. B., Bolts, J. M., Cummins, P. G. & Wrighton, M. S. Photoelectrolysis of water at high-current density - use of UV laser excitation. *Appl. Phys. Lett.* **31**, 568–570 (1977).
- [42] Wrighton, M. S. et al. Strontium-titanate Photoelectrodes - Efficient Photoassisted Electrolysis of Water At Zero Applied Potential. *J. Am. Chem. Soc.* **98**, 2774–2779 (1976).
- [43] Leenheer, A. J. & Atwater, H. A. Water-Splitting Photoelectrolysis Reaction Rate via Microscopic Imaging of Evolved Oxygen Bubbles. *J. Electrochem. Soc.* **157**, B1290–B1294 (2010).
- [44] Lide, D. R. (ed.) *CRC Handbook of Chemistry and Physics* (CRC Press/Taylor and Francis, Boca Raton, FL, 2009).
- [45] Blander, M. & Katz, J. L. Bubble Nucleation in Liquids. *AiChE J.* **21**, 833–848 (1975).
- [46] Vogt, H., Aras, O. & Balzer, R. The limits of the analogy between boiling and gas evolution at electrodes. *Int. J. Heat Mass Tran.* **47**, 787–795 (2004).
- [47] Wagner, F. & Somorjai, G. Photocatalytic and Photoelectrochemical Hydrogen Production on Strontium Titanate Single Crystals. *J. Am. Chem. Soc.* **102**, 5494–5502 (1980).

- [48] Lax, M. Temperature Rise Induced by a Laser Beam. *J. Appl. Phys.* **48**, 3919–3924 (1977).
- [49] Jones, S., Evans, G. & Galvin, K. Bubble nucleation from gas cavities - a review. *Adv. Colloid Interfac.* **80**, 27–50 (1999).
- [50] Lubetkin, S. The motion of electrolytic gas bubbles near electrodes. *Electrochim. Acta* **48**, 357–375 (2002).
- [51] Vogt, H. Interfacial Supersaturation at Gas Evolving Electrodes. *J. Appl. Electrochem.* **23**, 1323–1325 (1993).
- [52] Brandon, N. P. & Kelsall, G. H. Growth kinetics of bubbles electrogenerated at microelectrodes. *J. Appl. Electrochem.* **15**, 475–484 (1985).
- [53] Darby, R. & Haque, M. S. The dynamics of electrolytic hydrogen bubble evolution. *Chem. Eng. Sci.* **28**, 1129–1138 (1973).
- [54] Yu, C., Scullin, M. L., Huijben, M., Ramesh, R. & Majumdar, A. Thermal conductivity reduction in oxygen-deficient strontium titanates. *Appl. Phys. Lett.* **92**, 191911 (2008).
- [55] Vogt, H. & Balzer, R. The bubble coverage of gas-evolving electrodes in stagnant electrolytes. *Electrochim. Acta* **50**, 2073–2079 (2005).
- [56] Grigoriev, S., Porembsky, V. & Fateev, V. Pure hydrogen production by PEM electrolysis for hydrogen energy. *Int. J. Hydrol. Energy* **31**, 171–175 (2006).
- [57] Yang, Y.-F. & Denuault, G. Scanning electrochemical microscopy (SECM) study of pH changes at Pt electrode surfaces in Na₂SO₄ solution (pH 4) under potential cycling conditions. *J. Chem. Soc. Faraday T.* **92**, 3791 (1996).
- [58] Etienne, M., Dierkes, P., Erichsen, T., Schuhmann, W. & Fritsch, I. Constant-Distance Mode Scanning Potentiometry. High Resolution pH Measurements in Three-Dimensions. *Electroanalysis* **19**, 318–323 (2007).
- [59] Horrocks, B. et al. Scanning electrochemical microscopy. 19. Ion-selective potentiometric microscopy. *Anal. Chem.* **65**, 1213–1224 (1993).

- [60] Klimov, A. & Pollack, G. H. Visualization of charge-carrier propagation in water. *Langmuir* **23**, 11890–11895 (2007).
- [61] Cabrera, C., Finlayson, B. & Yager, P. Formation of natural pH gradients in a microfluidic device under flow conditions: Model and experimental validation. *Anal. Chem.* **73**, 658–666 (2001).
- [62] Loete, F., Vuillemin, B., Oltra, R., Chaumont, D. & Bourillot, E. Application of total internal reflexion fluorescence microscopy for studying pH changes in an occluded electrochemical cell: Development of a waveguide sensor. *Electrochim. Commun.* **8**, 1016–1020 (2006).
- [63] Vitt, J. & Engstrom, R. Imaging of oxygen evolution and oxide formation using quinine fluorescence. *Anal. Chem.* **69**, 1070–1076 (1997).
- [64] Chen, G., Delafuente, D., Sarangapani, S. & Mallouk, T. Combinatorial discovery of bifunctional oxygen reduction - water oxidation electrocatalysts for regenerative fuel cells. *Catal. Today* **67**, 341–355 (2001).
- [65] Reddington, E. et al. Combinatorial electrochemistry: A highly parallel, optical screening method for discovery of better electrocatalysts. *Science* **280**, 1735–1737 (1998).
- [66] Rudd, N. et al. Fluorescence confocal laser scanning microscopy as a probe of pH gradients in electrode reactions and surface activity. *Anal. Chem.* **77**, 6205–6217 (2005).
- [67] Fiedler, S. et al. Diffusional Electrotitration: Generation of pH Gradients over Arrays of Ultramicroelectrodes Detected by Fluorescence. *Anal. Chem.* **67**, 820–828 (1995).
- [68] Grime, J., Edwards, M., Rudd, N. & Unwin, P. Quantitative visualization of passive transport across bilayer lipid membranes. *Proc. Nat. Acad. Sci.* **105**, 14277 (2008).
- [69] Bitziou, E., Rudd, N. C., Edwards, M. A. & Unwin, P. R. Visualization and Modeling of the Hydrodynamics of an Impinging Microjet. *Anal. Chem.* **78**, 1435–1443 (2006).
- [70] Engstrom, R. C., Ghaffari, S. & Qu, H. Fluorescence imaging of electrode-solution interfacial processes. *Anal. Chem.* **64**, 2525–2529 (1992).

- [71] Sjoback, R., Nygren, J. & Kubista, M. Absorption and fluorescence properties of fluorescein. *Spectrochim. Acta A* **51**, L7–L21 (1995).
- [72] Boens, N. et al. Photophysics of the fluorescent pH indicator BCECF. *J. Phys. Chem. A* **110**, 9334–9343 (2006).
- [73] Tsien, R. & Waggoner, A. Fluorophores for Confocal Microscopy: Photophysics and Photochemistry. In Pawley, J. B. (ed.) *Handbook of Biological Confocal Microscopy* (Plenum Press, New York, 1995).
- [74] Grynkiewicz, G., Poenie, M. & Tsien, R. A New Generation of Ca-2+ Indicators with Greatly Improved Fluorescence Properties. *J. Biol. Chem.* **260**, 3440–3450 (1985).
- [75] Leenheer, A. J. & Atwater, H. Imaging Water-Splitting Electrocatalysts with pH-Sensing Confocal Fluorescence Microscopy. *J. Electrochem. Soc.* **159**, H752–H757 (2012).
- [76] Xu, W., Kong, J. S., Yeh, Y.-T. E. & Chen, P. Single-molecule nanocatalysis reveals heterogeneous reaction pathways and catalytic dynamics. *Nat. Mater.* **7**, 992–996 (2008).
- [77] Nørskov, J. K. et al. Trends in the Exchange Current for Hydrogen Evolution. *J. Electrochem. Soc.* **152**, J23–J26 (2005).
- [78] Matthews, S. et al. Quantitative kinetic analysis in a microfluidic device using frequency-domain fluorescence lifetime imaging. *Anal. Chem.* **79**, 4101–4109 (2007).
- [79] Cannan, S., Macklam, I. & Unwin, P. Three-dimensional imaging of proton gradients at microelectrode surfaces using confocal laser scanning microscopy. *Electrochim. Commun.* **4**, 886–892 (2002).
- [80] Sun, W.-C., Gee, K. R., Klaubert, D. H. & Haugland, R. P. Synthesis of Fluorinated Fluoresceins. *J. Org. Chem.* **62**, 6469–6475 (1997).
- [81] Demas, J., Degraff, B. & Coleman, P. Oxygen sensors based on luminescence quenching. *Anal. Chem.* **71**, 793A–800A (1999).

- [82] Orton, J. W. & Blood, P. *The Electrical Characterization of Semiconductors: Measurement of Minority Carrier Properties.* Techniques of Physics (Academic Press, London, 1990).
- [83] Schroder, D. K. *Semiconductor Material and Device Characterization* (John Wiley & Sons, Ltd, Hoboken, New Jersey, 2006), 3 edn.
- [84] Gartner, W. W. Depletion-Layer Photoeffects in Semiconductors. *Phys. Rev.* **116**, 84–87 (1959).
- [85] Siklitsky, V. & Tolmatchev, A. New Semiconductor Materials. Characteristics and Properties (2012). URL <http://www.ioffe.ru/SVA/NSM/>.
- [86] Butler, M. A. Photoelectrolysis and Physical-Properties of Semiconducting Electrode WO₃. *J. Appl. Phys.* **48**, 1914–1920 (1977).
- [87] Chen, X. et al. Enhanced incident photon-to-electron conversion efficiency of tungsten trioxide photoanodes based on 3D-photonic crystal design. *ACS Nano* **5**, 4310–4318 (2011).
- [88] Wang, G. et al. Hydrogen-Treated WO₃ Nanoflakes Shown Enhanced Photostability. *Energy Environ. Sci.* **5**, 6180–6187 (2012).
- [89] Baeck, S. H., Jaramillo, T., Stucky, G. D. & McFarland, E. W. Controlled Electrodeposition of Nanoparticulate Tungsten Oxide. *Nano Lett.* **2**, 831–834 (2002).
- [90] Marsen, B., Cole, B. & Miller, E. L. Influence of sputter oxygen partial pressure on photoelectrochemical performance of tungsten oxide films. *Sol. Energ. Mat. Sol. Cells* **91**, 1954–1958 (2007).
- [91] Vidyarthi, V. S. et al. Enhanced photoelectrochemical properties of WO₃ thin films fabricated by reactive magnetron sputtering. *Int. J. Hydrg. Energy* **36**, 4724–4731 (2011).
- [92] Sze, S. M. & Ng, K. K. *Physics of Semiconductor Devices* (John Wiley & Sons, Inc., Hoboken, 2007), 3 edn.

- [93] Wang, H., Lindgren, T., He, J., Hagfeldt, A. & Lindquist, S.-E. Photolelectrochemistry of Nanostructured WO₃ Thin Film Electrodes for Water Oxidation: Mechanism of Electron Transport. *J. Phys. Chem. B* **104**, 5686–5696 (2000).
- [94] Aspnes, D. E. & Studna, A. A. Dielectric functions and optical parameters of Si, Ge, GaP, GaAs, GaSb, InP, InAs, and InSb from 1.5 to 6.0 ev. *Phys. Rev. B* **27**, 985 (1983).
- [95] Thomann, I. et al. Plasmon enhanced solar-to-fuel energy conversion. *Nano Lett.* **11**, 3440–3446 (2011).
- [96] Solarska, R., Królikowska, A. & Augustynski, J. Silver Nanoparticle Induced Photocurrent Enhancement at WO₃ Photoanodes. *Ang. Chem. Int. Ed.* **49**, 7980–7983 (2010).
- [97] Neff, H., Sass, J. K. & Lewerenz, H. J. A photoemission-into-electrolyte study of surface plasmon excitation on high index faces of silver. *Surf. Sci.* **143**, L356–L362 (1984).
- [98] Knight, M. W., Sobhani, H., Nordlander, P. & Halas, N. J. Photodetection with Active Optical Antennas. *Science* **332**, 702–704 (2011).
- [99] Wang, F. & Melosh, N. A. Plasmonic Energy Collection through Hot Carrier Extraction. *Nano Lett.* **11**, 5426–5430 (2011).
- [100] Nishijima, Y., Ueno, K., Yokota, Y., Murakoshi, K. & Misawa, H. Plasmon-Assisted Photocurrent Generation from Visible to Near-Infrared Wavelength Using a Au-Nanorods/TiO₂ Electrode. *J. Phys. Chem. Lett.* **1**, 2031–2036 (2010).
- [101] Lee, Y. K. et al. Surface Plasmon-Driven Hot Electron Flow Probed with Metal-Semiconductor Nanodiodes. *Nano Lett.* **11**, 4251–4255 (2011).
- [102] Khurjin, J. B. & Boltasseva, A. Reflecting upon the losses in plasmonics and metamaterials. *MRS Bull.* **37**, 768–779 (2012).
- [103] Hartland, G. V. Optical Studies of Dynamics in Noble Metal Nanostructures. *Chem. Rev.* **111**, 3858–3887 (2011).

- [104] Koval, C. A. & Segar, P. R. Mechanistic aspects of reductions by hot electrons in p-indium phosphide/acetonitrile photoelectrochemical cells. *J. Phys. Chem.* **94**, 2033–2039 (1990).
- [105] Groner, M. D., Watts, D. K. & Koval, C. A. Further investigation of the reduction of alkyl bromides at p-InP photocathodes - Hot or thermalized electrons? *J. Electrochem. Soc.* **144**, 1690–1696 (1997).
- [106] Peterson, A. A., Abild-Pedersen, F., Studt, F., Rossmeisl, J. & Nørskov, J. K. How copper catalyzes the electroreduction of carbon dioxide into hydrocarbon fuels. *Energy Environ. Sci.* **3**, 1311 (2010).
- [107] Warren, S. C. & Thimsen, E. Plasmonic solar water splitting. *Energy Environ. Sci.* **5**, 5133–5146 (2011).
- [108] Tian, Y. & Tatsuma, T. Mechanisms and Applications of Plasmon-Induced Charge Separation at TiO₂ Films Loaded with Gold Nanoparticles. *J. Am. Chem. Soc.* **127**, 7632–7637 (2005).
- [109] Thimsen, E., Le Formal, F., Grätzel, M. & Warren, S. C. Influence of plasmonic Au nanoparticles on the photoactivity of Fe₂O₃ electrodes for water splitting. *Nano Lett.* **11**, 35–43 (2010).
- [110] Takai, A. & Kamat, P. V. Capture, Store, and Discharge. Shuttling Photogenerated Electrons across TiO₂–Silver Interface. *ACS Nano* **5**, 7369–7376 (2011).
- [111] Hung, W. H., Aykol, M., Valley, D., Hou, W. & Cronin, S. B. Plasmon resonant enhancement of carbon monoxide catalysis. *Nano Lett.* **10**, 1314–1318 (2010).
- [112] Liu, Z., Hou, W., Pavaskar, P., Aykol, M. & Cronin, S. B. Plasmon Resonant Enhancement of Photocatalytic Water Splitting Under Visible Illumination. *Nano Lett.* **11**, 1111–1116 (2011).
- [113] Linic, S., Christopher, P. & Ingram, D. B. Plasmonic-metal nanostructures for efficient conversion of solar to chemical energy. *Nat. Mater.* **10**, 911–921 (2011).

- [114] Wu, Z.-C., Zhang, Y., Tao, T.-X., Zhang, L. & Fong, H. Silver nanoparticles on amidoxime fibers for photo-catalytic degradation of organic dyes in waste water. *Appl. Surf. Sci.* **257**, 1092–1097 (2010).
- [115] Christopher, P., Xin, H. & Linic, S. Visible-light-enhanced catalytic oxidation reactions on plasmonic silver nanostructures. *Nat. Chem.* 1–6 (2011).
- [116] Wu, X., Thrall, E. S., Liu, H., Steigerwald, M. & Brus, L. Plasmon Induced Photovoltage and Charge Separation in Citrate-Stabilized Gold Nanoparticles. *J. Phys. Chem. C* **114**, 12896–12899 (2010).
- [117] Nitzan, A. & Brus, L. E. Can Photochemistry Be Enhanced on Rough Surfaces. *J. Chem. Phys.* **74**, 5321–5322 (1981).
- [118] Chen, C. J. & Osgood, R. M. Direct observation of the local-field-enhanced surface photochemical reactions. *Phys. Rev. Lett.* **50**, 1705–1708 (1983).
- [119] Adleman, J. R., Boyd, D. A., Goodwin, D. G. & Psaltis, D. Heterogenous Catalysis Mediated by Plasmon Heating. *Nano Lett.* **9**, 4417–4423 (2009).
- [120] Yen, C.-W. & El-Sayed, M. A. Plasmonic Field Effect on the Hexacyanoferrate (III)-Thiosulfate Electron Transfer Catalytic Reaction on Gold Nanoparticles: Electromagnetic or Thermal? *J. Phys. Chem. C* **113**, 19585–19590 (2009).
- [121] Kimata, M. Metal Silicide Schottky Infrared Detector Arrays. In Capper, P. & Elliott, C. T. (eds.) *Infrared Detectors and Emitters: Materials and Devices* (Kluwer Academic Publishers, Boston, 2001).
- [122] Dereniak, E. L. & Boreman, G. D. *Infrared Detectors and Systems* (John Wiley & Sons, Inc., New York, 1996).
- [123] Vickers, V. E. Model of Schottky barrier hot-electron-mode photodetection. *Appl. Opt.* **10**, 2190–2192 (1971).
- [124] Shepherd Jr, F. D. & Yang, A. C. Silicon Schottky retinas for infrared imaging. In *Electron Devices Meeting, 1973 International*, 310–313 (IEEE, 1973).
- [125] Ridley, B. K. *Quantum Processes in Semiconductors* (Clarendon Press, Oxford, 1999), 4 edn.

- [126] Hecht, E. *Optics* (Pearson, 2002), 4 edn.
- [127] Hao, J., Zhou, L. & Qiu, M. Nearly total absorption of light and heat generation by plasmonic metamaterials. *Phys. Rev. B* **83** (2011).
- [128] Ladst  dter, F., Hohenester, U., Puschnig, P. & Ambrosch-Draxl, C. First-principles calculation of hot-electron scattering in metals. *Phys. Rev. B* **70**, 235125 (2004).
- [129] Eastman, D. E. Photoemission Spectroscopy of Metals. In Passaglia, E. (ed.) *Techniques of Metals Research* (Interscience, 1972).
- [130] Ashcroft, N. W. & Mermin, N. D. *Solid State Physics* (Harcourt Brace, Orlando, 1976).
- [131] Kanter, H. Slow-Electron Mean Free Paths in Aluminum, Silver, and Gold. *Phys. Rev. B* **1**, 522–536 (1970).
- [132] Quinn, J. J. Range of Excited Electrons in Metals. *Phys. Rev.* **1**, 1453–1457 (1962).
- [133] Schmidt, M., Brauer, M. & Hoffmann, V. Influence of scattering on internal photoemission in heterostructures. *Appl. Surf. Sci.* **102**, 303–307 (1996).
- [134] Williams, R. *Injection Phenomena*, vol. 6 of *Semiconductors and Semimetals* (Academic Press, New York, 1970).
- [135] Dalal, V. L. Simple Model for Internal Photoemission. *J. Appl. Phys.* **42**, 2274 (1971).
- [136] Kane, E. O. Simple Model for Collision Effects in Photoemission. *Phys. Rev.* **147**, 335 (1966).
- [137] Kadlec, J. Theory of internal photoemission in sandwich structures. *Phys. Rep.* **26**, 69–98 (1976).
- [138] Fowler, R. H. The analysis of photoelectric sensitivity curves for clean metals at various temperatures. *Phys. Rev.* **38**, 45 (1931).
- [139] Kovacs, D., Winter, J., Meyer, S., Wucher, A. & Diesing, D. Photo and particle induced transport of excited carriers in thin film tunnel junctions. *Phys. Rev. B* **76** (2007).

- [140] Kane, E. Theory of Photoelectric Emission from Semiconductors. *Phys. Rev.* **127**, 131–141 (1962).
- [141] Afanas'ev, V. V. *Internal Photoemission Spectroscopy: Principles and Applications* (Elsevier, Amsterdam, 2008).
- [142] Hovel, H. *Solar Cells*, vol. 2 of *Semiconductors and Semimetals* (Academic Press, 1975).
- [143] Aydin, K., Ferry, V. E., Briggs, R. M. & Atwater, H. A. Broadband polarization-independent resonant light absorption using ultrathin plasmonic super absorbers. *Nat. Comm.* **2**, 517–7 (2011).
- [144] Fang, Z. et al. Graphene-Antenna Sandwich Photodetector. *Nano Lett.* **12**, 3808–3813 (2012).
- [145] Bates, C. W. & Hendricks, A. Quantum efficiencies of PtSi pSi composites in the 3-5 micron wavelength range. *Appl. Phys. Lett.* **87**, 233510 (2005).
- [146] Fathauer, R. W., Iannelli, J. M., Nieh, C. W. & Hashimoto, S. Infrared response from metallic particles embedded in a single-crystal Si matrix: The layered internal photoemission sensor. *Appl. Phys. Lett.* **57**, 1419 (1990).
- [147] Warren, A. C. et al. 1.3- mu m P-i-N photodetector using GaAs with As precipitates (GaAs:As). *IEEE Electron Device Letters* **12**, 527–529 (1991).
- [148] Schmidt, M., Brauer, M., Bannach, J. & Flietner, H. Characterization of Heterojunctions by Photoinjection. *Proceedings of the 12th European Photovoltaic Solar Energy Conference* 1–5 (1994).
- [149] Schmidt-Ott, A., Schurtenberger, P. & Siegmann, H. C. Enormous Yield of Photoelectrons From Small Particles. *Phys. Rev. Lett.* **45**, 1284–1287 (1980).
- [150] Faraci, G., Pennisi, A. R. & Margaritondo, G. Mechanism of Photoelectron Yield Enhancement From Ag Clusters. *Phys. Rev. B* **40**, 4209–4211 (1989).
- [151] Chen, Q. Y. & Bates, C. W. Geometrical Factors in Enhanced Photoyield From Small Metal Particles. *Phys. Rev. Lett.* **57**, 2737–2740 (1986).

- [152] Muller, U., Burtscher, H. & Schmidt-Ott, A. Photoemission From Small Metal Spheres - a Model Calculation Using an Enhanced 3-Step Model. *Phys. Rev. B* **38**, 7814–7816 (1988).
- [153] Endriz, J. & Spicer, W. Surface-Plasmon-One-Electron Decay and its Observation in Photoemission. *Phys. Rev. Lett.* **24**, 64–68 (1970).
- [154] Pines, D. Collective Energy Losses in Solids. *Rev. Mod. Phys.* **28**, 184–198 (1956).
- [155] Kreibig, U. & Vollmer, M. *Optical Properties of Metal Clusters* (Springer-Verlag, Berlin, 1995).
- [156] Guo, Z., Habenicht, B. F., Liang, W.-Z. & Prezhdo, O. V. Ab initio study of phonon-induced dephasing of plasmon excitations in silver quantum dots. *Phys. Rev. B* **81**, 125415 (2010).
- [157] Perner, M. et al. Optically induced damping of the surface plasmon resonance in gold colloids. *Phys. Rev. Lett.* **78**, 2192–2195 (1997).
- [158] Bigot, J., Halte, V., Merle, J. & Daunois, A. Electron dynamics in metallic nanoparticles. *Chem. Phys.* **251**, 181–203 (2000).
- [159] Luk'yanchuk, B. et al. The Fano resonance in plasmonic nanostructures and metamaterials. *Nat. Mater.* **9**, 707–715 (2010).
- [160] Hofmann, J. & Steinmann, W. Plasma Resonance in the Photoemission of Silver. *Phys. Stat. Sol. B* **30**, K53–K56 (1968).
- [161] Endriz, J. & Spicer, W. Study of Aluminum Films. II. Photoemission Studies of Surface-Plasmon Oscillations on Controlled-Roughness Films. *Phys. Rev. B* **4**, 4159–4184 (1971).
- [162] Feuerbacher, B. & Fitton, B. Investigation of Collective Electron Oscillations in Cd, Mg, and Zn by Photoemission. *Phys. Rev. Lett.* **24**, 499–502 (1970).
- [163] Sass, J. K., Sen, R. K., Meyer, E. & Gerischer, H. Effect of surface plasmon excitation on photoemission and photooxidation processes at a silver-electrolyte interface. *Surf. Sci.* **44**, 515–528 (1974).

- [164] Furtak, T. E. & Sass, J. K. Crystallographic anisotropy in the decay of surface plasmons to photoelectrons. *Surf. Sci.* **78**, 591–597 (1978).
- [165] Jacob, Z. & Shalaev, V. M. Plasmonics Goes Quantum. *Science* **334**, 463–464 (2011).
- [166] Feuerbacher, B., Fitton, B. & Willis, R. F. (eds.) *Photoemission and the Electronic Properties of Surfaces* (John Wiley & Sons, 1978).
- [167] Levinson, H., Plummer, E. & Feibelman, P. Effects on Photoemission of the Spatially Varying Photon Field at a Metal Surface. *Phys. Rev. Lett.* **43**, 952–955 (1979).
- [168] Herink, G., Solli, D. R., Gulde, M. & Ropers, C. Field-driven photoemission from nanostructures quenches the quiver motion. *Nature* **483**, 190–193 (2012).
- [169] Kupersztych, J., Monchicourt, P. & Raynaud, M. Ponderomotive Acceleration of Photoelectrons in Surface-Plasmon-Assisted Multiphoton Photoelectric Emission. *Phys. Rev. Lett.* **86**, 5180–5183 (2001).
- [170] Raynaud, M. & Kupersztych, J. Ponderomotive effects in the femtosecond plasmon-assisted photoelectric effect in bulk metals: Evidence for coupling between surface and interface plasmons. *Phys. Rev. B* **76**, 241402 (2007).
- [171] Sheldon, M. T. & Atwater, H. A. The plasmoelectric effect: optically induced electrochemical potentials in resonant metallic structures. Preprint. (2012). URL <http://arxiv.org/abs/1202.0301>.
- [172] Durach, M., Rusina, A. & Stockman, M. I. Giant surface-plasmon-induced drag effect in metal nanowires. *Phys. Rev. Lett.* **103**, 186801 (2009).
- [173] Noginova, N., Yakim, A. V., Soimo, J., Gu, L. & Noginov, M. A. Light-to-current and current-to-light coupling in plasmonic systems. *Phys. Rev. B* **84**, 035447 (2011).
- [174] Moskovits, M., Tay, L., Yang, J. & Haslett, T. SERS and the single molecule. *Topics Appl. Phys.* **82**, 215–226 (2002).
- [175] Dahlke, W. E. & Greve, D. W. Statistics of trap photoemission in MIS tunnel diodes. *Solid State Electron.* **22**, 893–903 (1979).

- [176] Sharma, U. & Dahlke, W. E. Infrared photoionization of interface states in Cr-SiO₂-(n,p)Si structures. *J. Appl. Phys.* **57**, 1186–1189 (1985).
- [177] Greve, D. W. & Dahlke, W. E. Photoionization cross section and density of interface states in MOS structures. *Appl. Phys. Lett.* **36**, 1002–1004 (1980).
- [178] Pierret, R. F. & Roesner, B. B. Photo-thermal probing of Si-SiO₂ surface centers—II. *Solid State Electron.* **19**, 593–603 (1976).
- [179] Chen, X., Liu, L., Yu, P. Y. & Mao, S. S. Increasing Solar Absorption for Photocatalysis with Black Hydrogenated Titanium Dioxide Nanocrystals. *Science* **331**, 746–750 (2011).
- [180] Ardo, S. & Meyer, G. J. Photodriven heterogeneous charge transfer with transition-metal compounds anchored to TiO₂ semiconductor surfaces. *Chem. Soc. Rev.* **38**, 115 (2008).
- [181] Cardona, M. & Harbeke, G. Optical properties and band structure of wurtzite-type crystals and rutile. *Phys. Rev.* **137**, A1467–A1476 (1965).
- [182] De Jongh, P. E. & Vanmaekelbergh, D. Trap-Limited Electronic Transport in Assemblies of Nanometer-Size TiO₂ Particles. *Phys. Rev. Lett.* **77**, 3427–3430 (1996).
- [183] Westermark, K. et al. Determination of the electronic density of states at a nanosstructured TiO₂/Ru-dye/electrolyte interface by means of photoelectron spectroscopy. *Chem. Phys.* **285**, 157–165 (2002).
- [184] Mubeen, S., Hernandez-Sosa, G., Moses, D., Lee, J. & Moskovits, M. Plasmonic Photosensitization of a Wide Band Gap Semiconductor: Converting Plasmons to Charge Carriers. *Nano Lett.* **11**, 5548–5552 (2011).
- [185] Kazuma, E., Sakai, N. & Tatsuma, T. Nanoimaging of localized plasmon-induced charge separation. *Chem. Comm.* **47**, 5777 (2011).
- [186] Tian, Y. & Tatsuma, T. Plasmon-induced photoelectrochemistry at metal nanoparticles supported on nanoporous TiO₂. *Chem. Comm.* 1810–1811 (2004).
- [187] Reineck, P. et al. A Solid-State Plasmonic Solar Cell via Metal Nanoparticle Self-Assembly. *Adv. Mater.* **24**, 4750–4755 (2012).

- [188] Govorov, A. O. & Richardson, H. H. Generating heat with metal nanoparticles. *Nano Today* **2**, 30–38 (2007).
- [189] Johnson, P. B. & Christy, R. W. Optical Constants of the Noble Metals. *Phys. Rev. B* **6**, 4370–4379 (1972).
- [190] Palik, E. D. (ed.) *Handbook of Optical Constants of Solids* (Academic Press, San Diego, 1985).
- [191] Schmidt, T., Martel, R., Sandstrom, R. L. & Avouris, P. Current-induced local oxidation of metal films: Mechanism and quantum-size effects. *Appl. Phys. Lett.* **73**, 2173–2175 (1998).
- [192] Ferry, V. E. *Light Trapping in Plasmonic Solar Cells*. Ph.D. thesis, California Institute of Technology (2011).
- [193] Henry, D. *ICP Etching of Silicon for Micro and Nanoscale Devices*. Ph.D. thesis, California Institute of Technology, Pasadena, CA (2010).